Reduction Methods for Feedback Stabilization of Fluid Flows

Sunil Ahuja

A Dissertation
Presented to the Faculty
of Princeton University
in Candidacy for the Degree
of Doctor of Philosophy

Recommended for Acceptance
By the Department of
Mechanical and Aerospace Engineering

Advisor: Clarence W. Rowley

September 2009

© Copyright by Sunil Ahuja, 2009. All rights reserved.

Abstract

This dissertation deals with reduction of two classes of dynamical systems in order to make them suitable for control design using linear systems theory. The first class consists of the large-dimensional systems governing fluid flows, for which we employ dimension reduction techniques for stabilization of unstable steady states. The second class consists of systems with a continuous symmetry, for which we use a template-based symmetry reduction method for stabilization of unstable relative equilibria.

Model reduction has opened the world of linear control techniques to flow control. Linear control methods involve large matrix computations and are limited to dimensions of $O(10^{2-4})$, while discretized fluid equations are typically of $O(10^{5-8})$, making model reduction essential. A method that has been shown to accurately capture dynamics is the snapshot-based approximate balanced truncation, in which the governing equations (linearized about a steady state) are projected onto a small number (typically ≤ 100) of dynamically important modes. The reduced models obtained using this method accurately capture the input-output (actuation to sensing) behavior. However, a limitation is that this method is restricted to systems linearized about stable steady states. In this work, we extend its applicability to unstable steady states, assuming a small number of unstable modes. The unstable dynamics is treated exactly while the (large dimensional) stable dynamics is modeled. We show a theoretical equivalence between approximate balanced truncation and an experimental system identification technique called eigensystem realization algorithm (ERA). We extend ERA to simulations and obtain an order-of-magnitude cost reduction over balanced truncation.

With the motivation of designing micro-air vehicles inspired by bird flight, the reduction techniques are applied to a model problem of the 2D flow past a flat plate at a low Reynolds number and a large angle of attack. The natural (uncontrolled) flow is periodic vortex shedding, though there also exists an unstable steady state that we seek to stabilize. The control actuation is modeled using a localized body-force actuator close to either the leading or the trailing edge of the plate and velocities are measured at two near-wake sensor locations. We obtain reduced models of the input-output dynamics linearized about the unstable steady state and provide time and frequency domain comparisons to show that 20-30 order models accurately capture the full system dynamics. We develop sensor-based feedback controllers and include them in the full nonlinear simulations. Even though the models are valid in a local neighborhood of the steady state, we show that they are even capable of suppressing the periodic vortex shedding, which is a nonlinear phenomenon.

We also consider systems with a continuous symmetry and use a template-based approach to reduce the equations to a frame in which the symmetry is factored out. Relative equilibria are steady states in the symmetry-reduced frame; an example is traveling waves in systems with periodic boundary conditions. The control goal is to stabilize unstable relative equilibria and the control design is based on linearization of the reduced equations about these steady states. A systematic reconstruction procedure to obtain the form of the controller in the original coordinates is provided. The key feature of the design is that the controlled system retains the symmetry of the original system. The control is demonstrated using various examples, including stabilization of unstable traveling waves in the 1D Kuramoto-Sivashinsky equation.

Contents

Abstract iii
Contents v
List of Figures vii
List of Tables ix

1 Introduction 2
1.1 Dimension reduction for flow control 2
1.1.1 Control of flow past 2-D wings 5
1.2 Control of systems with symmetry 6
1.3 Outline and contributions 9

2 Model dimension reduction of linear state-space systems 11
2.1 Model reduction: overview 12
2.1.1 Projection onto the global eigenspace 13
2.1.2 Proper orthogonal decomposition 14
2.1.3 Exact balanced truncation: stable systems 16
2.1.4 Approximate balanced truncation: stable systems 17
2.2 Balanced truncation: unstable systems 20
2.2.1 Exact method 20
2.2.2 Approximate method 21
2.2.3 Algorithm 24
2.3 Eigensystem Realization Algorithm (ERA) 25
2.3.1 Equivalence with approximate balanced truncation 27

3 Control of flow past a flat plate 30
3.1 Immersed boundary projection method 30
3.1.1 Linearized and adjoint equations 33
3.2 Model problem: flow past a flat plate 35
3.2.1 Numerical parameters 35
3.2.2 Input and output 36
3.3 Steady state analysis 38
3.3.1 Continuation using Newton-GMRES 38
3.3.2 Linear stability analysis 41
3.4 Reduced-order models 44

3.4.1 Comparison with ERA . . . 48
3.5 Full-state feedback control . . . 50
3.6 Observer-based control . . . 53
3.6.1 Observer design 1: using models that are not balanced . . . 54
3.6.2 Observer design 2: develop balanced models . . . 56
3.6.3 Modeling of process and sensor noise . . . 57
3.6.4 Observer-based control . . . 58
3.7 Summary . . . 59

4 Symmetry reduction for stabilization of relative equilibria 63
4.1 Template-based reduction . . . 64
4.1.1 Template dynamics of systems with control . . . 64
4.1.2 Control objective . . . 67
4.2 Control of differential-algebraic equations . . . 67
4.2.1 Linearization about a relative equilibrium . . . 68
4.3 State-space formulation . . . 70
4.3.1 Controllability and stabilizability . . . 71
4.4 Feedback control design . . . 71
4.4.1 Optimal control with equivariant actuation . . . 72
4.4.2 Amplitude and phase actuation . . . 74
4.5 Examples . . . 76
4.5.1 A planar ODE system with rotational symmetry . . . 76
4.5.2 Inverted pendulum on a cart . . . 80
4.5.3 The Kuramoto-Sivashinsky equation: a spatially distributed example . . . 82
4.6 Summary . . . 93

5 Conclusions and future work 96
5.1 Conclusions . . . 96
5.2 Future work . . . 98

A Balancing transformation for unstable systems 101

B Derivation of the adjoint equations 103
B.1 Adjoint formulation of the immersed boundary method . . . 103
B.2 Adjoint of differential algebraic equations . . . 104

C Linearization of slice dynamics 106

Bibliography 108

List of Figures

2.1 Model reduction idea 12
2.2 Balancing transformation 16

3.1 Multi-domain solution of the Poisson equation 34
3.2 Model of the actuators for flow past a flat plate 36
3.3 Clustering of eigenvalues of the discrete time-stepper 40
3.4 Convergence of Newton-GMRES 40
3.5 Variation of the lift and drag coefficients with angle of attack α . . 42
3.6 Unstable steady state at $\alpha = 35°$ 43
3.7 Growth rates and the frequencies of the dominant eigenmode 43
3.8 Right and left unstable eigenvectors of the linearized dynamics at $\alpha = 35°$ 44
3.9 POD modes of the impulse response restricted to the stable subspace 45
3.10 Balancing and adjoint modes of the stable subspace 46
3.11 Reduced-order models using approximate balanced truncation: empirical Hankel singular values and diagonal elements of the controllability and observability Gramians 47
3.12 Reduced-order models using ERA: empirical Hankel singular values and diagonal elements of the controllability and observability Gramians 48
3.13 Comparison of the outputs of reduced-order models with impulse response of the full simulation 49
3.14 Schematic of full-state feedback control implementation 51
3.15 Full-state feedback control: comparison of model outputs with linear simulation 52
3.16 Full-state feedback control: evolution of the lift-coefficient for different initial conditions in the nonlinear simulation 53
3.17 Full-state feedback control: comparison of model outputs with full nonlinear simulation 54
3.18 Energy evolution of the impulse response, compared with projection onto POD modes 55
3.19 Velocity reconstruction, at sensor locations, using POD modes . . . 56
3.20 Schematic of observer-based control implementation 58
3.21 Observer-based control using leading edge actuation: evolution of the lift-coefficient for different initial conditions 60

3.22 Reconstruction of the model states using reduced-order observer . . 61
3.23 Observer-based control using trailing edge actuation: evolution of the lift-coefficient for different initial conditions 61
3.24 Reconstruction of the outputs using reduced-order observer obtained using ERA 62

4.1 Method of slices 66
4.2 Feedback control using the method of slices 74
4.3 Planar rotationally invariant system. 78
4.4 Stabilization of inverted pendulum on a cart 83
4.5 Relative equilibria of the Kuramoto-Sivashinsky (K-S) equation . . 84
4.6 Stabilization of unstable traveling waves using equivariant actuation 88
4.7 Fig. 4.6 (continued) 89
4.8 Stabilization of unstable traveling waves using phase-amplitude actuation 90
4.9 Stabilization of unstable traveling waves using Gaussian actuation . 92
4.10 Stabilization of steady states using equivariant actuation 93
4.11 Fig. 4.10 (continued) 94
4.12 Equivariance of the closed-loop system 95

List of Tables

3.1 Comparison of the computational costs of approximate balanced truncation and ERA. 50

4.1 LQR gains for control of inverted pendulum on a cart. 82

Chapter 1

Introduction

The theme that runs throughout this dissertation is that of employing *reduction* with the goal of *stabilization* of certain features using feedback control. In particular, we consider two types of systems. The first one involves fluid flows that often exhibit simple low-dimensional behavior, even though the governing equations are the infinite-dimensional Navier-Stokes equations. For such systems, we employ dimension reduction techniques to obtain reduced models. The second class of systems consists of those endowed with a continuous symmetry, for which we employ symmetry reduction techniques to stabilize relative equilibria.

1.1 Dimension reduction for flow control

Many fluid flows in nature appear low-dimensional to the eye, and often are characterized by coherent structures. However, they are mathematically described by the Navier-Stokes equations, which in numerical computations lead to extremely large sets of equations, typically $O(10^{5-8})$ and sometimes even higher. Flow control is important for many applications, such as drag reduction in aircraft, enhanced mixing for efficient combustion or air-conditioning, quieter vehicles, and many others. The tools for control design from systems theory are however limited to systems of much lower dimension, up to $O(10^{3-4})$. The main reason for this limitation is that many of these control theoretic techniques require solutions of matrix equalities or inequalities, where the matrices involved are full and of the same dimension as the state. For instance, for a scalar variable discretization with $n = 10^5$ grid points, the storage of an n^2-matrix itself requires 74 Gigabytes, and the cost scales as n^3 for computations such as matrix inversion or solution of Lyapunov or Riccati equations or inequalities. Dimension reduction techniques seek to exploit the simplicity of fluid flows in order to obtain reduced yet accurate models for which the control tools are applicable.

Proper orthogonal decomposition. Extensive research effort in model reduction has focused on the method of proper orthogonal decomposition (POD) and Galerkin projection, introduced to fluid mechanical systems by Lorenz (1956) in the context of statistical weather prediction and later by Lumley (1970) in the context of identifying coherent structures in turbulent flows. The method captures the energetically dominant features of fluid flows (Holmes *et al.*, 1996) and has been widely used to achieve better understanding of complex flow physics. In one of the earliest applications, Corke *et al.* (1994) used a POD-based model to guide control experiments on an axisymmetric jet. Lumley & Blossey (1998) used the method for active control of turbulent boundary layers in order to reduce the drag by building on their prior experience with design of controllers for reduced models (Coller, 1995). Ravindran (2000) developed optimal control strategies for reducing the recirculation bubble length in the flow behind a backward facing step; two different actuation mechanisms, using moving walls and mass blowing through the boundary were considered. Other applications of POD-based methods for flow control include bluff-body wake suppression (Graham *et al.*, 1999*a*; Noack *et al.*, 2004; Tadmor *et al.*, 2007; Siegel *et al.*, 2008) and noise reduction in cavity flow (Rowley & Juttijudata, 2005; Gloerfelt, 2008).

The main limitation of POD is that, although the resulting modes are energetically optimal, the reduced models obtained by subsequent Galerkin projection of the governing equations do not always represent the dynamics accurately. Furthermore, POD does not account for the control actuation and sensing, which can be important for good performance; for example, Prabhu *et al.* (2001) explored the effect of wall-based control on turbulent channel flow and showed that a POD basis obtained from the uncontrolled case grossly under-predicts the Reynolds stress of the controlled flow. Various modifications to improve upon POD-based models have been proposed; refer to the introduction of Siegel *et al.* (2008) for a review of these techniques. Graham *et al.* (1999*a*,*b*) devised strategies to incorporate control action in the reduced models and developed optimal controllers for flow past a cylinder actuated by the cylinder rotation. Noack *et al.* (2003) included a shift mode, representing a mean-field correction, and global eigenmodes to the POD basis and obtained significant improvement of the transient dynamics in flow past a cylinder, while Luchtenburg *et al.* (2009) used shift modes to develop mean-field POD models of a periodically actuated flow past an airfoil that captured the transients between actuated and unactuated regimes. Siegel *et al.* (2008) developed a double POD method to account for the changes in the spatial structure of the POD modes during transients, and used an artificial neural network based approach to obtain reduced models.

Balanced truncation. A model reduction technique that has attracted considerable interest recently is the approximate balanced truncation method developed by Rowley (2005), also called balanced POD. As the name suggests, the method is an approximation to the balanced truncation method of Moore (1981), which is a control theoretic method to obtain reduced models of linear, stable, time-invariant, state-space systems. Balanced truncation accounts for the effects of both actuation and sensing, and results in models that capture the input-output dynamics of the full system within a-priori error bounds. However, like many control theoretic tools, this technique becomes intractable for large-dimensional systems. The approximate method of Rowley (2005) overcomes this drawback by adopting ideas from POD to develop a computationally tractable algorithm. The method has been used to obtain models of linearized channel flow by Ilak & Rowley (2008) and to control boundary layers for drag reduction by Bagheri *et al.* (2009*a*), and has been shown to accurately capture control actuation and also to outperform the POD/Galerkin models.

In contrast to the POD/Galerkin approach, which results in models of full nonlinear equations, the approximate balanced truncation method results in models only of linearized equations. Although it appears to be a disadvantage, it was argued in the review by Kim & Bewley (2007), that for developing control strategies, it is often sufficient to use linearized models that accurately capture the effects of inputs and outputs of the system.

The balanced truncation method of Moore (1981) is applicable only to systems linearized about *stable* steady states. An extension to *unstable* linear systems was proposed by Zhou *et al.* (1999), by introducing frequency-domain definitions of controllability and observability Gramians. Reduced-order models were obtained by first decoupling the dynamics on the stable and unstable subspaces, and then truncating the relatively uncontrollable and unobservable modes on each of the two subspaces. In this work, we build upon the techniques of Rowley (2005) and Zhou *et al.* (1999) to develop a systematic algorithm for modeling unstable systems. The dynamics on the unstable subspace is treated *exactly* by a projection onto the global eigenmodes, while the dynamics on the stable subspace is modeled using the algorithm developed by Rowley (2005).

Eigensystem realization algorithm. The approximate balanced truncation algorithm involves post-processing data from linear and adjoint impulse-response simulations to compute reduced models. The adjoint simulations are not physical, which limits the method to computations only. In this work, we establish equivalence between this method and eigensystem realization algorithm (ERA), a system identification technique developed by Juang & Pappa (1985). The equivalence allows two significant advances over the original method. First, ERA does not require adjoint simulations and thus can be used in experiments. Second, when adapted to simulations, ERA results in an order-of-magnitude reduction in computational cost over approximate balanced truncation. ERA has been used previously for model reduction of fluids: Gaitonde & Jones (2003) developed models of airfoils with small amplitude heaving and pitching as inputs; Silva & Bartels (2004) developed models of unsteady aerodynamics and combined it with a structural model for aeroelastic analysis and flutter prediction in 3D wings; Cattafesta *et al.* (1997) used the method to obtain models for lift enhancement in flow over airfoils, while Cabell *et al.* (2006) developed controllers to reduce tones generated by flow over a cavity.

1.1.1 Control of flow past 2-D wings

As a proof-of-concept study, the modeling procedure developed in this work is applied to the problem of two dimensional low-Reynolds-number flow past a flat plate at a large angle of attack. We develop reduced-order models and design controllers that stabilize the unstable steady states of this flow. The motivation for the choice of this problem comes from our interest in regulating vortices in separated flows behind low aspect-ratio wings, which is of importance in design of micro air vehicles (MAVs). Recently, design of MAVs has been inspired from experimental observations in insect and bird flights of a stabilizing leading edge vortex (Birch & Dickinson, 2001; Ellington *et al.*, 1996), which remains attached throughout the wing stroke and provides enhanced lift. So, it could be beneficial to design controllers that can manipulate the wake of MAVs to enhance lift and achieve better maneuverability in presence of wind gusts. Recent studies in this direction, using open-loop control of the flow past low-aspect-ratio wings using steady or periodic blowing, were performed computationally by Taira & Colonius (2009*a*) and experimentally by Williams *et al.* (2008). These studies explored different forcing amplitudes and frequencies, locations and directions. However, the design of feedback controllers remains a challenge, due to the large dimensionality of the problem and the complex flow physics. We present computational tools that we hope can at least pave a direction and provide techniques towards addressing some of these challenges.

Much of the previous research in this area has focused on the control of flow past a cylinder, which is qualitatively similar to the flow past a flat plate at large angle of attack, with the natural flow in both the cases being periodic vortex shedding. The flow past a cylinder undergoes a transition from steady state to periodic shedding with increasing Reynolds number, while a similar transition occurs in the flow past a flat plate with increasing angle of attack. There has been considerable research effort on suppression of this shedding in cylinder and other bluff body wakes, using passive and active, open-loop and feedback control, as reviewed by Choi *et al.* (2008). Among those, some techniques are based on reduced-order models; for instance, Gillies (1998) developed models using artificial neural networks and a POD basis, Graham *et al.* (1999*a*) modified the POD/Galerkin method to account for actuation by means of cylinder-rotation, while Siegel *et al.* (2008) developed a double POD method to account for changes in the wake structure during transients. Some earlier efforts in the control of a *flat-plate* wake include those by Cortelezzi (1996), Cortelezzi *et al.* (1997) who used vortex-based methods to model the flow past a vertical plate (angle of attack = 90°); vortex-based models form their own class of modeling techniques reviewed recently by Protas (2008). Lagrangian coherent structures were used by Wang *et al.* (2003) to enhance mixing in flow past a bluff body with the trailing surface similar to the vertical flat plate. One of the few efforts towards control of flat plate at an angle of incidence was by Zannetti & Iollo (2003), who used a passive leading-edge suction control along with a potential flow vortex model. Pastoor *et al.* (2008) also used reduced-order vortex models for drag reduction on an elongated D-shaped bluff body.

In this work, we consider the two-dimensional flow past a flat plate, actuated by a localized body force close to either the leading or the trailing edge, with two near-wake velocity sensors. We design reduced-order models of the flow linearized about an unstable steady state at a large angle of attack, using approximate balanced truncation and ERA. We use these models to develop a reduced-order compensator and, even though the models are linear, we show that the resulting controller is able to suppress vortex shedding, which is a consequence of nonlinearity.

1.2 Control of systems with symmetry

The second class of systems that we consider are those with a continuous symmetry: some of the examples in fluid mechanical systems are plane channel flow, Rayleigh-Bénard convection and Taylor-Couette flow, all of which have translational or rotational symmetry. Relative equilibria constitute particular types of solutions in such systems: they are steady states in a frame of reference with the symmetry factored out; some examples in fluid systems are traveling waves in the channel flow, spiral rolls in Rayleigh-Bénard convection (Bodenschatz *et al.*, 2000) and Taylor vortices in Taylor-Couette flow. Examples in other systems include rotating spiral waves in models of pattern formation (Golubitsky & Stewart, 2002), vehicles or animals moving in specific formations (Justh & Krishnaprasad, 2004), coordinated networks of rotating rigid bodies such as satellites (Nair & Leonard, 2007), and many others.

The dynamics of systems with symmetry can be thought of as a sum of two components: one associated with the symmetry variable called the *group dynamics* (e.g., the position of a traveling wave), and the second associated with the rest of the variables called the *shape dynamics* (e.g., the shape of a traveling wave). A relative equilibrium is then a fixed point of the shape dynamics. Our goal is to develop techniques for stabilization of unstable relative equilibria, and the approach we adopt is that of symmetry reduction to obtain appropriate shape dynamics. We then linear the shape dynamics about a relative equilibrium (steady state) and use linear systems tools to develop optimal feedback controllers.

In the context of mechanical systems that arise from a Lagrangian or a Hamiltonian, stabilization of relative equilibria has been an active topic of research; for example, see Bloch *et al.* (2000, 2001), Jalnapurkar & Marsden (1999, 2000) and Bullo (2000). The control technique common to these works is the use of either kinetic or potential shaping to modify the Lagrangian in order to achieve the desired stability properties. In the work of Bloch *et al.* (2000, 2001), a control term was added to the Lagrangian (leaving the relative equilibrium to be stabilized unchanged) to form a controlled Lagrangian and the additional terms appearing in the corresponding Euler-Lagrange equations were identified as the control forces. In Bloch *et al.* (2000), relative equilibria were stabilized by kinetic shaping, which essentially means modifying the kinetic energy by control terms. Potential shaping was further included in Bloch *et al.* (2001), to achieve stability in the full phase space by breaking the symmetry. Jalnapurkar & Marsden (2000) used potential shaping to stabilize relative equilibria for which the shape configuration is unstable. This work was extended by Jalnapurkar & Marsden (1999) to stabilize relative equilibria in the full phase space. Bullo (2000) considered systems on Riemannian manifolds and achieved exponential stabilization in the full phase space. The work used potential shaping to stabilize the subspace orthogonal to the symmetry direction and exponential stability was achieved by adding dissipation. Such mechanical systems (arising from a Lagrangian or a Hamiltonian) often have the advantage of a readily available Lyapunov function, which not only leads to stability results, but also naturally allows one to define the domains of attraction. Even though the stability achieved by this method is just Lyapunov stability, adding dissipation can often lead to asymptotic stability.

Much previous work towards control of more general (not necessarily mechanical) systems with symmetry has focused on linear systems. Brockett & Willems (1974) considered a system of ordinary differential equations (ODEs), arising upon discretization of certain partial differential equations (PDEs), in which the state and control matrices had a *block circulant* structure. Their work exploited the symmetry to save computational effort in solving system theoretic problems. Linear optimal control problems with symmetry were studied by Lewis & Martin (1983) and Mozhaev (1975*a*,*b*). The latter showed that such problems can be decomposed into several smaller dimensional independent problems. Bamieh *et al.* (2002) considered the optimal control problem of linear, translationally invariant PDEs, where the feedback law was chosen so as to minimize a given translationally invariant objective or cost function. They showed that the resulting feedback inherits the translational invariance and that it can be obtained by solving a one-parameter family of finite-dimensional optimal control problems. D'Andrea & Dullerud (2003) addressed the control problem of systems consisting of extremely large number of interconnected subsystems with a symmetric structure. Their work exploited this symmetry to develop computationally tractable tools for control design. Also see the references listed in the introduction of Bamieh *et al.* (2002) for more information along this line of research.

An important early work considering the control of general nonlinear systems with symmetry was by Grizzle & Marcus (1985). They showed that, under certain conditions, such systems can be locally or globally decomposed into lower dimensional subsystems. In particular, if the original system evolves on a manifold M and the symmetry group acting on M is G, they showed that such a system can be globally decomposed into two subsystems: one evolving on the quotient space M/G and the other on the group space. The work of Grizzle & Marcus (1985) was extended in Grizzle & Marcus (1984) to decompose the optimal control problem into similar lower-dimensional factors. Rowley *et al.* (2003) and Rowley & Marsden (2000) obtained a similar decomposition for uncontrolled systems, and in addition presented different systematic procedures to define the quotient space for this decomposition; see also Beyn & Thümmler (2004) for different such procedures and Aronson *et al.* (2001) for an application to self-similar problems. One of the methods described in Rowley *et al.* (2003) and Rowley & Marsden (2000) is what the authors called *the method of slices* or *the template-based method*, which is applicable to systems evolving on an inner-product space. This method gives rise to a particular set of equations, called the *slice* or *template* or *shape dynamics*, in which the symmetry is dynamically factored out. These slice dynamics are constrained to evolve on a subspace that is locally isomorphic to the quotient space, called a *slice*, and the relative equilibria are just the fixed points of these dynamics. In this work, we adopt this view of the dynamics to derive feedback laws that stabilize relative equilibria of general nonlinear systems with symmetry, evolving on an inner-product space.

We will show that the template dynamics can be viewed as a set of coupled *differential-algebraic equations (DAEs)*. The algebraic equations constrain the dynamics of the differential equations to evolve on the slice. There exist substantive tools for feedback control design for DAEs, for example, see Krishnan & McClamroch (1992); Kumar & Daoutidis (1995, 1996, 1999). The methods in these papers involve obtaining an equivalent state-space realization, that is, a purely differential system, which then allows use of traditional tools from linear or nonlinear control theory. Krishnan & McClamroch (1992) considered a linear system of DAEs and developed a computational procedure using singular value decomposition to derive an equivalent set of linear ODEs suited for application of linear control techniques. Kumar & Daoutidis (1995, 1996, 1999) considered a broad class of nonlinear DAEs, developed an algorithmic procedure for deriving the equivalent state-space realization, and used that as the basis for feedback controller synthesis.

The aim of this work is to combine the template-based symmetry reduction technique with the feedback control methodology for DAEs to develop a systematic approach to stabilizing relative equilibria. The relative equilibria are simple fixed points of the template or slice dynamics. These dynamics are constrained to evolve on a slice, which for our systems is an affine subspace. This simplifies the task, allowing us to linearize about the fixed points and use standard tools from linear control theory for feedback controller design.

1.3 Outline and contributions

We now outline the main contributions of this work and their place in the dissertation. Chapters 2 and 3 deal with model dimension reduction of linear systems with control, while chapter 4 deals with symmetry reduction for stabilizing unstable relative equilibria.

Chapter 2 first reviews the projection-based model reduction techniques using global eigenmodes, proper orthogonal decomposition and approximate balanced truncation for stable linear systems in section 2.1. A key contribution, presented in section 2.2, is the extension of approximate balanced truncation to unstable systems. In section 2.3, an equivalence between approximate balanced truncation and the eigensystem realization algorithm (ERA) is exploited for achieving substantial speed-up in computations; this work was done jointly with Zhanhua Ma. The idea of exploiting ERA for reducing computational cost belongs to ZM. My contribution was to work together with ZM in solving issues that arose while implementing those ideas in numerical computations.

Chapter 3 concerns with the application of the model reduction techniques developed in chapter 2 to a model problem of the two-dimensional flow past a flat plate at a large angle of attack. The immersed boundary method used for computations is described and its linear and adjoint formulations are developed in section 3.1. A continuation study with varying angle of attack and the linear stability analysis of the resulting steady states are presented in section 3.3. Reduced-order models of the linearized dynamics are developed and evaluated by comparison with full linear simulations in section 3.4. Stabilizing controllers are developed using full-state feedback in section 3.5 and using observers based on near-wake velocity measurements in section 3.6. The resulting compensator is shown to stabilize the unstable states, and results in a sufficiently large basin of attraction to suppress the periodic vortex shedding.

Chapter 4 extends the symmetry reduction method using templates to systems with control inputs in section 4.1. The reduced dynamics are linearized about relative equilibria, which are steady states in the reduced frame, in section 4.2. Linear systems techniques are used in section 4.4 to develop two different controllers, that minimize a cost function defined in the original (unreduced) frame. The resulting controllers are shown to preserve the symmetry of the original system. The method is illustrated with three examples in section 4.5: a planar rotationally-invariant ODE, an inverted pendulum on a cart, and a translationally invariant PDE, namely, the the Kuramoto-Sivashinsky equation.

Chapter 5 provides a summary of the dissertation and suggests directions for future work.

The approximate balanced truncation for unstable systems and its application to control of the flow over a flat plate were developed in Ahuja & Rowley (2009). The computational speed-up of the approximate balancing algorithm using ERA appears in Ma *et al.* (2009). The work on template-based symmetry reduction for stabilizing unstable equilibria has been published in Ahuja *et al.* (2007).

Chapter 2

Model dimension reduction of linear state-space systems

Numerical discretization of fluid mechanical systems leads to large systems of ODEs or DAEs of dimension typically greater than $O(10^5)$. The control design of such large dimensional systems is difficult as the typical linear and nonlinear system theoretic tools are restricted to dimensions $O(10^{3-4})$. The restriction arises due to the fact that most of these tools involve solutions of certain matrix equations or inequalities (such as Lyapunov or Riccati), which becomes prohibitive due to the huge storage requirements of the matrices involved. Dimension reduction techniques have thus played an important role in making these control tools available for fluid flows.

This chapter describes some dimension reduction methods that involve projecting the governing equations onto a low-dimensional subspace. We think of the governing equations being the Navier-Stokes equations, linearized about a steady state solution, which on spatial discretization result in a large set of linear ordinary differential equations (ODEs). The chapter is organized as follows: section 2.1 gives a geometric picture of projection-based model reduction methods and reviews the existing methods based on global eigenmodes and proper orthogonal decomposition, and the approximate balanced truncation method for stable systems developed in Rowley (2005). An approximate algorithm for balanced truncation of unstable systems is developed in section 2.2; this algorithm has been developed in Ahuja & Rowley (2009). The eigensystem realization algorithm is adopted in section 2.3 for substantial computational savings of the approximate balanced truncation method; the results from this section have been presented in Ma *et al.* (2009).

2.1 Model reduction: overview

The focus here is on obtaining reduced-order models of the *input to output dynamics* of linear and time-invariant (LTI) systems of the form

$$\frac{dx}{dt} = Ax + Bu, \tag{2.1}$$

$$y = Cx, \tag{2.2}$$

where $x \in \mathcal{X}$ is the state, $u \in \mathcal{U}$ is the input, and $y \in \mathcal{Y}$ is the output of the system. We assume that $\mathcal{X} \subset \mathbb{R}^n$, $\mathcal{U} \subset \mathbb{R}^p$ and $\mathcal{Y} \subset \mathbb{R}^q$ are linear vector spaces endowed with inner-products denoted by $\langle \cdot, \cdot \rangle_{\mathcal{X}}$, $\langle \cdot, \cdot \rangle_{\mathcal{U}}$ and $\langle \cdot, \cdot \rangle_{\mathcal{Y}}$ respectively. The matrices $A \in \mathbb{R}^{n\times n}$, $B \in \mathbb{R}^{n\times p}$ and $C \in \mathbb{R}^{q\times n}$ are constant. The system (2.1) is stable if all the eigenvalues of A are strictly to the left of the imaginary axis on the complex plane. It is neutrally stable or unstable if any of these eigenvalues are on or to the right of the imaginary axis.

In general, projection-based model reduction techniques rely on the idea that the full dynamics of (2.1) is projected onto a low-dimensional subspace along a certain direction to obtain a reduced model. There are two key components for obtaining accurate models: one is the choice of a r-dimensional subspace $\mathcal{X}_r \subset \mathcal{X}$ ($r \ll n$) onto which the dynamics is restricted, and the other is the choice of direction of projection onto $\mathcal{X}_r$, often related to another r-dimensional subspace $\mathcal{Z}_r \subset \mathcal{X}$. Fig. 2.1 shows two different ways of restricting the dynamics of a general nonlinear system $\dot{x} = f(x)$ to a subspace $\mathbb{X}_r$, one being an orthogonal projection (in which case $\mathcal{Z}_r \equiv \mathcal{X}_r$), and the other being a projection along a direction orthogonal to $\mathcal{Z}_r$. Subsequent sections present different choices of these subspaces widely used to obtain reduced models.

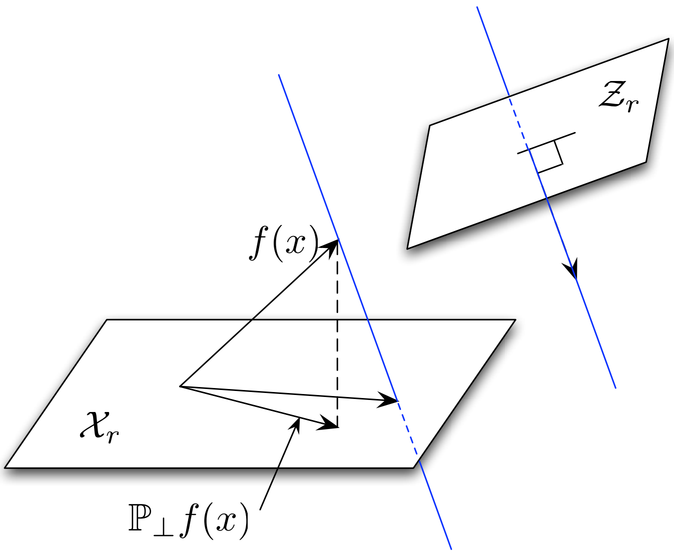

Figure 2.1: Projection of the full dynamics $f(x)$ onto $\mathcal{X}_r$.

In order to obtain an explicit form of the reduced-order models, we also need the bases spanning the subspaces $\mathcal{X}_r$ and $\mathcal{Z}_r$. In general, the choice of these bases is not arbitrary but is determined by the model reduction technique at hand, for example, by solving an optimization problem. Throughout this chapter, the bases spanning $\mathcal{X}_r$ and $\mathcal{Z}_r$ are represented by Φ, $\Psi \in \mathbb{R}^{n\times r}$, with columns denoted by ϕ_i, $\psi_i \in \mathbb{R}^n$ respectively. Then, the state x is approximated by $x_r \in \mathbb{R}^n$ using a modal expansion

$$x \approx x_r = \sum_{i=1}^{r} \phi_i a_i = \Phi a, \qquad a = (a_1, a_2, \ldots, a_r)^T, \quad a_i \in \mathbb{R}, \tag{2.3}$$

where $a \in \mathbb{R}^r$ is the reduced-order state. Substituting (2.3) in the governing equations (2.1) and taking inner-products with ψ_j yields the reduced-order model:

$$\frac{da}{dt} = \Psi^* A \Phi a + \Psi^* B u, \tag{2.4}$$

$$y = C\Phi a, \tag{2.5}$$

where the asterisk * represents the adjoint with respect to the inner-product $\langle \cdot, \cdot \rangle_{\mathcal{X}}$. Further, we have assumed that the bases Φ and Ψ are bi-orthonormal, that is,

$$\langle \psi_i, \phi_j \rangle = \delta_{ij} \quad \text{or} \quad \Psi^* \Phi = I_r. \tag{2.6}$$

where δ_{ij} is the Kronecker delta and $I_r \in \mathbb{R}^{r\times r}$ is the identity. Finally, the initial condition for (2.4) is obtained by projecting the initial condition x_0 of (2.1) as

$$a_i = \langle \psi_i, x_0 \rangle \quad \text{or} \quad a = \Psi^* x_0 \tag{2.7}$$

We now describe certain projection-based modeling techniques which we adopt later to develop a new algorithm for approximate balanced truncation of unstable systems.

2.1.1 Projection onto the global eigenspace

One of the simplest ways of obtaining the reduced-order models of (2.1) is to project the dynamics onto the leading eigenvectors of A. An appropriate restriction is obtained by choosing the direction of projection being orthogonal to the *left* eigenvectors of A. That is, the bases Φ and Ψ in (2.4) are chosen to be the leading right and left eigenvectors of A (that is, the corresponding eigenvalues have a large real part):

$$A\Phi = \Phi\Lambda \qquad \text{and} \qquad \Psi^* A = \Lambda \Psi^*, \tag{2.8}$$

where $\Lambda \in \mathbb{R}^r$ is a diagonal matrix of eigenvalues (or a block diagonal matrix representing the Jordan normal form of A). The resulting model is then given by

$$\dot{a} = \Lambda a + \Psi^* B u, \qquad y = C\Phi a \tag{2.9}$$

Even though the method is conceptually simple, the eigenvalue problem is computationally prohibitive due to the huge system of equations. The most widely used methods for such problems are based on Krylov methods, with the main advantage being that they require storage and manipulation of only a relatively small number of matrix-vector products Aw; the computational package called ARPACK developed by Lehoucq *et al.* (1998) which uses an implicitly restarted Arnoldi algorithm is often used. Further, easy implementations using computational wrappers around the original direct numerical solver were developed by Barkley & Tuckerman (1999) in an attractive timestepper-based technique. This model reduction technique has been used used by Henningson & Åkervik (2008) and Åkervik *et al.* (2007) for stability analysis and control design for the Blasius boundary layer and flow over a shallow cavity.

The global eigenmodes are useful for understanding various instability mechanisms. However, for control design, their performance is limited. The main reason being that the modes that are most important from the instability point of view might not be relevant from the controls perspective, maybe because they are difficult to excite by control actuation or are difficult to measure. Mathematically, the reduced-order models obtained using this method do not account for the particular choice of B and C in (2.1). We will see later that a method from balanced truncation precisely accounts for these two factors and thus results in both models; this has been demonstrated for a transitional channel flow by Ilak & Rowley (2008) and the Blasius boundary layer by Bagheri *et al.* (2009*a*).

2.1.2 Proper orthogonal decomposition

The method of proper orthogonal decomposition (POD), along with Galerkin projection, is arguably the most widely used method for model reduction of fluid systems. POD was originally introduced for fluid problems by Lumley (1970) for extracting dominant coherent structures in turbulent flows. It is a method for obtaining an optimal basis for modal expansion of a given data-set, obtained either from experiments or numerical simulations. In the context of model reduction described in section 2.1, we can think of POD as a method for computing the subspace $\mathcal{X}_r$ to which the original dynamics is restricted. It computes this subspace by solving an optimization problem that maximizes the energy or the L^2-norm of the orthogonal projection of a given data-set. Although we restrict our attention to a finite-dimensional system, the method can be extended to infinite dimensional systems; see Holmes *et al.* (1996) for a rigorous treatment. Given a data-set $\{x_i\}_{i=1}^m$, snapshots from it are first stacked in a matrix X:

$$X = \begin{pmatrix} x_1 & x_2 & \dots & x_m \end{pmatrix}. \tag{2.10}$$

The optimization problem is that of obtaining an orthogonal projection $\mathbb{P}_\perp$ such that, on average, the norm of the error between the original and the projected datasets is minimized:

$$\frac{1}{m}\sum_{i=1}^{m} \|x_i - \mathbb{P}_\perp x_i\|_{\mathcal{X}}, \tag{2.11}$$

where $\|\cdot\|_{\mathcal{X}}$ is the norm induced by $\langle\cdot,\cdot\rangle_{\mathcal{X}}$. By calculus of variations, this leads to a symmetric eigenvalue problem

$$XX^*\Theta = \Theta\Lambda. \tag{2.12}$$

Since XX^* is symmetric, the eigenvalues λ_i (diagonal elements of Λ) are positive (or zero) and the corresponding eigenvectors θ_i (columns of Θ) are orthonormal. These eigenvectors are called the POD modes and the optimal projection is given by $\mathbb{P}_\perp = \Theta\Theta^*$. Further, the eigenvalues λ_i are directly proportional to the energy content (or norm) of the corresponding POD mode θ_i, and thus give a physical criterion for truncating the modal expansion at a low order. The eigenvalue problem (2.12) is too expensive if the vectors x_i are large-dimensional ($XX^* \in \mathbb{R}^{n\times n}$), as is typically the case for fluid flows. A computational algorithm using a method of snapshots developed by Sirovich (1987), takes advantage of the fact that the number of snapshots $m \ll n$. Instead of solving (2.12), one solves the eigenvalue problem

$$X^*XU = U\Lambda, \tag{2.13}$$

where now $X^*X \in \mathbb{R}^{m\times m}$, which is tractable and now $\Lambda \in \mathbb{R}^{m\times m}$. The leading m eigenvalues resulting from (2.12) and (2.13) are the same, and the POD modes can then be computed using

$$\Theta = XU\Lambda^{-1/2}. \tag{2.14}$$

For obtaining reduced-order models, the subspace $\mathcal{X}_r$ to restrict the dynamics is chosen to be the span of the energetically dominant r POD modes. Then, Galerkin projection is often employed to project the governing equations, which are in general nonlinear, onto the POD modes. In Galerkin projection, the governing equations are projected orthogonally onto the span of POD modes. From Fig. 2.1, it means that the spaces $\mathcal{Z}_r$ and $\mathcal{X}_r$ are identical and represented by the same basis given by POD modes Θ_r. A main disadvantage of the POD/Galerkin is that it often does not capture the *dynamics* of the original system; this has been shown in many studies on modeling various fluid flows, for example, flow past a cylinder by Deane *et al.* (1991) and Noack *et al.* (2003), plane Couette flow by Smith (2003), linearized channel flow by Ilak & Rowley (2008). Now, using this technique, the reduced-order model (2.4) of the linear system (2.1) becomes

$$\dot{a} = \Theta^* A\Theta a + \Theta^* Bu, \qquad y = C\Theta a. \tag{2.15}$$

As it was shown by Rowley (2005) and will be discussed later, if the data-set (2.10) is chosen from an impulse response simulation of (2.1), and appropriately scaled, the POD modes capture the most controllable modes and the resulting models capture the effect of actuation. However, the effect of the choice of sensors is still not captured by this method. Also, the resulting models are not guaranteed to be stable after truncating at a low order. The balanced truncation technique, described in the next section, precisely captures the effect of both actuation and sensing, and "balances" their effect in the resulting reduced models, and guarantees stability.

2.1.3 Exact balanced truncation: stable systems

The exact balanced truncation procedure was developed by Moore (1981) and is valid only for *stable* systems of the form (2.1). This method uses the concepts of controllability and observability of a system, and starts with defining the controllability and observability Gramians of the system (2.1) as follows:

$$W_c = \int_0^\infty e^{At} B B^* e^{A^* t}\, dt \tag{2.16}$$

$$\text{and} \quad W_o = \int_0^\infty e^{A^* t} C^* C e^{At}\, dt, \tag{2.17}$$

where asterisks are used to denote adjoint operators, defined by

$$\langle Bu, x\rangle_{\mathcal{X}} = \langle u, B^* x\rangle_{\mathcal{U}}, \qquad \forall u \in \mathcal{U} \quad \text{and} \quad \forall x \in \mathcal{X}, \tag{2.18}$$

$$\langle Cx, y\rangle_{\mathcal{Y}} = \langle x, C^* y\rangle_{\mathcal{X}}, \qquad \forall y \in \mathcal{Y} \quad \text{and} \quad \forall x \in \mathcal{X}. \tag{2.19}$$

The Gramians (2.16,2.17) have a nice physical interpretation. For controllability, the minimum amount of input energy required to drive the system from the origin at time $t = -\infty$ to a state x_0 at $t = 0$ is given by $\|u\|_{\mathcal{U}}^2 = x_0^* W_c^{-1} x_0$. The states that can be reached using the least input energy are the most controllable states, and geometrically, they can be represented by the major axes of the ellipsoid $x^* W_c x = 1$, while the minor axes represent the least controllable states; see Fig. 2.2. On the other hand, the output energy excited by the system starting at state x_0 is given by $\|y\|_{\mathcal{Y}}^2 = x_0^* W_o x_0$. The states that excite the largest output energy are most observable and are given by the major axes of $x^* W_o x = 1$.

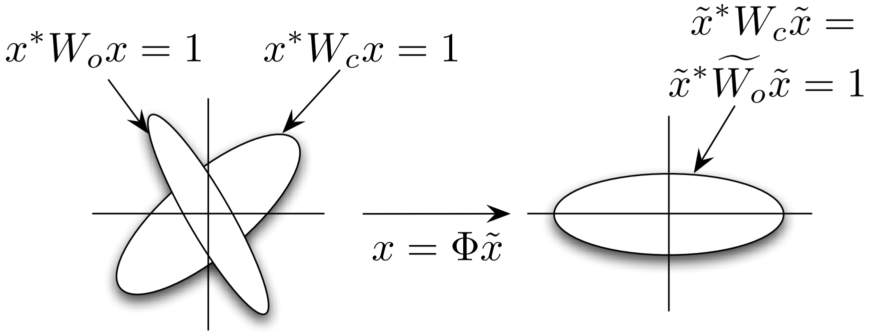
$x^* W_o x = 1$
$x^* W_c x = 1$
$\tilde{x}^* \widetilde{W_c} \tilde{x} =$
$\tilde{x}^* \widetilde{W_o} \tilde{x} = 1$
$x = \Phi \tilde{x}$

Figure 2.2: A two-dimensional caricature of the balanced transformation of the controllability and observability Gramians.

Balancing is referred to as a transformation of the system (2.1, 2.2) to different coordinates in which the controllability and observability Gramians (2.16, 2.17) are equal and diagonal. It is always possible to find such a transformation if the system is both controllable and observable. Thus, in the balanced coordinates, the most controllable and the most observable states coincide and a reduced model can be obtained by simply truncating the least controllable and observable modes. If the balanced transformation is given by $x = \Phi\tilde{x}$, the Gramians in the new coordinates are given by

$$\widetilde{W_c} = \Phi^{-1} W_c (\Phi^{-1})^*, \qquad \widetilde{W_o} = \Phi^* W_c \Phi, \tag{2.20}$$

$$\text{and} \qquad \widetilde{W_c} = \widetilde{W_o} = \Sigma, \tag{2.21}$$

where $\Sigma \in \mathbb{R}^{n\times n}$ is diagonal, whose entries $\sigma_i \geq 0$ decrease monotonically; they are called the Hankel singular values (HSVs) and are directly related to the controllability and observability of the corresponding states; see Fig. 2.2. A reduced-order model is obtained by truncating the states with relatively small HSVs, that is, the states which are almost uncontrollable and unobservable. Further, the HSVs are independent of the choice of the coordinates and are given by the eigenvalues of the product of the Gramians $W_c W_o$, while the (appropriately scaled) eigenvectors give the balancing transformation.

The main advantage of balanced truncation over the previously described methods is that it captures both the actuation and sensing. The resulting reduced model is guaranteed to be stable, provided that the truncation does not take place at an order between two equal HSVs. Also, there exist rigorous error bounds for the accuracy of the reduced model. In particular, if $G(t)$ is the input-ouput impulse response of (2.1,2.2) and $G_r(t)$ is the impulse response of the balanced system (2.4, 2.5) truncated at an order r, the error is given by

$$\|G(t) - G_r(t)\|_\infty < 2 \sum_{i=r+1}^{\infty} \sigma_i. \tag{2.22}$$

A disadvantage of the exact balanced truncation method is that it is not tractable for large-dimensional systems as it involves solution of large matrix Lyapunov equations to compute the Gramians; we now describe an approximate technique developed by Rowley (2005).

2.1.4 Approximate balanced truncation: stable systems

For systems of large dimension such as those encountered here, the Gramians (2.16, 2.17) are huge matrices which cannot be easily computed or stored. A computationally tractable procedure was introduced by Rowley (2005) for obtaining an approximate balancing transformation. The procedure relies on an approximate expression of the Gramians which was introduced by Moore (1981), which can be arrived at by observing that the impulse response of (2.1) is given by $\mathbf{x}(t) = \exp(At)B$, where columns of $\mathbf{x}(t) \in \mathbb{R}^{n\times p}$ are states obtained from the response of (2.1) to an impulse to the corresponding element of input u. The controllability Gramian (2.16) can be written in terms of this impulse response as

$$W_c = \int_0^\infty (\mathbf{x}\mathbf{x}^*)\, dt. \tag{2.23}$$

If the snapshots from this impulse response are sampled at equal time intervals δ_t and stacked in a matrix $X \in \mathbb{R}^{n\times pm_c}$ (after scaling),

$$\begin{aligned} X &= \sqrt{\delta_t}\begin{pmatrix}\mathbf{x}_1 & \mathbf{x}_2 & \dots & \mathbf{x}_{m_c}\end{pmatrix} && (2.24)\\ &= \sqrt{\delta_t}\begin{pmatrix}e^{At_1}B & e^{At_2}B & \dots & e^{At_{m_c}}B\end{pmatrix}. && (2.25)\end{aligned}$$

the integral in (2.23) can be approximated by the quadrature sum

$$W_c \approx XX^*. \tag{2.26}$$

In general, the snapshots need not be sampled at equal time intervals, in which case each snapshot needs to be scaled differently by the appropriate quadrature factor. As pointed out by Rowley (2005), if the dataset (2.24) is used in (2.10) for computing POD modes, the resulting modes are the leading controllable modes; thus POD captures the effect of actuation but not sensing.

The observability Gramian can also be approximated in a similar way. We first define the adjoint state-space system of (2.1,2.2):

$$\begin{aligned} \dot z &= A^*z + C^*v, && (2.27)\\ w &= B^*z, && (2.28)\end{aligned}$$

where the adjoint matrices are given by (2.18, 2.19). The observability Gramian can be written in terms of the impulse response $\mathbf{z}(t) = \exp(A^*t)C^*$ of (2.27), where columns of $\mathbf{z}(t) \in \mathbb{R}^{n\times q}$ are states obtained from the response of (2.27) to an impulse to the corresponding element of input v:

$$W_o = \int_0^\infty (\mathbf{z}(t)\mathbf{z}(t)^*)\, dt. \tag{2.29}$$

If the snapshots of the impulse response are again sampled at equal time intervals δ_t and stacked in a matrix $Z \in \mathbb{R}^{n\times qm_o}$,

$$\begin{aligned} Z &= \sqrt{\delta_t}\begin{pmatrix}\mathbf{z}_1 & \mathbf{z}_2 & \dots & \mathbf{z}_{m_o}\end{pmatrix} && (2.30)\\ &= \sqrt{\delta_t}\begin{pmatrix}e^{A^*t_1}C^* & e^{A^*t_2}C^* & \dots & e^{A^*t_{m_o}}C^*\end{pmatrix} && (2.31)\end{aligned}$$

the integral in (2.29) can be approximated by

$$W_o \approx ZZ^*. \tag{2.32}$$

The approximate Gramians (2.26, 2.32) are huge dimensional and not actually computed due to the large storage cost, but the leading columns (or modes) of the transformation that balances these Gramians are computed using a cost-efficient algorithm similar to the method of snapshots using POD. It involves computing the singular value decomposition of

$$Z^*X = U\Sigma V^* = \begin{pmatrix} U_1 & U_2 \end{pmatrix} \begin{pmatrix} \Sigma_1 & 0 \\ 0 & \Sigma_2 \end{pmatrix} \begin{pmatrix} V_1^* \\ V_2^* \end{pmatrix}, \tag{2.33}$$

where $\Sigma_1 \in \mathbb{R}^{r\times r}$ is a diagonal matrix of the most significant HSVs greater than a cut-off which is a modeling parameter, while $\Sigma_2 \in \mathbb{R}^{(n-r)\times(n-r)}$ is a diagonal matrix of smaller and zero HSVs. Note that $Z^*X \in \mathbb{R}^{qm_o \times pm_c}$ is a relatively small matrix, where m_c and m_o are the number of snapshots of the impulse responses of systems (2.1) and (2.27), to each input, respectively. For fluid systems that we are interested in, the typical number of snapshots is $O(10^{2-4})$, thus resulting in a reasonable computational cost, and typically $r \leq 100$. The leading columns and rows of the balancing transformation and its inverse are obtained using:

$$\Phi = XV_1\Sigma_1^{-1/2} \quad \text{and} \quad \Psi = ZU_1\Sigma_1^{-1/2}, \tag{2.34}$$

where $\Phi, \Psi \in \mathbb{R}^{n\times r}$, and the two sets of modes are bi-orthogonal; that is, $\Psi^*\Phi = I_r$. The columns of Φ and Ψ are called the balancing and adjoint modes respectively. The reduced-order model is obtained by using the expressions (2.34) in the general model (2.4, 2.5). Thus, the subspaces $\mathcal{X}_r$ and $\mathcal{Z}_r$ in Fig. 2.1 are given by linear combinations of snapshots obtained from the forward and adjoint impulse responses.

Another comparison with POD was obtained by Rowley (2005): the models are the same as those obtained using POD/Galerkin method of section 2.1.2 if the inner-product used in the eigenvalue problem (2.13) is weighted by the observability Gramian (2.17).

Output projection

When the number of outputs of the system (rows of C) is large, the algorithm described in section 2.1.4 can become intractable. The reason for this is that it involves one simulation of the adjoint system (2.27) for each component of v, the dimension of which is the same as the number of outputs. This number is often large in fluids systems where a good model needs to capture the response of the entire system to a given input ($C = I$). To overcome this problem, Rowley (2005) proposed a technique called *output projection*, which involves projecting the output y of (2.1, 2.2) onto a small number of energetically important modes obtained using POD. Let the columns of $\Theta \in \mathbb{R}^{q\times m}$ consist of the leading m POD modes of the dataset consisting of the *outputs* obtained from an impulse response of (2.1, 2.2). Then, for the purpose of obtaining a reduced-order model, the output (2.2) is approximated by

$$y = \Theta\Theta^* Cx, \tag{2.35}$$

where $\Theta\Theta^*$ is an orthogonal projection of the output onto the first m POD modes. The resulting output-projected system is optimally close (in the L^2-sense) to the original system, for an output of fixed rank m. With this approximation, only m adjoint simulations are required to approximate the observability Gramian; refer to Rowley (2005) for details. The number of POD modes m for output projection is a design parameter: for instance, one might choose this so that the first m modes capture at least 90% of the output energy. In the rest of this dissertation, the models resulting from this approximation of the output are referred to as *m-mode output projected models.*

The reduced-order model of the output-projected system is then given by

$$\dot{a} = \Psi^* A \Phi a + \Psi^* B u, \tag{2.36}$$

$$y = \Theta\Theta^* C \Phi a. \tag{2.37}$$

2.2 Balanced truncation: unstable systems

2.2.1 Exact method

We briefly describe a model reduction procedure using the balanced truncation method for unstable systems developed by Zhou *et al.* (1999). The eigenvalues of A are assumed to be anywhere on the complex plane, except on the imaginary axis. For unstable systems, the integrals in (2.16, 2.17) are unbounded and hence the Gramians are ill-defined. A modified technique was proposed by Zhou *et al.* (1999) based on the following frequency-domain definitions of the Gramians:

$$W_c = \frac{1}{2\pi}\int_{-\infty}^{\infty} (j\omega I - A)^{-1} B B^* (-j\omega I - A^*)^{-1}\, d\omega, \tag{2.38}$$

$$W_o = \frac{1}{2\pi}\int_{-\infty}^{\infty} (-j\omega I - A^*)^{-1} C^* C (j\omega I - A)^{-1}\, d\omega. \tag{2.39}$$

By using Parseval's theorem, it can be shown that for stable systems, the frequency-domain definitions (2.38, 2.39) are equivalent to the time-domain definitions (2.16, 2.17). The model-reduction procedure of Zhou *et al.* (1999) begins by first transforming the system (2.1) to coordinates in which the stable and unstable dynamics are decoupled. That is, let T be a transformation such that if $x = T\tilde{x}$, the system (2.1, 2.2) transforms to

$$\dot{\tilde{x}} = \frac{d}{dt}\begin{pmatrix} \tilde{x}_u \\ \tilde{x}_s \end{pmatrix} = \begin{pmatrix} A_u & 0 \\ 0 & A_s \end{pmatrix} \tilde{x} + \begin{pmatrix} B_u \\ B_s \end{pmatrix} u \tag{2.40}$$

$$y = \begin{pmatrix} C_u & C_s \end{pmatrix} \tilde{x}. \tag{2.41}$$

Here, A_u and A_s are such that all their eigenvalues are in the right- and left-half complex planes respectively, while $\tilde{x}_u$ and $\tilde{x}_s$ are the corresponding states. Next, denote the controllability and observability Gramians corresponding to the set (A_s, B_s, C_s) describing the stable dynamics by W_c^s and W_o^s respectively. Similarly, denote the

Gramians corresponding to the set $(-A_u, B_u, C_u)$ by W_c^u and W_o^u. The Gramians of the original system (2.1, 2.2) are then related to those corresponding to the two subsystems by:

$$W_c = T \begin{pmatrix} W_c^u & 0 \\ 0 & W_c^s \end{pmatrix} T^* \tag{2.42}$$

$$\text{and} \quad W_o = (T^{-1})^* \begin{pmatrix} W_u^u & 0 \\ 0 & W_u^s \end{pmatrix} T^{-1}. \tag{2.43}$$

A system is said to be balanced if its Gramians defined by (2.42, 2.43) are equal and diagonal, in which case the diagonal entries are called the *generalized* Hankel singular values. A reduced-order model is obtained by truncating the states with small generalized HSVs.

A physical interpretation of the Gramians (2.42, 2.43) was also given by Zhou *et al.* (1999) and is as follows. The sum of the minimum input energies required to drive the system from the origin at time at $t = -\infty$ to a state x_0 at $t = 0$ and back to the origin at $t = \infty$ is given by $\|u\|_{\mathcal{U}}^2 = x_0^* W_c^{-1} x_0$. For observability, if the system (2.1, 2.2) is started with an initial condition x_0 and with no control input, the sum of the output energies: (a) excited on the stable subspace of A in forward time $t = (0, \infty)$, and (b) excited on the unstable subspace of A in the time interval $t = (-\infty, 0)$, is given by $\|y\|_{\mathcal{Y}}^2 = x_0^* W_o x_0$.

The properties of balanced truncation for stable systems described in section 2.1.3 extend to unstable systems as well; the reduced system is guaranteed to have no eigenvalues on the imaginary axis provided that the balanced model is not truncated between two equal generalized HSVs. Also, the error bound (2.22) holds for unstable systems, but with the time-domain impulse response $G(t)$ replaced by its frequency-domain counterpart $G(s)$ (which is the transfer-function from u to y). This is because, for unstable systems, $G(t)$ grows without bound, however, the ∞-norm is well-defined if the transfer function $G(s)$ is used.

A disadvantage of reducing an unstable system based on generalized HSVs is that an unstable mode, if it is almost uncontrollable or unobservable, might get truncated. Thus the reduced model will not capture all the instabilities, which might be undesirable for control. In the next section, we develop an approximate algorithm which differs from the approach of Zhou *et al.* (1999) in this respect; the proposed method treats the unstable dynamics exactly and obtains a reduced model of the stable dynamics.

2.2.2 Approximate method

The approximate balancing procedure described in section 2.1.4, which is essentially a snapshot-based method, does not extend to unstable systems since the impulse responses of (2.1) and (2.27) are unbounded. We could consider applying the algorithm to the two sub-systems given in (2.40), but the transformation T that decouples (2.1) itself is not available. However, when the dimension of the unstable sub-system is small, we show that it is not necessary to compute the entire transformation T and it is still possible to obtain an approximate balancing transformation. Here, we present an algorithm for computing such a transformation and also show that it essentially results in a method that is a variant of the technique of Zhou *et al.* (1999) presented in section 2.2.1. The idea behind the algorithm is to first project the original system (2.1) onto the still high-dimensional stable subspace of A. Then, one obtains a reduced-order model of the projected system using the snapshot-based procedure described in section 2.1.4. The dynamics projected onto the unstable subspace can be treated exactly on account of its low dimensionality.

We assume that the number of unstable eigenvalues n_u is $O(10)$ and can be computed numerically, say using the computational package ARPACK developed by Lehoucq *et al.* (1998). We further assume that the bases for the right and the left unstable eigenspaces $\Phi_u, \Psi_u \in \mathbb{R}^{n \times n_u}$, defined as in (2.8), can be computed. For the algorithm, we need the following projection operator onto the stable subspace of A:

$$\mathbb{P}_s = I - \Phi_u \Psi_u^*, \tag{2.44}$$

where Φ_u and Ψ_u have been scaled such that $\Psi_u^* \Phi_u = I_{n_u}$. We use the operator $\mathbb{P}_s$ to obtain the dynamics of (2.1) restricted to the stable subspace of A as follows:

$$\dot{x}_s = \mathbb{P}_s A x_s + \mathbb{P}_s B u, \tag{2.45}$$

$$y_s = C \mathbb{P}_s x_s \tag{2.46}$$

where $x_s = \mathbb{P}_s x$. The adjoint of (2.45, 2.46) is the same as the dynamics of (2.27, 2.28) restricted to the stable subspace of A^* using $\mathbb{P}_s^*$, and is given by

$$\dot{z}_s = \mathbb{P}_s^* A^* z_s + \mathbb{P}_s^* C^* v, \tag{2.47}$$

$$w_s = B^* \mathbb{P}_s^* z_s, \tag{2.48}$$

where $z_s = \mathbb{P}_s^* z$. Then, as shown in appendix A, balancing the stable part of the Gramians W_c and W_o defined in (2.42, 2.43) (balancing W_c^s and W_o^s) is the same as balancing the Gramians of the stable subsystem (2.45, 2.46).

We use the procedure of section 2.1.4 to obtain a transformation that balances the Gramians of the stable subsystem (2.45, 2.46). We first compute the state-impulse responses of (2.45) and (2.47) and stack the resulting snapshots x_s and z_s in matrices X_s and Z_s respectively. As in (2.33), we compute the singular value decomposition of $Z_s^* X_s$ and use the expressions (2.34) to obtain the balancing modes Φ_s and the adjoint modes Ψ_s, where again $\Psi_s^* \Phi_s = I_r$. The reduced-order modes are obtained by expressing the state x as

$$x = \Phi_u a_u + \Phi_s a_s, \tag{2.49}$$

where $a_u \in \mathbb{R}^{n_u}$ and $a_s \in \mathbb{R}^r$. Substituting (2.49) in (2.1) and pre-multiplying by Ψ_u^* and Ψ_s^*, we obtain

$$\frac{da}{dt} \equiv \frac{d}{dt}\begin{pmatrix} a_u \\ a_s \end{pmatrix} = \begin{pmatrix} \Psi_u^* A \Phi_u & \Psi_u^* A \Phi_s \\ \Psi_s^* A \Phi_u & \Psi_s^* A \Phi_s \end{pmatrix} \begin{pmatrix} a_u \\ a_s \end{pmatrix} + \begin{pmatrix} \Psi_u^* \\ \Psi_s^* \end{pmatrix} Bu \tag{2.50}$$

$$y = C(\Phi_u a_u + \Phi_s a_s) \equiv \begin{pmatrix} C\Phi_u & C\Phi_s \end{pmatrix} a. \tag{2.51}$$

Now, since the unstable subspace is invariant ($\mathrm{range}(A\Phi_u) \subseteq \mathrm{span}(\Phi_u)$), we can write $A\Phi_u = \Phi_u \Lambda$ for some $\Lambda \in \mathbb{R}^{n_u \times n_u}$, and using the properties of eigenvectors, we have $\Psi_s^* A \Phi_u = \Psi_s^* \Phi_u \Lambda = 0$. Similarly, it can be shown that $\Psi_u^* A \Phi_s = 0$. Thus, the cross terms in (2.50) are zero and the reduced-order model is

$$\begin{aligned} \frac{da}{dt} &= \begin{pmatrix} \Psi_u^* A \Phi_u & 0 \\ 0 & \Psi_s^* A \Phi_s \end{pmatrix} \begin{pmatrix} a_u \\ a_s \end{pmatrix} + \begin{pmatrix} \Psi_u^* \\ \Psi_s^* \end{pmatrix} Bu \\ &\overset{\text{def}}{=} \begin{pmatrix} \widetilde{A}_u & 0 \\ 0 & \widetilde{A}_s \end{pmatrix} \begin{pmatrix} a_u \\ a_s \end{pmatrix} + \begin{pmatrix} \widetilde{B}_u \\ \widetilde{B}_s \end{pmatrix} u \end{aligned} \tag{2.52}$$

$$y = C(\Phi_u a_u + \Phi_s a_s) \overset{\text{def}}{=} \begin{pmatrix} \widetilde{C}_u & \widetilde{C}_s \end{pmatrix} a. \tag{2.53}$$

The procedure described so far to obtain the reduced-order model (2.52, 2.53) is related to the procedure of Zhou *et al.* (1999) described in section 2.2.1. It can be shown that the transformation that balances the Gramians defined by (2.42, 2.43) results in a system in which the unstable and stable dynamics are decoupled. Furthermore, the resulting stable dynamics are the same as those given by the equations describing the a_s-dynamics of (2.52). The difference is that, in our algorithm, the unstable dynamics are not balanced, while they are in Zhou *et al.* (1999). Further, our approach does not explicitly compute the stable subsystem A_s, since it is not tractable for large systems. A disadvantage of Zhou's approach is that an unstable mode might be truncated resulting in a model which does not capture all the unstable modes, which is undesirable for control purposes.

Output projection for the stable subspace

For systems with a large number of outputs, the number of adjoint simulations (2.47) can become intractable; however, the output projection of section 2.1.4 can readily be extended to unstable systems. Instead of projecting the entire output y onto POD modes, we first express the state $x = x_u + x_s$, where $x_u = (I - \mathbb{P}_s)x$ and $x_s = \mathbb{P}_s x$ are projections on the unstable and stable subspaces of A respectively. We similarly express the output as $y = y_u + y_s = C(x_u + x_s)$. We then project the component y_s onto a small number of POD modes, of the data set consisting of the outputs from an impulse response of (2.45, 2.46). If the POD modes are represented as columns of the matrix $\Theta_s \in \mathbb{R}^{q \times m}$, the output of (2.1, 2.2) is approximated by

$$y = \big[C(I - \mathbb{P}_s) + \Theta_s \Theta_s^* C \mathbb{P}_s\big] x = Cx_u + \Theta_s \Theta_s^* C x_s. \tag{2.54}$$

Finally, with the state x expressed by the modal expansion (2.49), the output of the reduced-order model (2.52) is given by

$$y = \begin{pmatrix} C\Phi_u & \Theta_s\Theta_s^* C\Phi_s \end{pmatrix} \begin{pmatrix} a_u \\ a_s \end{pmatrix}. \tag{2.55}$$

2.2.3 Algorithm

The steps involved in obtaining reduced-order models of (2.1), for the case with a large number of outputs, can now be summarized as follows:

1. Compute the unstable eigenvectors Φ_u and Ψ_u of the linearized and adjoint systems.
2. Project the original system (2.1, 2.2) onto the subspace spanned by the stable eigenvectors of A in the direction of the unstable eigenvectors of A to obtain (2.45, 2.46). Compute the state and output responses from an impulse on each input of (2.45) and stack the *state* snapshots $\{x_s(t_i)\}$ in a matrix X_s.
3. Assemble the resulting *output* snapshots $\{y_s(t_i)\}$, and compute the POD modes θ_j of the resulting data-set. These POD modes are stacked as columns of Θ_s.
4. Choose the number of POD modes one wants to use to describe the output (2.46). For instance, if 10% error is acceptable, and the first m POD modes capture 90% of the energy, then the output is the velocity field projected onto the first m modes. Thus, the output is represented as $y_s = \Theta_s^* C x_s$.
5. Project the adjoint system (2.27, 2.28) onto the subspace spanned by the stable eigenvectors of A^* in the direction of the unstable eigenvectors of A^* to obtain (2.47, 2.48). Compute the (state) response of (2.47), starting with each POD mode θ_j as the initial condition (one simulation for each of the first m modes). Stack the snapshots $\{z_s(t_i)\}$ in a matrix Z_s.
6. Compute the singular value decomposition $H = Z_s^* X_s^* = U_s \Sigma_s V_s^*$; let U_r and V_r be the leading r columns of U_s and V_s and let $\Sigma_r \in \mathbb{R}^{r\times r}$ contain the leading rows and columns of Σ_s.
7. Define balancing modes ϕ_j^s and the corresponding adjoint modes ψ_j^s as columns of the matrices Φ_s and Ψ_s, where

$$\Phi_s = X_s V_r \Sigma_r^{-1/2}, \qquad \Psi_s = Y_s U_r \Sigma_r^{-1/2}. \tag{2.56}$$

8. Obtain the reduced-order model using (2.52), which can be written as

$$\frac{da}{dt} = \begin{pmatrix} \widetilde{A}_u & 0 \\ 0 & \widetilde{A}_s \end{pmatrix} a + \begin{pmatrix} \widetilde{B}_u \\ \widetilde{B}_s \end{pmatrix} u \overset{\text{def}}{=} \widetilde{A}a + \widetilde{B}u, \tag{2.57}$$

$$y = \begin{pmatrix} \widetilde{C}_u & \widetilde{C}_s \end{pmatrix} a \overset{\text{def}}{=} \widetilde{C}a \qquad \text{where,} \tag{2.58}$$

$$a = \begin{pmatrix} a_u \\ a_s \end{pmatrix}, \tag{2.59}$$

$$\widetilde{A}_u = \Psi_u^* A \Phi_u, \quad \widetilde{B}_u = \Psi_u^* B, \quad \widetilde{C}_u = C\Phi_u, \tag{2.60}$$

$$\widetilde{A}_s = \Psi_s^* A \Phi_s, \quad \widetilde{B}_s = \Psi_s^* B, \quad \widetilde{C}_s = \Theta_s \Theta_s^* C \Phi_s. \tag{2.61}$$

When the output is the entire state or $C = I$, the entire field can be reconstructed by measuring the coefficients of the unstable modes a_u and the POD modes Θ_s of the stable subspace. That is, the output (2.58) can be represented as

$$y = \begin{pmatrix} \widehat{C}_u & 0 \\ 0 & \widehat{C}_s \end{pmatrix} \begin{pmatrix} a_u \\ a_s \end{pmatrix} \overset{\text{def}}{=} \widehat{C}a, \qquad \text{where,} \tag{2.62}$$

$$\widehat{C}_u = I_{n_u}, \quad \widehat{C}_s = \Theta_s^* \Phi_s. \tag{2.63}$$

Finally, if the initial state x_0 is known, the initial condition of (2.57) can be obtained using

$$a_0 = \begin{pmatrix} \Psi_u & \Psi_s \end{pmatrix}^* x_0. \tag{2.64}$$

2.3 Eigensystem Realization Algorithm (ERA)

Here, we develop a technique for reducing the computational cost of the approximate balanced truncation described in section 2.1.3. The method requires impulse response simulations of the linear and adjoint systems given by (2.1) and (2.27) respectively, which are limited by the speed of the numerical solver. The next step is to compute the cross-correlation matrix Z^*X of the two sets of snapshots, as needed for the SVD in (2.33). We show that the cost of both these steps can be substantially reduced by adopting a system identification technique called the eigensystem realization algorithm (ERA) developed by Juang & Pappa (1985). We will see that, at a discrete-time level, ERA results in the same reduced-order model as approximate balanced truncation, and is feasible for experiments.

ERA is a method for model reduction of discrete-time, stable, linear time-invariant systems of the form

$$x_{k+1} = A_d x_k + B_d u_k \tag{2.65}$$

$$y_k = C_d x_k, \tag{2.66}$$

where we think of (2.65, 2.66) as being obtained from a temporal discretization of (2.1, 2.2). The discretization time-step Δt is assumed to be a constant, and the index k is used to represent various quantities at time $t = k\Delta t$. As in approximate balanced truncation, ERA begins by computing the impulse response of (2.65, 2.66), and the resulting outputs y_k are sampled every M time-steps. The ouputs can be compactly described by the Markov parameters given by

$$\mathbf{y}_k = C_d A_d^k B_d, \tag{2.67}$$

where $\mathbf{y}_k \in \mathbb{R}^{q\times p}$ is a matrix with elements y^{ij} which represent the ith output from an impulse on the jth input. The Markov parameters are sampled every M time-steps:

$$\begin{aligned} &\begin{pmatrix}\mathbf{y}_0 & \mathbf{y}_M & \mathbf{y}_{2M} & \cdots & \mathbf{y}_{(m_c+m_o)M}\end{pmatrix} && (2.68)\\ &=\begin{pmatrix}C_dB_d & C_dA_d^MB_d & C_dA_d^{2M}B_d & \dots & C_dA_d^{(m_c+m_o)M}B_d\end{pmatrix}. && (2.69)\end{aligned}$$

These outputs are used to assemble the Hankel matrix H as follows:

$$H = \begin{pmatrix} \mathbf{y}_0 & \mathbf{y}_M & \cdots & \mathbf{y}_{m_cM} \\ \mathbf{y}_M & \mathbf{y}_{2M} & \cdots & \mathbf{y}_{(m_c+1)M} \\ \vdots & \vdots & \ddots & \vdots \\ \mathbf{y}_{m_oM} & \mathbf{y}_{(m_o+1)M} & \cdots & \mathbf{y}_{(m_c+m_o)M} \end{pmatrix} \tag{2.70}$$

$$= \begin{pmatrix} C_dB_d & C_dA_d^MB_d & \dots & C_dA_d^{m_cM}B_d \\ C_dA_d^MB_d & C_dA_d^{2M}B_d & \dots & C_dA_d^{(m_c+1)M}B_d \\ \vdots & \vdots & \ddots & \vdots \\ C_dA_d^{m_oM}B_d & C_dA_d^{(m_o+1)M}B_d & \dots & C_dA_d^{(m_c+m_o)M}B_d \end{pmatrix}. \tag{2.71}$$

The reduced-order models are obtained by first computing the SVD of H

$$H = U\Sigma V^*. \tag{2.72}$$

Then, if U_r and V_r are the leading columns of U and V, and $\Sigma_r \in \mathbb{R}^{r\times r}$ contains the leading rows and columns of Σ, the reduced model of (2.65, 2.66) is given by

$$\begin{aligned} a_{k+1} &= A_r a_k + B_r u_k, && (2.73)\\ y_k &= C_r a_k && (2.74)\\ \text{where,}\quad A_r &= (\Sigma_r^{-\frac{1}{2}}U_r^*)\, H_1\, (V_r\Sigma_r^{-\frac{1}{2}}), && (2.75)\\ B_r &= (\Sigma_r^{-\frac{1}{2}}U_r^*)\ \mathrm{Col}_{\text{first}}(H), && (2.76)\\ C_r &= \mathrm{Row}_{\text{first}}(H)\,(V_r\Sigma_r^{-\frac{1}{2}}). && (2.77)\end{aligned}$$

In the above expressions, $\mathrm{Col}_{\text{first}}(H)$ and $\mathrm{Row}_{\text{first}}(H)$ represent the first block column and row of H respectively, and

$$H_1 = \begin{pmatrix} \mathbf{y}_1 & \mathbf{y}_{M+1} & \cdots & \mathbf{y}_{(m_c+1)M} \\ \mathbf{y}_{M+1} & \mathbf{y}_{2M+1} & \cdots & \mathbf{y}_{(m_c+2)M} \\ \vdots & \vdots & \ddots & \vdots \\ \mathbf{y}_{m_oM+1} & \mathbf{y}_{(m_o+1)M+1} & \cdots & \mathbf{y}_{(m_c+m_o)M+1} \end{pmatrix}. \tag{2.78}$$

Note that H_1 cannot be assembled from the building blocks given by (2.68) but needs the following additional Markov parameters:

$$\begin{aligned} &\begin{pmatrix} \mathbf{y}_1 & \mathbf{y}_{M+1} & \mathbf{y}_{2M+1} & \cdots & \mathbf{y}_{(m_c+m_o)M+1} \end{pmatrix} && (2.79) \\ = &\begin{pmatrix} C_dA_dB_d & C_dA_d^{M+1}B_d & C_dA_d^{2M+1}B_d & \ldots & C_dA_d^{(m_c+m_o)M+1}B_d \end{pmatrix}. && (2.80) \end{aligned}$$

Thus, pairs of output snapshots at consecutive time-steps $(kM, kM+1)$ for $k = 0, 1, \ldots, m_c + m_o$ are needed to compute the reduced model (2.73, 2.74).

2.3.1 Equivalence with approximate balanced truncation

For comparison with ERA, we first obtain reduced-order models of the discrete-time system (2.65, 2.66) using the approximate balanced truncation method. The algorithm, outlined in section 2.1.4 for continuous-time systems, is essentially the same for discrete-time systems. First, impulse response simulations are computed of the forward and adjoint systems and the resulting snapshots are stacked in matrices X and Z respectively, as in (2.25) and (2.31):

$$X = \begin{pmatrix} \mathbf{x}_1 & \mathbf{x}_2 & \ldots & \mathbf{x}_{m_c} \end{pmatrix} = \begin{pmatrix} A_d^{t_1}B & A_d^{t_2}B & \ldots & A_d^{t_{m_c}}B \end{pmatrix}, \tag{2.81}$$

$$Z = \begin{pmatrix} \mathbf{z}_1 & \mathbf{z}_2 & \ldots & \mathbf{z}_{m_o} \end{pmatrix} = \begin{pmatrix} (A_d^*)^{t_1}C^* & (A_d^*)^{t_2}C^* & \ldots & (A_d^*)^{t_{m_o}}C^* \end{pmatrix}. \tag{2.82}$$

The next step is to compute the SVD of the correlation matrix Z^*X and use the resulting factors to compute the balancing and adjoint modes. If the snapshots are sampled at times $t_i = (i-1)M$, we have from (2.81, 2.82) by direct calculation

$$Z^*X = H, \tag{2.83}$$

where H is the Hankel matrix (2.71) obtained using ERA. Thus the SVD factorization of Z^*X is given by (2.72) and can be used in expressions (2.34) to obtain the balancing modes Φ and the adjoint modes Ψ. Finally, the reduced model can be obtained by expressing the state $x_k = \Phi a_k$ and projecting the system (2.65, 2.66) onto the adjoint modes:

$$a_{k+1} = \Psi^*A_d\Phi a_k + \Psi^*B_du_k \tag{2.84}$$

$$y_k = C_d\Phi a_k. \tag{2.85}$$

For comparison with the models (2.73, 2.74) obtained using ERA, we substitute the expressions for Φ and Ψ from (2.34) in the reduced matrices obtained in (2.84, 2.85) and define:

$$A_r \overset{\text{def}}{=} \Psi^* A \Phi = (\Sigma_r^{-\frac{1}{2}} U_r^*)\,(Z^* A X)\,(V_r \Sigma_r^{-\frac{1}{2}}), \tag{2.86}$$

$$B_r \overset{\text{def}}{=} \Psi^* B = (\Sigma_r^{-\frac{1}{2}} U_r^*)\,(Z^* B), \tag{2.87}$$

$$C_r \overset{\text{def}}{=} C \Phi = (CX)\,(V_r \Sigma_r^{-\frac{1}{2}}). \tag{2.88}$$

Again by direct calculation, we obtain

$$Z^* A X = H_1, \qquad Z^* B = \mathrm{Col}_{\mathrm{first}}(H), \qquad CX = \mathrm{Row}_{\mathrm{first}}(H). \tag{2.89}$$

On substituting (2.89) in (2.86, 2.87, 2.88), we obtain expressions for the reduced matrices which are the same (2.75, 2.76, 2.77), that is, those obtained using ERA. Thus, the two methods theoretically result in the same reduced-order models for discrete-time systems.

Even though the two techniques theoretically result in identical reduced-order models, there are key differences in the computational steps involved, and both methods have their own advantages. The main advantages of ERA as compared to approximate balanced truncation are:

1. ERA requires only the Markov parameters (2.69, 2.80) which can be obtained from impulse response of the original system (2.65, 2.66). Thus, unlike approximate balanced truncation, it does not need any adjoint simulations, which makes it feasible for experiments. For instance, ERA has been used for system identification in flow control experiments by Cattafesta *et al.* (1997), Cabell *et al.* (2006).

2. Once the snapshots from impulse-response simulations have been obtained, the most computationally expensive step in approximate balanced truncation is the computation of the correlation matrix $Z^* X$ (2.83), which was shown to be the same as the Hankel matrix H defined in (2.71). The computation of each building-block of H requires pq inner-products, where p and q are the number of inputs and outputs of the system. In approximate balanced truncation, all the $(m_c+1) \times (m_o+1)$ blocks are obtained by computing inner-products of all the adjoint snapshots (2.82) with all the forward snapshots (2.81). In contrast, ERA requires the computation of only the first block-row and the last block-column of H and H_1, which are essentially the Markov parameters (2.69, 2.80) and require $2(m_c+m_o)$ inner-products. Thus, ERA results in an order-of-magnitude savings over approximate balanced truncation. As an example, if $m_c = m_o = 100$, the number of block-computations required using balanced truncation is 10^4, while that using ERA is 200 or only 2% of the former.

Although the approximate balanced truncation method is computationally more expensive, it has its own advantages over ERA:

1. Approximate balanced truncation provides the balancing and adjoint modes, which form the bases of the subspaces $\mathcal{X}_r$ and $\mathcal{Z}_r$ in Fig. 2.1, and can be used

to reconstruct the full state x_k from the reduced state a_k. These modes can also be useful for control design, as they highlight regions of the flow most receptive to actuation and sensing. ERA does not provide such modes, so the full state cannot be readily reconstructed. Theoretically, it is possible to obtain the reduced state from the full state by computing additional Markov parameters, but the procedure is computationally expensive as it requires the full simulation and thus defeats the purpose of model reduction.

2. Since balanced truncation provides the projection subspaces, reduced models of the governing nonlinear equations can also be obtained. Further, the parameters in the governing equations such as Reynolds number can be retained in the reduced models. Thus, the reduced models can in principle be used for a wide range of parameters; initial studies on the linearized channel flow by Ilak & Rowley (2008) show promise in this direction.

Chapter 3

Control of flow past a flat plate

The model-reduction techniques developed in chapter 2 are applied to develop controllers for a two-dimensional flow past a flat plate at low Reynolds number and large angle of attack. Numerical simulations are performed using the immersed boundary solver developed by Colonius & Taira (2008), which is adapted into a suite of computational tools for performing linearized and adjoint simulations, computing steady states and global eigenmodes, and developing reduced-order models suitable for control. We show that as the angle of attack is increased beyond 27°, the flow undergoes a Hopf bifurcation from steady state to periodic vortex shedding. For control, the actuation is modeled as a localized body force near the flat plate, and reduced models are developed of the dynamics linearized about an unstable steady state at $\alpha = 35°$. The models are used to design two different controllers, one based on full-state feedback and the other based on two near-wake velocity measurements. We include the controllers in the full nonlinear simulations and show that they are able to suppress the nonlinear vortex shedding, and thus are effective even in the regions of phase-space where the nonlinear effects are strong.

3.1 Immersed boundary projection method

The numerical scheme used is the fast immersed boundary projection method developed by Colonius & Taira (2008), which is an accelerated version of the technique developed by the same authors in Taira & Colonius (2007). The method is first described in this section and then adapted into linearized and adjoint formulations.

Consider the following form of the incompressible Navier-Stokes equations, based on the continuous analog of the immersed boundary formulation introduced by Peskin (1972):

$$\frac{\partial u}{\partial t} + u \cdot \nabla u = -\nabla p + \frac{1}{\mathsf{Re}} \nabla^2 u + \int f(\xi)\delta(\xi - x) d\xi, \tag{3.1}$$

$$\nabla \cdot u = 0, \tag{3.2}$$

$$u(\xi) = \int u(x,t)\delta(x - \xi) dx = u_B, \tag{3.3}$$

where u and p are the fluid velocity and pressure respectively. The force f acts as a Lagrange multiplier that imposes the no-slip boundary condition on the Lagrangian points ξ, which arise from the discretization of a body moving with the velocity u_B. We consider the body to be a stationary flat plate at an angle of attack α; that is, here $u_B = 0$. The variables u and x are non-dimensionalized with respect to the free stream velocity U and the flat plate chord length c, and the Reynolds number is defined as $\mathsf{Re} = Uc/\nu$ where ν is the kinematic viscosity. The other quantities p, f, and time t are consistently non-dimensionalized as well: time as Ut/c, pressure as $p/\rho U^2$ and the force as $f/\rho U^2 c$. Equations (3.1-3.3) are discretized in space using a second-order finite-volume scheme on a staggered grid, which results in the following semi-discrete equations:

$$M\frac{dq}{dt} + Gp - Hf = \mathcal{N}(q) + Lq + bc_1, \tag{3.4}$$

$$Dq = bc_2, \tag{3.5}$$

$$Eq = 0, \tag{3.6}$$

where q, p, and f are the discrete velocity flux, pressure, and force respectively. The operator $\mathcal{N}(q)$ is the discretized nonlinear term $u \cdot \nabla u$, L is the discrete Laplacian, and M is the diagonal mass matrix, which is the identity for a uniform grid. The operators G and D are the discrete gradient and divergence operators constructed such that $G = -D^T$, and the operators E and H are interpolation and regularization operators that smear the Dirac delta functions in equation (3.1) over a few grid points. In order to obtain a symmetric matrix in the Poisson solve, these operators are also constructed such that $E = -H^T$; see Taira & Colonius (2007) for details. The terms bc_1 and bc_2 depend on the particular choice of boundary conditions; as an example, for a 2-D flow past a stationary object, uniform flow conditions are applied at the inlet and at the lateral walls, while convective boundary conditions are applied at the outflow.

The equations are (3.4, 3.5, 3.6) are then discretized in time using an implicit trapezoidal scheme for the linear terms and the second-order accurate Adams-Bashforth for the nonlinear terms. The resulting algebraic equations are solved using a fractional-step (or projection or operator-splitting) algorithm to march the variables forward in time. The key feature of this technique of Taira & Colonius (2007) is that the pressure p and the force f are combined together as a single Lagrange multiplier $\lambda = (p, f)$, which in turn is obtained by solving a single modified Poisson equation.

A fast algorithm of the above immersed boundary method was developed by Colonius & Taira (2008) by employing a nullspace approach and a multi-domain method for applying the far-field boundary conditions. The discrete streamfinction s is introduced, which is related to the flux q by a discrete curl operation C constructed as the nullspace of the divergence D:

$$q = Cs, \quad \text{where,} \quad DC \equiv 0. \tag{3.7}$$

Thus, the incompressibility condition (3.5) is satisfied at all times. The transpose operator C^T relates the discrete circulation γ to the discrete flux by:

$$\gamma = C^T q. \tag{3.8}$$

Pre-mutliplying (3.4) by C^T eliminates the pressure, since $C^T G = -C^T D^T = 0$, resulting in a semi-discrete formulation in terms of the circulation γ:

$$\frac{d\gamma}{dt} + C^T E^T \tilde{f} = -\beta C^T C\gamma + C^T \mathcal{N}(q) + bc_\gamma, \tag{3.9}$$

$$ECs = u_B, \tag{3.10}$$

where a uniform grid is assumed ($M = I$) for achieving computational speed-up using fast Sine transforms. In (3.9), the discrete Laplacian is represented by $-C^T C\gamma$, using the identity $\nabla^2\gamma = \nabla(\nabla\cdot\gamma) - \nabla\times(\nabla\times\gamma) = -\nabla\times(\nabla\times\gamma)$; the constant $\beta = 1/\mathsf{Re}\Delta^2$, where Δ is the uniform grid spacing. The nonlinear term $\mathcal{N}(q)$ can also be represented as the spatial discretization of $q \times \gamma$. From (3.7) and (3.8), the discrete stream function s and circulation γ are related by

$$s = (C^T C)^{-1}\gamma. \tag{3.11}$$

The boundary conditions specified are Dirichlet and Neumann for the velocity components normal and tangential to the domain boundaries, which for the flow past a flat plate imply a uniform-flow in the far-field. With a uniform grid and these boundary conditions, the Laplacian $C^T C$ can be diagonalized using the fast Sine transform:

$$L = C^T C = S\Lambda S, \tag{3.12}$$

where, S is the symmetric operator representing the discrete Sine transform and Λ is a diagonal matrix containing eigenvalues of $C^T C$. Equations (3.9, 3.10) are then discretized in time, using the trapezoidal rule for the linear terms and the second-order Adams-Bashforth for the nonlinear terms to obtain the time-stepping scheme:

$$\begin{aligned} S\Big(1 + \frac{\beta\Delta t}{2}\Lambda\Big)S\gamma^* &= \Big(I - \frac{\beta\Delta t}{2}C^T C\Big)\gamma^n && (3.13)\\ &\quad + \frac{\Delta t}{2}\Big(3\mathcal{N}(q^n) - \mathcal{N}(q^{n-1})\Big) + \Delta t bc_\gamma, \\ EC\Big(S\Lambda^{-1}\Big(1 + \frac{\beta\Delta t}{2}\Lambda\Big)^{-1}S\Big)(EC)^T\tilde{f} &= ECS\Lambda^{-1}S\gamma^* - u_B^{n+1}, && (3.14)\\ \gamma^{n+1} &= \gamma^* - S\Big(1 + \frac{\beta\Delta t}{2}\Lambda\Big)^{-1}S(EC)^T\tilde{f}, && (3.15)\end{aligned}$$

where the index n represents the fields at time $t_n = n\Delta t$. The dimension of the Poisson solve (3.14), for the force $\tilde{f}$, is much smaller than the corresponding solve, for pressure p, required in the scheme resulting from a similar temporal discretization of (3.4–3.6).

The above boundary conditions are valid for only a sufficiently large domain, and with a uniform grid, could result in a large number of grid points. In order to circumvent this problem, Colonius & Taira (2008) developed a multi-domain approach to apply simple far-field boundary conditions. The domain around the immersed body is considered to be embedded in a series of domains, each twice as large as the preceding, with a uniform but a *coarser* grid having the same number of grid points; see Fig. 3.1. The circulation field on the smallest is first *coarsified* or interpolated onto the next larger mesh. The Poisson equation (3.11), with zero boundary conditions, is solved on the largest domain to obtain the stream function. This solution is then interpolated to obtain the values on the boundary of the next smaller domain, which are in turn used as boundary conditions to solve the Poisson equation on the smaller domain. The immersed body is assumed to be present only in the smallest domain, which consists of a fine mesh in the region of interest around the body. For the model problem of two dimensional flow past a flat plate, the typical size of the largest domain is around 40 chord lengths in each direction, and the number of domains is 3–5. The operators for interpolating between different levels of domains are carefully designed to preserve the total circulation. The cost of the method increases due to the multi-domain implementation, as the Poisson equation (3.11) is required to be solved at least once for each domain, however, the overall cost benefit due to the elimination of pressure and use of the fast Sine transform results in an overall speed-up by an order-of-magnitude over the previous algorithm of Taira & Colonius (2007).

3.1.1 Linearized and adjoint equations

For deriving reduced-order models useful for control design using the approximate balanced truncation method outlined in section 2.2, we first linearize equations (3.9, 3.10) about a pre-computed steady state (γ_0, q_0); computation of this steady state is discussed later in section 3.3.1. The linearized equations are the same as equations (3.9, 3.10) with the nonlinear term $\mathcal{N}(q)$ replaced by its linearization about the steady state. Thus, the linearized equations are:

$$\frac{d\gamma}{dt} + C^T E^T \tilde{f} = -\beta C^T C \gamma + C^T \mathcal{N}_L(\gamma_0)\gamma, \tag{3.16}$$

$$ECs = 0, \tag{3.17}$$

where $\mathcal{N}_L(\gamma_0)\gamma$ is the spatial discretization of

$$q_0 \times \gamma + q \times \gamma_0, \tag{3.18}$$

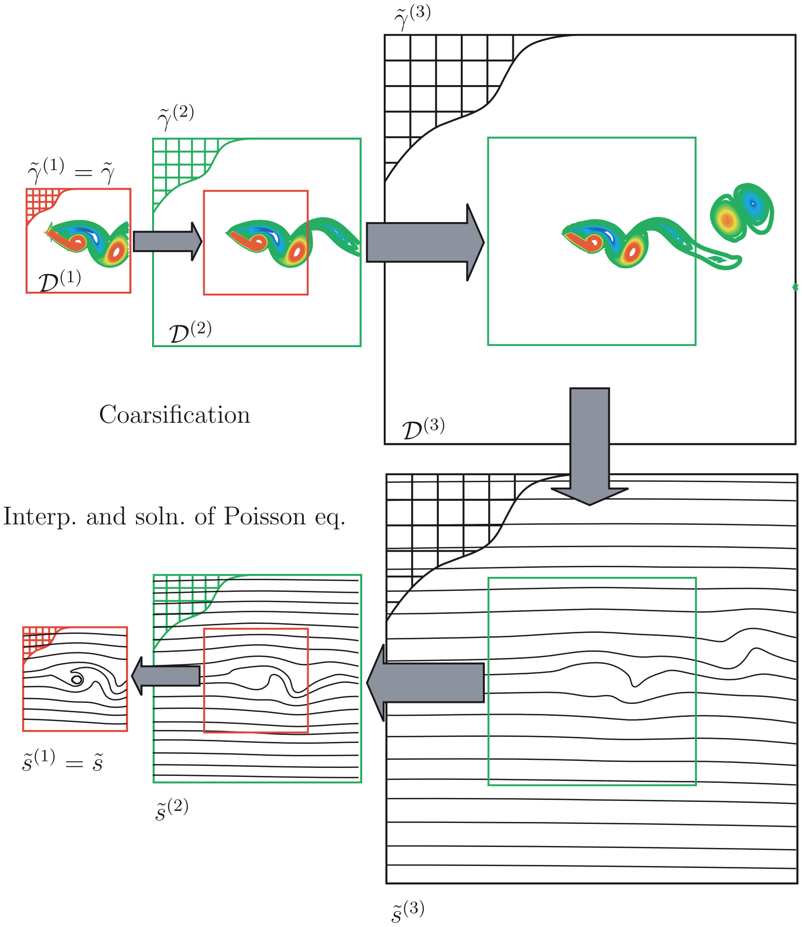

$\tilde{\gamma}^{(3)}$
$\tilde{\gamma}^{(2)}$
$\tilde{\gamma}^{(1)} = \tilde{\gamma}$
$\mathcal{D}^{(1)}$
$\mathcal{D}^{(2)}$
Coarsification
$\mathcal{D}^{(3)}$
Interp. and soln. of Poisson eq.
$\tilde{s}^{(1)} = \tilde{s}$
$\tilde{s}^{(2)}$
$\tilde{s}^{(3)}$

Figure 3.1: Mutli-domain method to solve the Poisson equation. Figure taken from Colonius & Taira (2008).

and the flux q is related to γ by (3.11). The boundary conditions for the linearized equations are $bc_\gamma = 0$ on the outer boundary of the largest computational domain.

The modeling technique of section 2.2 also requires certain adjoint simulations to approximate the observability Gramians. In order to derive the adjoint formulation of (3.9, 3.10), we define the following inner-product on the state-space:

$$\langle \gamma_1, \gamma_2 \rangle_{\mathcal{X}} = \int_\Omega \gamma_1 \, (C^T C)^{-1} \gamma_2 \, dx. \tag{3.19}$$

That is, the inner-product defined on the state-space is the standard L^2-inner product weighted with the inverse-Laplacian operator. Using (3.8, 3.11), it can be shown that the inner-product (3.19) induces the usual energy-norm; that is, $\langle \gamma, \gamma \rangle_{\mathcal{X}} = \int_\Omega q^2 \, dx$, which is the energy of the fluid integrated over the entire domain. This choice is convenient as it results in the adjoint equations which differ from the linearized equations only in the nonlinear term. A derivation is outlined in appendix B and the resulting equations are:

$$\frac{d\zeta}{dt} + C^T E^T \psi = -\beta C^T C \zeta + (C^T C)\mathcal{N}_L(\gamma_0)^T q_a, \tag{3.20}$$

$$EC\xi = 0, \tag{3.21}$$

where the variables ζ, ξ and ψ are dual to the discrete circulation γ, stream function s and body force $\tilde{f}$, respectively, and $q_a = C\xi$ is dual to the flux q. The adjoint of the linearized nonlinear term is $(C^T C)\mathcal{N}_L(\gamma_0)^T q_a$, which can be shown to be a spatial discretization of

$$\nabla \times (\gamma_0 \times q_a) - \nabla^2(q_0 \times q_a). \tag{3.22}$$

Since equation (3.20) differs from (3.16) only in the last term on the right hand side, the numerical integrator for the adjoint equations can be obtained by a small modification to the solver for the linearized equations.

The nature of the multi-domain scheme used to approximate the boundary conditions of the smallest computational domain results in a multi-domain discrete Laplacian that is not exactly self-adjoint to numerical precision. As a result, the adjoint formulation given by (3.20, 3.21) which also uses the same multi-domain approach, is not precise and results in small, rather insignificant, errors in the computation of the reduced-order models.

3.2 Model problem: flow past a flat plate

We apply the model reduction techniques developed in the previous sections to the uniform flow past a flat plate in two spatial dimensions, at a low Reynolds number, $\mathsf{Re} = 100$. We obtain reduced-order models of a system actuated by means of a localized body force near either the leading edge or the trailing edge of the flat plate; the vorticity contours of the flow field obtained on an impulsive input to the actuator are shown in Fig. 3.2. Using these reduced-order models, we develop feedback controllers that stabilize the unstable steady state at high angles of attack. We first assume full-state feedback, but use output projection described in section 2.1.4 to considerably decrease the number of outputs in order to make the model computation tractable. Later, we relax the full-state feedback assumption, and develop more practical observer-based controllers which uses a few velocity measurements in the near-wake of the flat plate (shown in Fig. 3.2) to reconstruct the entire flow.

3.2.1 Numerical parameters

The grid size used is 250 × 250, with the smallest computational domain given by $[-2, 3] \times [-2.5, 2.5]$, where lengths are non-dimensionalized by the chord of the

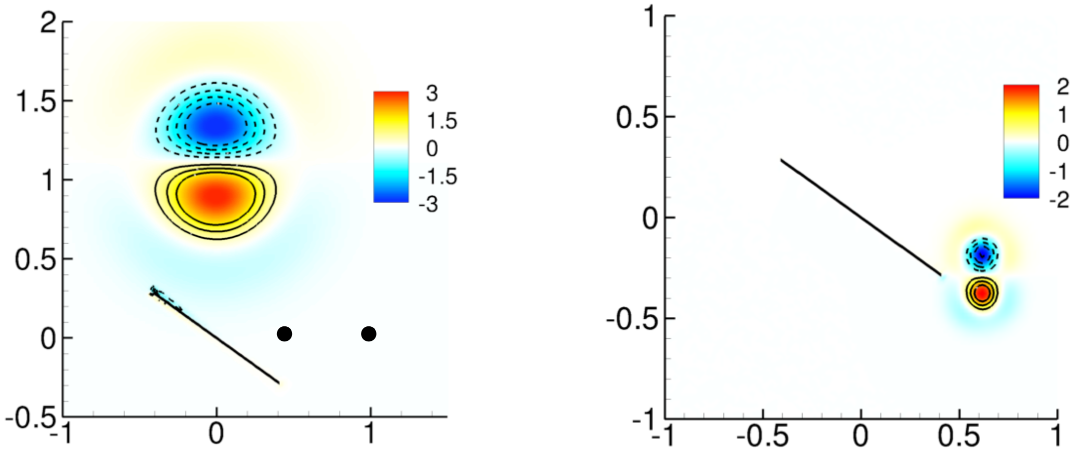

Figure 3.2: Actuator modeled as a localized body force near the leading (left) and trailing (right) edge of the flat plate, with the angle of attack fixed at $\alpha = 35°$. Vorticity contours are plotted, using both color and line plots, with negative contours shown by dashed lines. The velocity-sensor locations are marked by solid circles.

flat plate, with its center located at the origin. We use 5 domains in the multiple-grid scheme, resulting in an effective computational domain 2^4 times larger the size of the smallest domain; thus the largest domain is given by $[-32, 48] \times [-40, 40]$. The timestep used for all simulations is $\Delta t = 0.01$.

3.2.2 Input and output

The actuation is modeled as a localized body force near the flat plate; two different locations, near the leading and trailing edges of the flat plate, are considered. The control is implemented in the numerical solver by simply adding a term of the form Bu, as appears in equation (2.65), where B is a velocity field that is divergence-free and satisfies the no-slip boundary conditions at the surface of the flat plate:

$$\gamma_{k+1} = \Phi(\gamma_k) + Bu_k, \tag{3.23}$$

where $\Phi(\gamma_k)$ is a compact representation of the time-stepper obtained from a temporal discretization of (3.9, 3.10). The flow-field obtained from an impulsive input ($u_k = \delta_k$) consists of two counter-rotating vortices, where the circulation of each vortex given by

$$B^i_\gamma(r) = \pm c(1 - ar^2)e^{-ar^2}, \quad i = 1, 2 \tag{3.24}$$

$$\text{where,} \qquad r^2 = (x - x_{0,i})^2 + (y - y_{0,i})^2; \tag{3.25}$$

the constants a and c determine the radius and strength of the vortices, while $(x_{0,i}, y_{0,i})$ determine the location of the centers of these vortices. The velocity fields corresponding to the functions B^i_γ do not satisfy the no-slip boundary conditions at the plate surface; a projection step is used to enforce these conditions and the resulting fields are used to model actuation. The two different choices of actuation considered here are shown in Fig. 3.2.

In previous research, Taira & Colonius (2009*a*) considered actuators modeled as body forces smeared over a few grid points in studying the effect of open loop constant forcing on three-dimensional flows past a low aspect ratio flat plate, while Williams *et al.* (2008) performed experiments on semi-circular planforms using periodic blowing through slots on the leading edge. The actuation above is a simplistic model of blowing and suction, although our aim here is not to have an accurate representation of blowing or suction, but rather to demonstrate the effectiveness of the algorithms presented in chapter 2 by developing simple controllers. Several other actuators were also considered by varying the constants a, c in (3.24), and two that resulted in successful controllers are reported here.

The energy input from the actuation, in studies using open-loop control by steady or periodic forcing, is often quantified in terms of the momentum coefficient C_μ (Greenblatt & Wygnanski, 2000; Taira & Colonius, 2009*a*) which is defined as:

$$C_\mu = \frac{\rho U_{\mathrm{act}}^2 \sigma_{\mathrm{act}}}{\frac{1}{2}\rho U_\infty^2 c} \tag{3.26}$$

where U_{act} is the constant actuator velocity in case of steady forcing, σ_{act} is the actuator width, and c is the flat plate chord length. With feedback control, the input u is a function of time and so is U_{act}, and thus the momentum coefficient is time-dependent. However, for the sake of quantifying the control input, we assume that the input u has unit amplitude and is a constant. Later, we will see that the maximum amplitude of u is $O(1)$ and this assumption holds. For leading edge actuation, the maximum velocity of actuation is $U_{\mathrm{act}}/U_\infty = 0.003$, while the actuation width is $\sigma_{\mathrm{act}}/c = 1$, which gives $C_\mu \approx 0.08\%$. For trailing edge actuation, the maximum velocity of actuation is $U_{\mathrm{act}}/U_\infty = 0.07$, while the actuation width is $\sigma_{\mathrm{act}}/c = 0.3$, which gives $C_\mu \approx 0.15\%$. Both of these values are in the standard range $C_\mu = 0.01\%$ to 10% used in studies using steady actuation (Greenblatt & Wygnanski, 2000; Taira & Colonius, 2009*a*).

We also consider two different outputs of the system, and they are:

1. The velocity field over the entire fluid domain, which is used for developing full-state feedback controllers. As discussed in section 2.1.4, for large dimensional outputs, the model reduction procedure using approximate balanced truncation becomes intractable as the number of adjoint simulations needed is the same as the number of outputs. Hence, output projection is used and the observables are considered to be the velocity field projected onto (a) unstable eigenmodes and (b) leading POD modes of the stable subspace dynamics (impulse-response).

2. Velocity measurements at two near-wake sensor locations, shown in Fig. 3.2, which are used to develop observer-based feedback controllers.

The control goal is to stabilize unstable steady states using the above actuators and sensors, for which we first develop reduced-order models using the methods developed in sections 2.2.2 and 2.3.

3.3 Steady state analysis

The dimension reduction techniques described in chapter 2 start with linear state-space equations of the form (2.1, 2.2). In order to obtain equations in that form, we linearize the Navier-Stokes equations about steady-state solutions. Further, the approximate balanced truncation method of section 2.2.2 requires the global unstable eigenvectors of the linearized flow. This section deals with the computations of steady states of our model problem, and their linear stability analysis. We use a "time-stepper based" approach reviewed in Tuckerman & Barkley (1999), in which the original numerical solver is treated as a black box and efficient computational wrappers are developed around it for performing steady-state analyses.

3.3.1 Continuation using Newton-GMRES

The computational task of computing steady states of the governing equations is fundamentally different from the task of developing solvers for marching the solutions forward in time. The first consists of solving boundary value problems and, after discretization, leads to coupled nonlinear algebraic equations, usually solved using iterative techniques. The second task consists of initial value problems and leads to time-stepping schemes; the immersed boundary method of section 3.1 is an example. For fluid mechanical problems, the first task often becomes unwieldy due to large dimensional discretizations, although it has been applied to various problems. For instance, Sanchez *et al.* (2002) developed efficient continuation methods for cylindrical geometries and applied it to a flow in a driven cylinder; Cliffe *et al.* (2000) developed a detailed convergence theory for a finite element method and performed a bifurcation study of the Taylor-Couette flow; de Almeida & Derby (2000) computed steady states of the flow over a lid-driven cavity. Although there has been considerable research effort in this area, a much greater impetus has been towards the second task of developing numerical time-steppers, as it offers insights into the dynamics, and allows direct comparison with experiments; the number of solvers developed is so vast that a review is not even attempted here. The main idea of Tuckerman & Barkley (1999) is to convert these time-steppers into steady-state solvers, thus performing the first task without having to solve the huge set of nonlinear equations. This technique was first developed by Chowdhury

& Tuckerman (1995) for the spherical Couette flow, and has been applied for identifying three-dimensional instabilities of the flow past a cylinder by Barkley & Henderson (1996) and in the flow over a backward-facing step by Barkley *et al.* (2002).

An alternate method, called selective frequency damping, was developed by Åkervik *et al.* (2006), adapting tools from control theory for computing steady states. In this method, a control term proportional to the difference between the actual and the (temporally) low-pass filtered state, is used in an attempt to stabilize unstable steady states. The method was used to compute steady states of flow over a cavity by Åkervik *et al.* (2006), a three-dimensional jet in cross-flow by Bagheri *et al.* (2009*b*) and of the flow over a low aspect-ratio flat plate by Rowley *et al.* (2008). The method has good performance when the instability arises due to high frequency components, but the choice of filtering parameters is ad-hoc; in the presence of low-frequency components, it becomes difficult to obtain the parameters that stabilize the steady state.

Here, we adopt the approach of developing computational wrappers around the immersed boundary solver to compute steady states. If the numerical timestepper advances a circulation field γ^k at a timestep k to a circulation field $\gamma^{k+T} \equiv \Phi_T(\gamma^k)$ after T timesteps, a steady state is given by a field γ_0 that satisfies

$$g(\gamma_0) = \gamma_0 - \Phi_T(\gamma_0) = 0. \tag{3.27}$$

The steady states are thus given by zeros of $g(\gamma_0)$, which could, in principle, be solved for using Newton's method. However, the standard Newton's method involves computing and inverting Jacobian matrices at each iteration, which is computationally infeasible due to the large dimension of fluid systems. Instead of computing the Jacobian, we use a Krylov-space based iterative solver called Generalized Minimal Residual Method (GMRES) developed by Saad & Schultz (1986) to compute the Newton update (see Kelley (1995) and Trefethen & Bau (1997) for a description of the method). This method requires computation of only Jacobian-vector products $Dg(\gamma) \cdot v$, which can be approximated using finite differences as

$$Dg(\gamma) \cdot v = \frac{g(\gamma + \epsilon v) - g(\gamma)}{\epsilon}, \qquad \text{for} \quad 0 < \epsilon \ll 1. \tag{3.28}$$

So, the Jacobian-vector products can also be computed by invoking the appropriately-initialized timestepper. A nice feature of GMRES is relatively fast convergence to the steady state when the eigenvalues of the Jacobian $Dg(\gamma_0)$ occur in clusters; see Kelley (1995) and Kelley *et al.* (2004) for details. For systems with multiple time-scales, such as Navier-Stokes, most of the eigenvalues of the continuous Jacobian lie in the far-left-half of the complex plane. Thus, the corresponding eigenvalues of the discrete Jacobian $D\Phi_T$, for a sufficiently large value of T, cluster near the origin; this is schematically shown in Fig. 3.3; the larger the value of T, the tighter is the clustering.

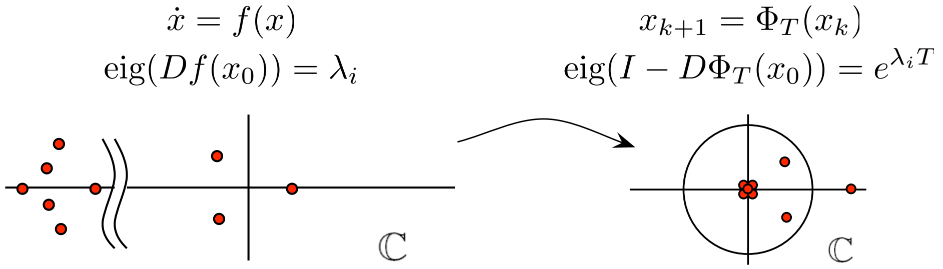
$\dot{x} = f(x)$
$\mathrm{eig}(Df(x_0)) = \lambda_i$
$x_{k+1} = \Phi_T(x_k)$
$\mathrm{eig}(I - D\Phi_T(x_0)) = e^{\lambda_i T}$
$\mathbb{C}$
$\mathbb{C}$

Figure 3.3: A schematic showing the clustering of the eigenvalues (red circles) of the linearization of the discrete time-stepper.

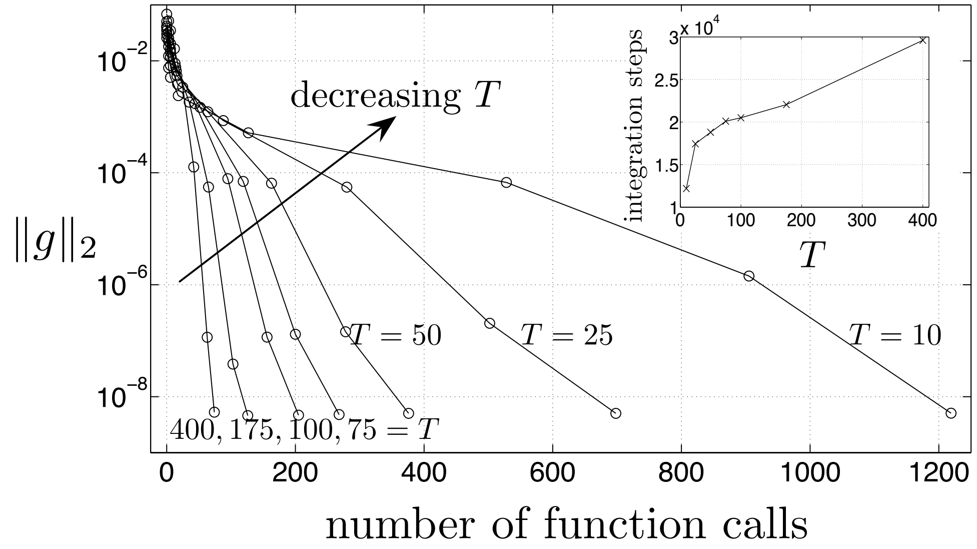

Figure 3.4: Convergence study of Newton-GMRES for different values of the paramter T.

We now study the effect of varying T on the convergence of Newton-GMRES; such a study was performed in much greater detail for a reaction-diffusion equation by Kelley *et al.* (2004). The angle of attack is fixed at $\alpha = 35°$ and the initial guess for the Newton solve is the steady state computed for $\alpha = 36°$. The value of T is varied from 10 to 400 time-steps, and in each case, 7 Newton iterations were required for convergence; the stopping criterion used was the residual to reach a level $\|g\|_2 = 10^{-8}$. For each Newton iteration, the update step is computed iteratively using GMRES. In Fig. 3.4, the reduction in the residual is plotted against the cumulative number of function calls during each iteration. We see that the total number of function calls decreases with increasing T, which can be justified by greater clustering of the eigenvalues. However, since the number of iterations of the numerical solver increases with T, the total cost need not decrease with T. In this case, the total number of integration time-steps is in fact the least for $T = 10$; see the inset in Fig. 3.4.

The Newton-GMRES method described above is used to compute the branch of steady states for the angles of attack $0 < \alpha < 90°$; the parameter T in (3.27) is fixed to 50 timesteps. The lift and drag coefficients, C_L and C_D, and their ratio C_L/C_D with changing α are plotted in Fig. 3.5. As with flow past bluff bodies with increasing Reynolds number (for example, see Provansal *et al.* (1987)), the flow undergoes a Hopf bifurcation from a steady flow to periodic vortex shedding as the angle of attack α is increased beyond a critical value α_c, which in our computations is $\alpha_c \approx 27°$. Also plotted in the figure are the maximum, minimum, and mean values of the forces during shedding for $\alpha > \alpha_c$. We see that the (unstable) steady state values of the lift coefficient are smaller than the minimum for the periodic shedding until $\alpha \approx 75°$, after which they are slightly higher, but still smaller than the mean lift for the periodic shedding. The (unstable) steady state drag is much lower than the minimum value for periodic shedding. The ratio C_L/C_D of the (unstable) steady state is close to the mean value for shedding. Thus, if the large fluctuations in the forces are undesirable at high angles of attack, it would be useful to stabilize the unstable state. The steady state at $\alpha = 35°$ is shown in Fig. 3.6(a), and a time history of the lift coefficient C_L with this steady state as an initial condition is shown in Fig. 3.6(b). Since the steady state is unstable, numerical perturbations excite the instability, and the flow eventually transitions to periodic vortex shedding.

3.3.2 Linear stability analysis

For the linear stability analysis about the steady state γ_0, we need to solve the eigenvalue problem

$$\Phi_T(\gamma_0)v = v\lambda \tag{3.29}$$

where λ and v are the eigenvalue and eigenvector of the operator $\Phi_T(\gamma_0)$, which we now think of as the time-stepper obtained from the temporal discretization of either the linearized equations (3.16, 3.17) or the adjoint equations (3.20, 3.21). In order to solve (3.29), we use another Krylov technique called the Arnoldi iteration developed by Arnoldi (1951); see also Trefethen & Bau (1997). A variant of this method called the implicitly restarted Arnoldi method has been implemented by Lehoucq *et al.* (1998) and is freely available in the form of a Fortran-77 library called ARPACK. This library can be used to compute a small number of eigenvalues (and eigenvectors) with user-specified properties such as the largest or smallest magnitude, largest or smallest real part, etc. to a desired accuracy. We use this library to compute the leading eigenvectors of the linearized and adjoint equations, that is, those corresponding to the eigenvalues with the largest magnitude.

The eigenvalues μ of the continuous operator are related to the eigenvalues λ of the discrete operator by $\mu = \log\lambda/(T\Delta t)$, where we fix $T = 30$ timesteps. We computed two eigenvalues with the largest magnitude for the range of angle of attack $20 \leq \alpha \leq 90°$, and found that they form a complex pair, implying an

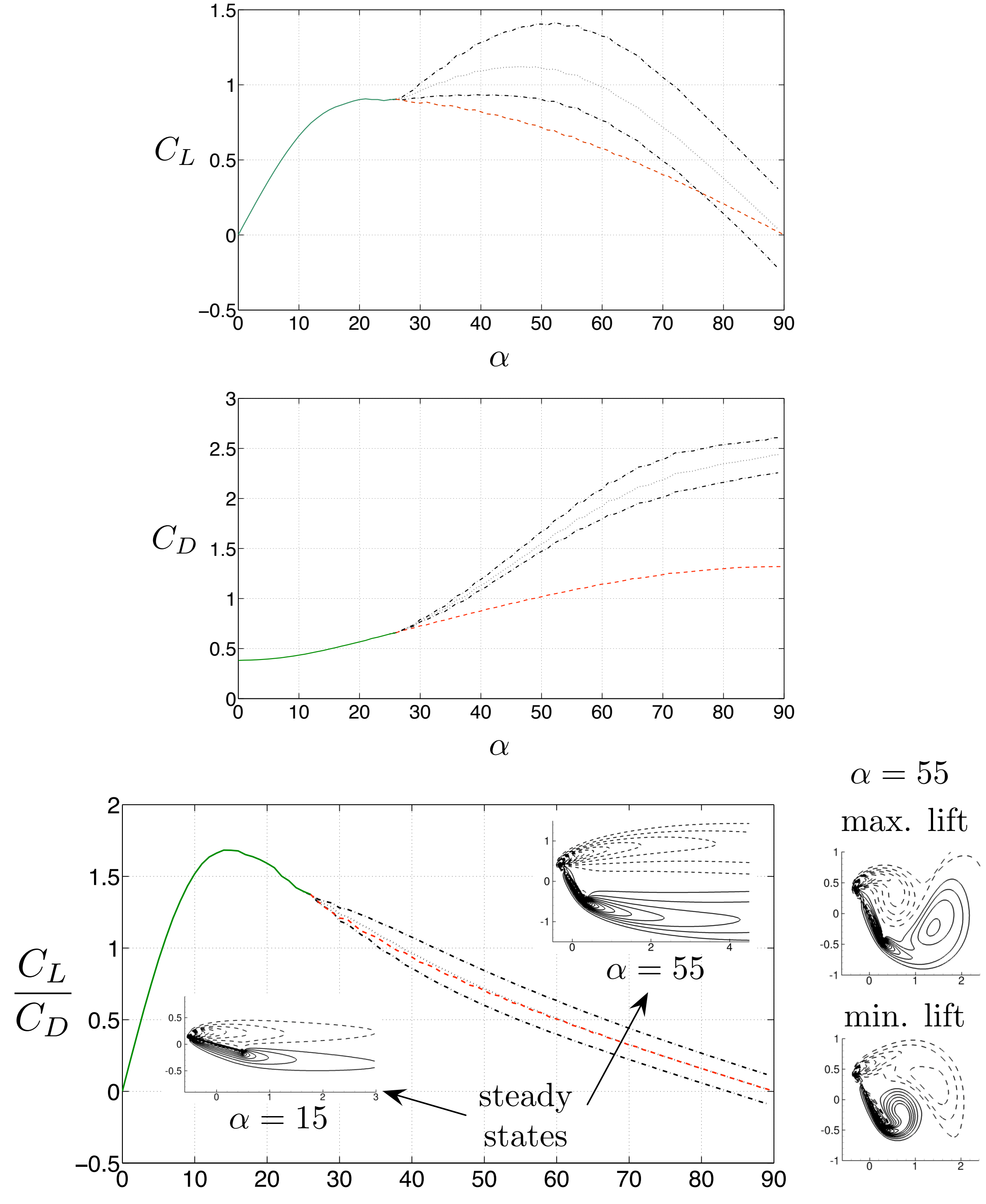

Figure 3.5: Forces on a flat plate at a fixed angle of attack α and at $\mathsf{Re} = 100$, showing a transition from a stable equilibrium to periodic vortex shedding at $\alpha \approx 26°$. Shown are the force coefficients corresponding to the stable (——) and unstable (- - - -) steady states, and the maximum and minimum (—·—), and the mean (·······) values during periodic vortex shedding. Also shown are the vorticity contours (negative values in dashed lines) of steady states at $\alpha = 15°, 55°$ and the flow fields corresponding to the maximum and minimum force coefficients at $\alpha = 55°$.

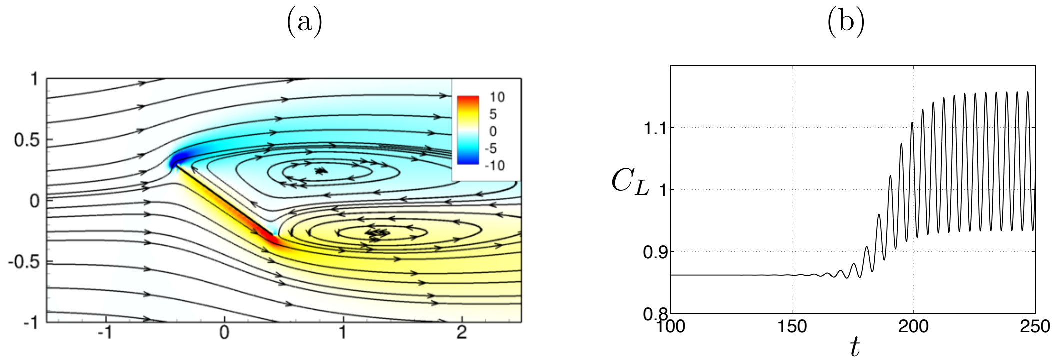

Figure 3.6: (a) Streamlines of the unstable steady state at $\alpha = 35$. (b) C_L vs. time, with the steady state as an initial condition.

oscillating eigenmode. The real and imaginary parts of these eigenvalues, which correspond to the growth rate and frequency of the instability, are plotted in Fig. 3.7. The real part of the eigenvalue becomes positive (or the eigenvalues cross the imaginary axis into the right-half complex plane with a non-zero speed) at $\alpha_c \approx 27°$, confirming Hopf bifurcation. For the post-bifurcation values of α, we also plot the frequency of vortex shedding, which depart considerably from the frequency of the linear instability growth, consistent with the finding of Barkley (2006) for the flow past a cylinder. The real and imaginary parts of the right and left (linear and adjoint) unstable eigenvectors of the flow linearized about the steady state at $\alpha = 35°$ are plotted in Fig. 3.8. These modes are qualitatively similar to the structures during periodic vortex shedding, but have different spatial wavelengths, as reported in earlier studies by Noack *et al.* (2003) and Barkley (2006).

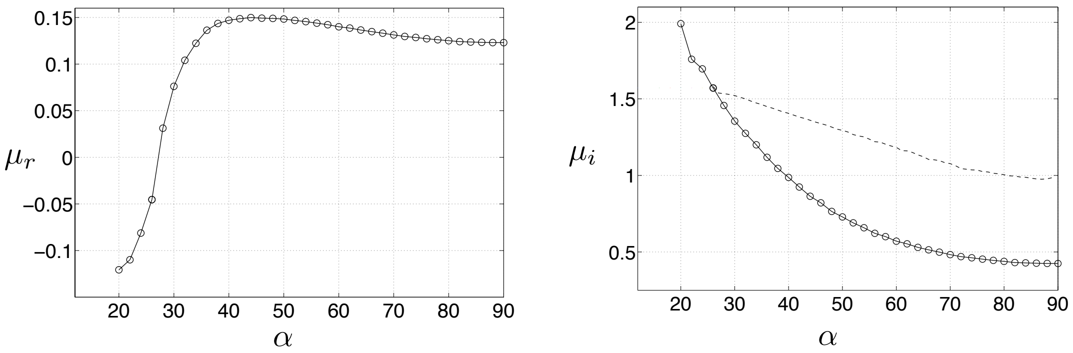

Figure 3.7: The real (μ_r) and imaginary (μ_i) part of the eigenvalues, representing the growth rate and frequency of the corresponding eigenmodes, of the flow linearized about the steady states in the range $20 \leq \alpha \leq 90°$. Also shown is the frequency of the periodic vortex shedding for $\alpha \geq 27°$ (−−−−).

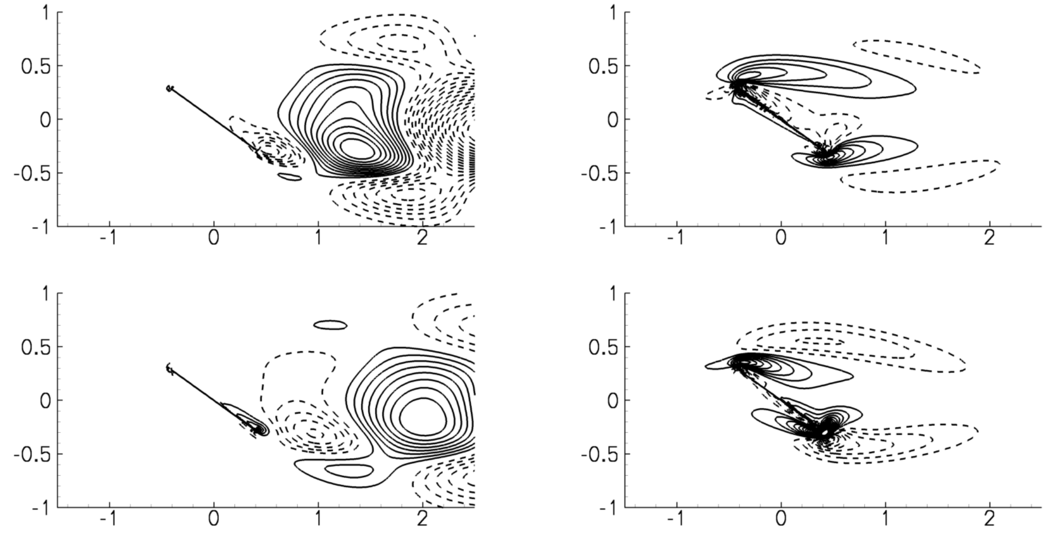

Figure 3.8: Real (top) and imaginary (bottom) parts of the unstable eigenvectors of the linearized (left) and the adjoint (right) equations, for $\alpha = 35°$. Vorticity contours are plotted (negative contours are dashed).

3.4 Reduced-order models

In this section, we describe the process involved in deriving the reduced-order models of the input-output response of the linearized Navier-Stokes equations (3.16, 3.17), which upon adding the actuation inputs and sensor outputs, are in the form of the state-space equations (2.1, 2.2). The equations (3.16, 3.17) are considered to be linearized about the unstable steady state at $\alpha = 35°$, and the models developed here will be used in the later sections to develop controllers that stabilize this steady state. The model reduction procedure is outlined for the leading edge actuation, plotted on the left in Fig. 3.2, and is similar for the trailing edge actuation. The models are derived using the approximate balanced truncation procedure outlined in section 2.2.2. The output of the system is considered to be the entire velocity field. Since this would result in large number of adjoint simulations, we use output projection described in section 2.1.4, and approximate the output by its projection onto (a) the unstable eigenspace, and (b) the span of the leading POD modes of the impulse response restricted to the stable subspace.

The first step in computing the reduced-order models is to project the flow field B onto the stable subspace of (3.16, 3.17) using the projection operator $\mathbb{P}_s$ defined in equation (2.44); the unstable eigenvectors computed in section 3.3.2 are used to define $\mathbb{P}_s$ numerically. The vorticity contours of the corresponding flow field $\mathbb{P}_s B$ are plotted in Fig. 3.9a. The next step is to compute the impulse response of (2.45), which is rewritten here:

$$\dot{x_s} = \mathbb{P}_s A x_s + \mathbb{P}_s B u; \tag{3.30}$$

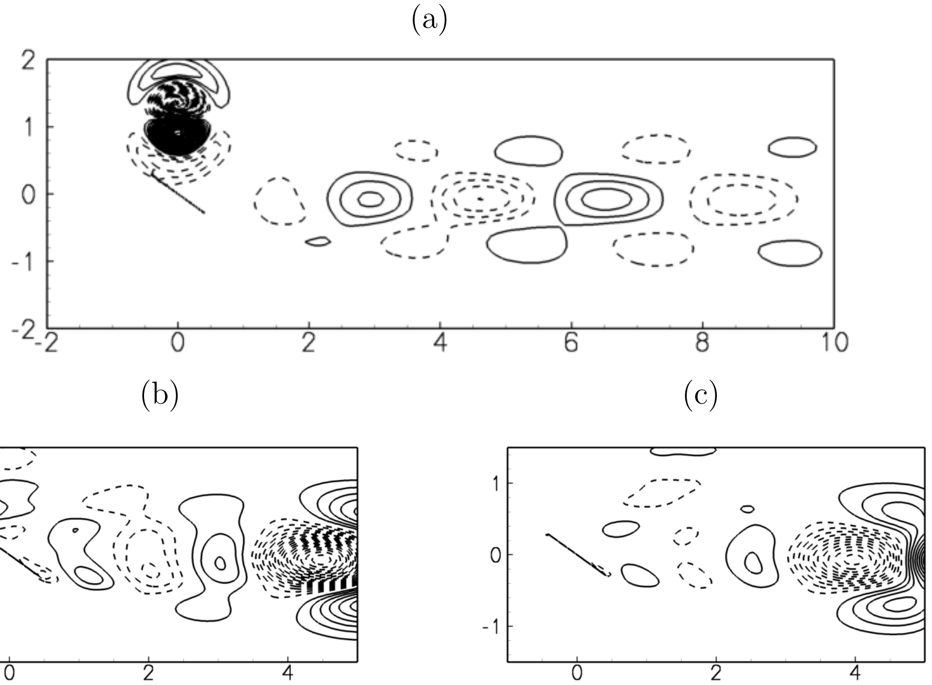

Figure 3.9: Vorticity contours of (a) the flow field shown in Fig. 3.2, projected onto the stable subspace, and (b,c) the first- and fifth-most energetic POD modes of the impulse response to the leading edge actuation, restricted to the stable subspace.

that is, at each timestep of integration, we project the state x_s onto the stable subspace of A using the operator $\mathbb{P}_s$. Since the stable subspace is an invariant subspace for the linearized dynamics (3.16, 3.17), theoretically, it should be sufficient to project only the initial condition, and the resulting dynamics should be constrained to the stable subspace. However, due to the (small) numerical inaccuracy of the projection $\mathbb{P}_s$ (which is a result of the numerical inaccuracy of the unstable eigenspaces Φ_u and Ψ_u), the resulting dynamics might not be strictly restricted to the stable subspace and indeed, in the long term, grows without bound in the unstable direction. Thus, the state is projected at each timestep to ensure that it remains constrained to the stable subspace. Next, we compute the POD modes θ_s^i of the impulse response of (3.30), and consider the output of (3.30) to be the state x_s projected onto a certain number of these POD modes. Here, 200 snapshots spaced every 50 timesteps were used to compute the POD modes. The leading 4, 10 and 20 POD modes contain 84.47%, 98.98% and 99.89% of the energy respectively and, as it has been observed in previous studies (Deane *et al.*, 1991; Ilak & Rowley, 2008), these modes come in pairs in terms of their energy content, a characteristic of traveling structures; the leading first and third POD modes are shown in Fig. 3.9.

The next step is to compute the adjoint snapshots, with the POD modes of the impulse response (projected onto the stable subspace of the adjoint) as the initial

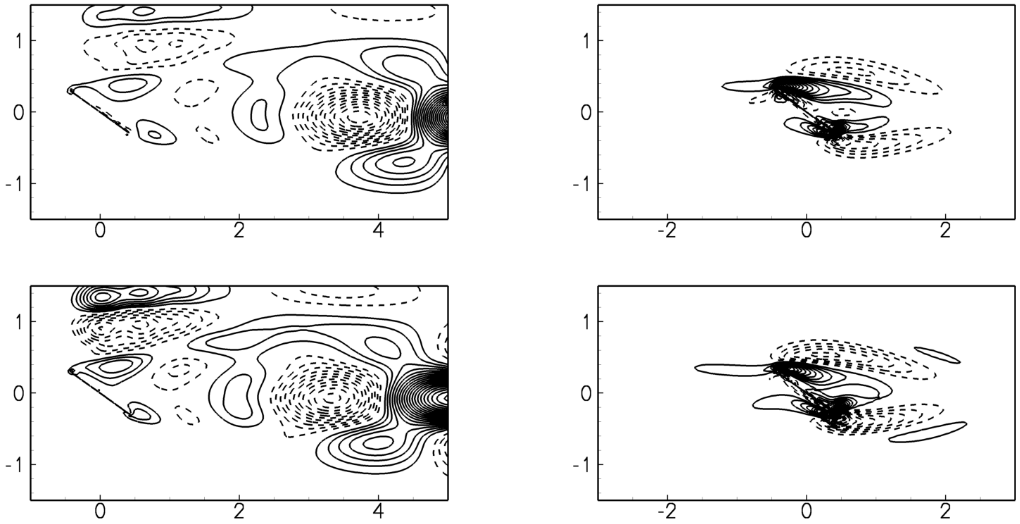

Figure 3.10: Vorticity contours of the leading (in the order of Hankel singular values of the stable subspace dynamics) first and third balancing (left) and adjoint (right) modes. The input is given by leading edge actuation and the output is the entire velocity field, projected onto 10 POD modes.

conditions. As in the case of the linearized impulse response, these simulations are also restricted to the stable subspace. We compute the impulse response of (2.47), which is rewritten here:

$$\dot{z}_s = \mathbb{P}_s^* A^* + \mathbb{P}_s^* C^* v. \tag{3.31}$$

The snapshots of the impulse responses of systems (3.30) and (3.31) are stacked as columns of X and Z, and using the expressions (2.33) and (2.34), we obtain the balancing modes ϕ_s^i and the adjoint modes ψ_s^i. We used 200 snapshots of the linearized simulation and 200 snapshots of each adjoint simulation, with the spacing between snapshots fixed to 50 timesteps, to compute the balancing transformation. These number of snapshots and the spacing were sufficient to accurately compute the modes; further reduction in the spacing did not significantly change the singular values from the SVD computation (2.33). We considered the outputs to be a projection onto 4, 10 and 20 POD modes (corresponding to 4, 10 and 20 mode *output-projections*, as introduced in section 2.1.4). Using these modes, we use the expressions in equation (2.57, 2.62) to obtain the matrices $\widetilde{A}_s, \widetilde{B}_s, \widehat{C}_s$ defining the reduced-order model of the stable-subspace dynamics. The vorticity contours of the balancing and the adjoint modes, for a 10-mode output projected system, are plotted in Fig. 3.10. The adjoint modes provide a direction for projecting the linearized equations onto the subspace spanned by the balancing modes. These modes are quite different from the POD and the balancing modes; thus, the resulting models are also quite different from those obtained using the standard POD-Galerkin technique wherein an orthogonal projection is used. Since the models obtained using balanced truncation are known to perform better than the POD-Galerkin models,

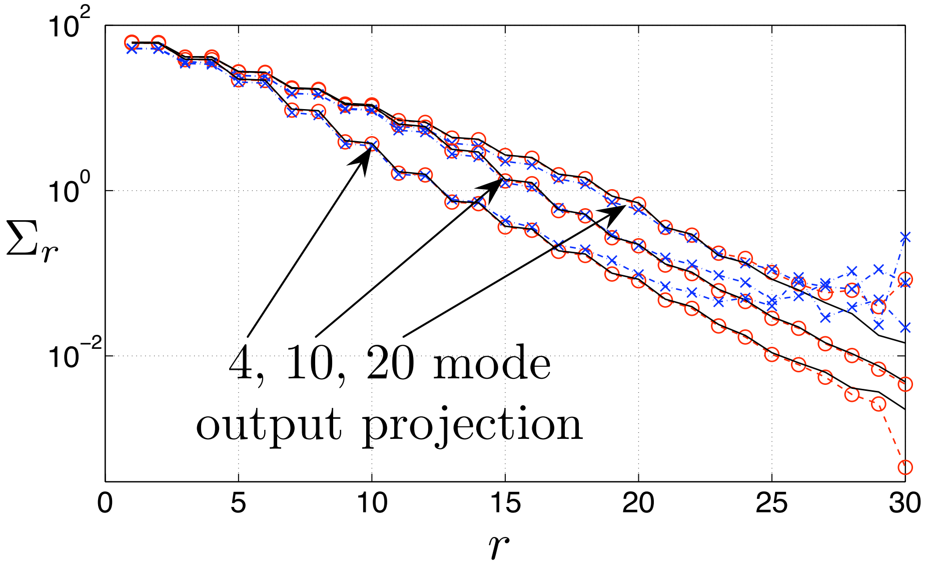

Figure 3.11: Reduced-order models obtained using approximate balanced truncation. The empirical Hankel singular values (——) and the diagonal elements of the controllability (- - - -, ○) and observability (— - —, ×) Gramians of a 25-mode model with leading edge actuation and the full-state output approximated using a 4, 10, and 20-mode output projection, for the unstable steady state at $\alpha = 35$.

as reported in Ilak & Rowley (2008), the better performance could be attributed to a better choice of projection using the adjoint modes.

Since the reduced-order models of the stable-subspace dynamics are approximately balanced, the controllability and observability Gramians of the a_s-dynamics of (2.57, 2.58), given by expressions (2.16, 2.17), are approximately equal and diagonal. Further, their diagonal values are approximately the same as the Hankel singular values (HSVs) σ_i obtained by the SVD (2.33). The diagonal values of the Gramians and the singular values for different output projections are plotted in Fig. 3.11 for a 30-state reduced-order model. With increasing order of output projection, the HSVs converge to the case with full-state output, and the number of converged HSVs is roughly equal to the order of output projection, as was observed by Ilak & Rowley (2008). We see that the diagonal elements of both the Gramians are very close to the HSVs for the first 20 modes. For higher modes, the observability Gramians are inaccurate, which is due to a small inaccuracy of the adjoint formulation mentioned in section 3.1.1. For controller design, we use models of order ≤ 20, for which these Gramians are sufficiently accurate.

In order to test the accuracy of the reduced-order models, we compare the impulse responses of system (3.30) (that is, restricted to the stable subspace) with that of the model (2.57), restricting $a_u = 0$. In particular, we compare the outputs of the two systems, which are the projection onto the POD modes; a representative case in Fig. 3.13 shows the results of 4, 10 and 20 mode models of a system approximated

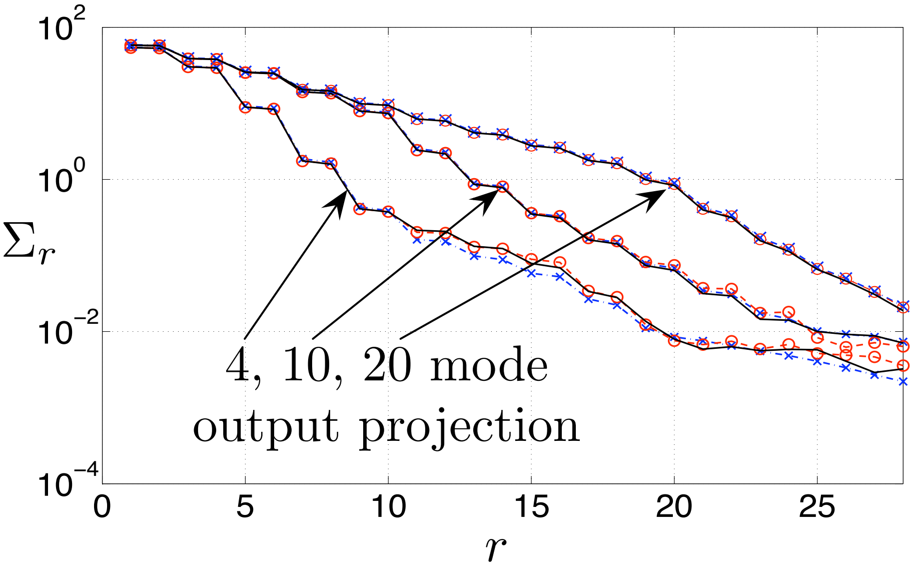

Figure 3.12: The plots represent the same information shown in Fig. 3.11 for reduced-order models obtained using ERA.

using a 20-mode output projection (the outputs are projection onto the leading 10 POD modes). The first output, which is a projection onto the first POD mode, is well captured by all the models until $t \approx 60$, while the 20-mode model performs well for all time. Also shown is the eleventh output, which is well captured only by the 20-mode model. As we will see later, it is important to capture the higher-order outputs for design of observers.

3.4.1 Comparison with ERA

As described in section 2.3, the eigensystem realization algorithm (ERA) theoretically results in the same reduced-order models as approximate balanced truncation. Here, we use ERA to compute models of the stable subspace dynamics and compare them with those obtained in the previous section using balanced POD.

In order to compute models using ERA, the first step is to collect the Markov parameters given by (2.69, 2.80), which are simply the outputs of the impulse response of (2.45, 2.46). Here, the output is the entire velocity field approximated as a projection onto m-POD modes of this impulse response (using output projection). Thus, m inner products are required to compute the Markov parameters for each snapshot. For direct comparison with models obtained using approximate balanced truncation, 400 pairs of Markov parameters spaced every 50 timesteps were collected to compute the Hankel matrices H and H_1, given by (2.71, 2.78). Thus, for an output projection of order m, the number of inner products required is $m_c + m_o = 400m$ (see section 2.3). In comparison, in approximate balanced truncation the

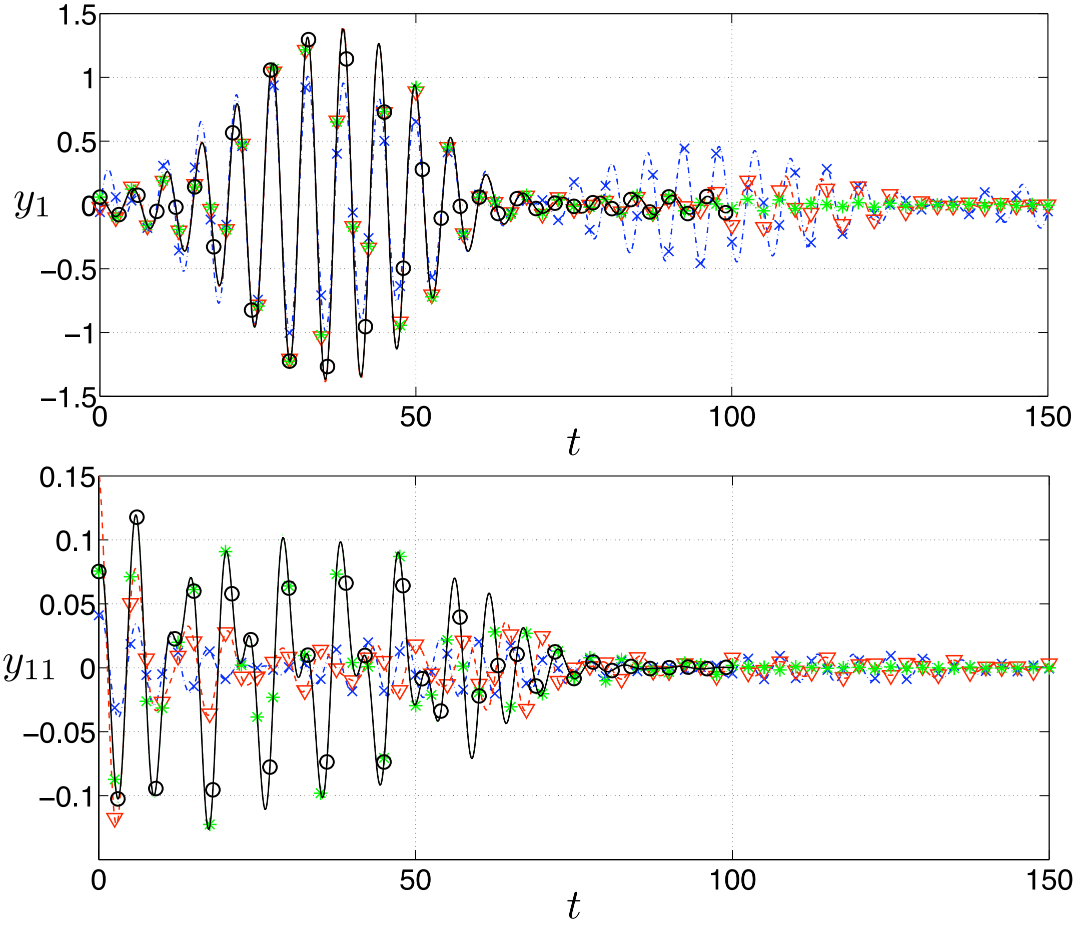

Figure 3.13: Outputs (projection of the flow field onto POD modes) from a reduced-order model obtained using a 20-mode output projection. Actuation is near the leading edge. The first (top figure) and eleventh (bottom figure) outputs of the DNS (———, ∘) are compared with predictions of models with 4 (—·—, ×), 10 (– – – –, ▽), and 20 (·······, ∗) modes.

Hankel matrix H is obtained by computing the inner products of forward and adjoint snapshots as given in 2.83. Thus, the number of inner products required is $200 \times 200m$, which is 50 times more than that to compute H and H_1 in total for ERA. The number of inner-products required using the two methods for different orders of output projection is given in table 3.1.

The diagonal values of the controllability and observability Gramians, and the empirical Hankel singular values of the reduced-order models obtained using ERA are plotted in Fig. 3.12 and can be compared directly with those obtained using balanced POD, shown in Fig. 3.11. The models obtained using ERA are more accurate in the sense that the three sets of curves are almost indistinguishable, for all orders of output-projection. However, for balanced POD, the diagonal values of the observability Gramians are accurate only for certain leading modes, the number of which depends on and increases with the order of output projection. This inaccuracy can be attributed to a slight inaccuracy in the adjoint formulation, which in turn results from an approximation in the multi-domain approach of the immersed boundary method of Colonius & Taira (2008). Thus, ERA is advantageous as it does not need any adjoint simulations and results in more balanced Gramians. The advantage of balanced truncation is that it provides the adjoint modes, which can be used to compute the reduced states, which in turn can be used for full-state feedback control. More importantly, these modes can provide other information such as the identifying regions of the flow that are most sensitive to actuation.

Order of output projection	No. of inner-products using approx. bal. trunc.	No. of inner-products using ERA	Speed-up factor
4	1.6×10^5	2.0×10^3	80
10	4.0×10^5	4.4×10^3	91
20	8.0×10^5	8.4×10^3	95

Table 3.1: Comparison of the computational costs for obtaining reduced-order models using approximate balanced truncation and ERA. The second and third column compare the number of inner-products required in the two methods, using 200 snapshots from each linearized and adjoint impulse response simulation. The last column is the total speed-up factor achieved using ERA.

3.5 Full-state feedback control

The reduced-order models derived in section 3.4 can now be used along with standard linear control techniques to obtain stabilizing controllers. We again consider leading edge actuation and the output is considered to be the entire velocity field.

We use a Linear Quadratic Regulator (LQR) $u = Ka$ so that the eigenvalues of $(\widetilde{A} + \widetilde{B}K)$ (where the matrices were defined in (2.57)) are in the left-half of the complex plane, and the gain K is chosen to minimize the cost function

$$J[a, u] = \int_0^\infty (a^* Q a + u^* R u)\, dt, \tag{3.32}$$

where Q and R are positive weights chosen as follows. We choose Q such that the first term in the integrand of (3.32) represents the energy (in perturbations from the steady state), that is, we use $Q = \widetilde{C}^* \widetilde{C}$, with $\widetilde{C}$ defined in (2.58) and $C = I$. The weight R is chosen to be a multiple of the identity cI, and typically c is chosen to be a large number $\sim O(10^{4-7})$, to avoid excessively aggressive controllers. The control implementation steps are sketched in Fig. 3.14; first compute the reduced-order state a, using the expression (2.64), then the control input is given by $u = Ka$. Here, we derive the gain K based on a 12-mode reduced-order model (with 2 unstable and 10 stable modes), using $R = 10^5$, and include the same in the original linearized and nonlinear simulations. The output is approximated using a 4-mode output projection. The difference between the linear and nonlinear simulations is that, in the latter, the steady state field x_0 is subtracted from the state x, before projecting onto the modes to compute the reduced-order state a.

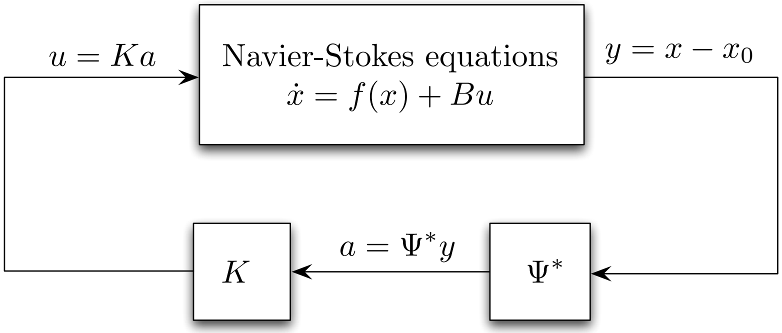

Figure 3.14: Schematic of the implementation of full-state feedback control in the nonlinear simulations. The entire velocity is first projected onto the unstable eigenvectors and the stable subspace POD modes to compute the reduced-order state a. The state is then multiplied by the gain K, computed based on the reduced-order model using LQR, to obtain the control input u.

Fig. 3.15 compares the model predictions with the projection of data from the simulations of the linearized system (3.16, 3.17), with a control input. The initial condition used is the flow field obtained from an impulsive input to the actuator. Both the states shown in the figure eventually decay to zero, which implies that the perturbations decay to zero, thus stabilizing the unstable steady state. More importantly, the model predicts the outputs accurately for the time horizon shown in the plots.

We now use the same controller in the full nonlinear simulations and test the performance of the model for various perturbations of the steady state. A plot of the lift coefficient C_L vs. time t, with the control turned on at different times of the base simulation, is shown in Fig. 3.16. The initial condition for the base case (no control) is the unstable steady state; eventually, small numerical errors excite the unstable modes and the flow transitions to periodic vortex shedding. In separate simulations, control is turned on at times $t = 170, 180, 210$ corresponding to the base case. As the figure shows, the control is effective and is able to stabilize the steady state in each case, even when the flow exhibits strong vortex shedding. We remark that the latter two of these perturbations are large enough to be outside the range of validity of the linearized system, but the control is still effective, implying a large basin of attraction of the stabilized steady state. We also compare the output of the reduced-order model with the outputs of the nonlinear simulation; the plots are shown in Fig. 3.17. The models perform well for the initial transients, but for longer times fail to capture the actual dynamics. This is not surprising as these perturbations are outside the range of validity of the linear models. For control purposes, it appears to be sufficient to capture the initial transients (approximately one period), during which the instability is suppressed to a great extent. We remark that one could possibly compute nonlinear models by projecting the full nonlinear

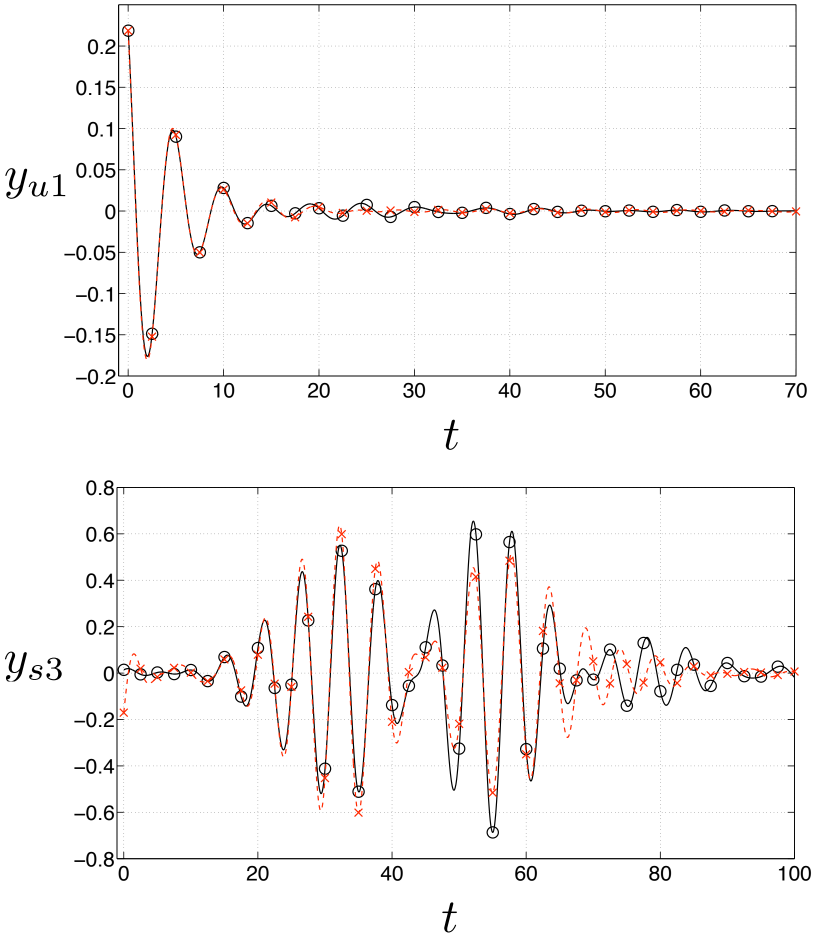

Figure 3.15: Control gain obtained using LQR, and the initial condition is that obtained by an impulsive input to the system with leading edge actuation. Control is turned on at $t = 0$. Comparison of the outputs y_{u1} and y_{s3} of a 12-mode reduced-order model (- - - -, ×) with the projection of data from the linearized simulation (——, ∘).

equations onto the balancing modes, or enhance the model subspace by adding POD modes of vortex shedding and the shift modes as proposed by Noack *et al.* (2005) to account for the nonlinear terms.

Finally, we note that the reduced-order model (2.57) decouples the dynamics on the stable and unstable subspaces, and also, the dynamics on the unstable subspace can be computed only using the unstable eigen-bases Φ_u and Ψ_u. Thus, we could derive a control gain $K \in \mathbb{R}^{1\times n_u}$, based only on the two-dimensional unstable part of the model, such that the eigenvalues of $(\widetilde{A}_u - \widetilde{B}_u K)$ are in the left half complex plane. That is, we can obtain a stabilizing controller *without* modeling the stable subspace dynamics. We have performed simulations to test such a controller and found that it also is capable of suppressing the periodic vortex shedding and thus results in a large basin of attraction for the stabilized steady state. The choice of

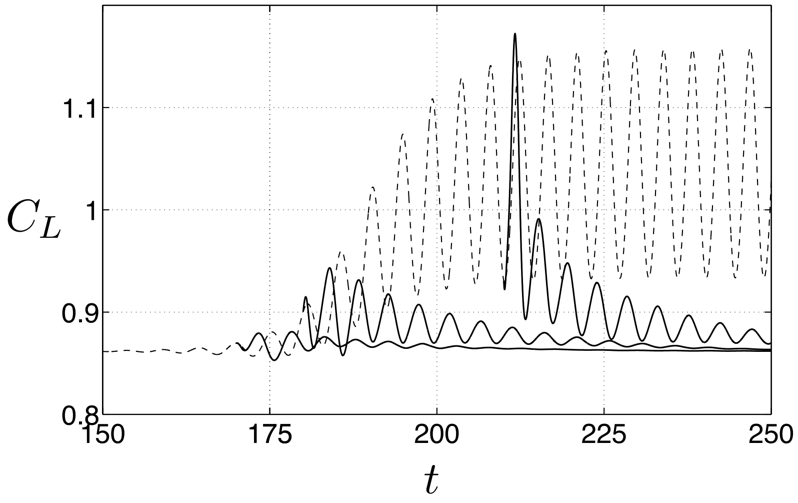

Figure 3.16: Leading edge actuation. Lift-coefficient C_L vs. time t, for full-state feedback control, with control turned on at different times in the base uncontrolled simulation. The base case with no control (‒ ‒ ‒ ‒) has the unstable steady state as the initial condition, and transitions to periodic vortex shedding. The control is tested for different initial conditions, corresponding to $t = 170, 180, 210$ of the base case, and stabilizes the steady state in all the cases (———).

weight matrices Q and R in the LQR cost (3.32) needs to be different to obtain a comparable performance. However, as shown in the next section, it is essential to model the stable subspace dynamics to design a practical controller based on an observer that reconstructs the entire flow field using a few sensor measurements.

3.6 Observer-based control

The full-state feedback control of section 3.5 is not directly useful in practice, since it is not possible to measure the entire flow field. Here, we consider a more practical approach of measuring certain flow quantities at a small number of sensor locations. We assume that we can measure the velocities at the sensors shown in Fig. 3.2, in the near-wake of the plate. We remark that, even though these sensors may not be experimentally realizable, they serve as a good testing ground for our models. We will consider both leading and trailing edge actuation.

Using the reduced-order models derived as outlined in section 3.4, we design observers that dynamically estimate the entire flow field. The estimation is then used along with the full-state feedback controllers of section 3.5 to determine the control input. We outline two different approaches for developing these observers.

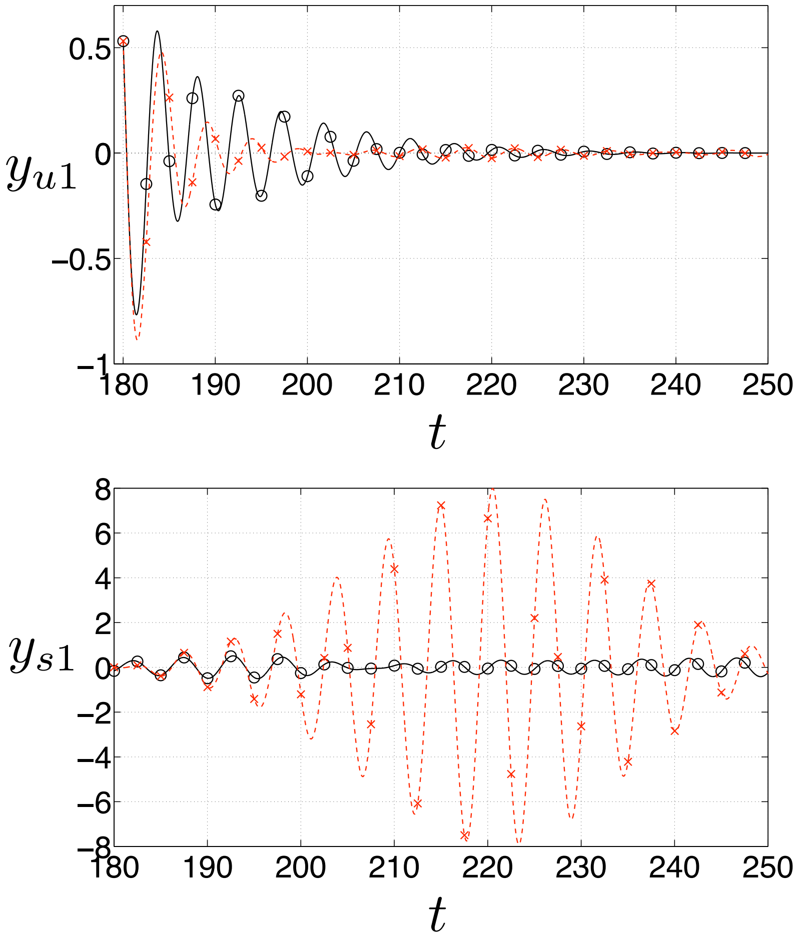

Figure 3.17: Outputs of a system with full-state feedback control using leading edge actuation. The control gain is obtained using LQR, and the initial condition is that corresponding to $t = 180$ of the uncontrolled case plotted in Fig. 3.16. Comparison of the outputs y_{u1} and y_{s1} of a 12-mode (2 unstable and 10 stable modes) reduced-order model (- - - -, ×) with the projection of data from the full nonlinear simulation (———, ∘).

3.6.1 Observer design 1: using models that are not balanced

The approximate balanced truncation method produces reduced models of the input-output response of the original system, and thus the inputs and outputs to the system first need to be defined. In section 3.5, the output was considered to be the entire velocity field, observed as a projection onto a small number of modes using output projection. The output matrix $\widetilde{C}$ of the resulting model (2.57, 2.58) can now be modified to represent the sensor measurements, while retaining $\widetilde{A}$ and $\widetilde{B}$. We replace the output equation (2.58) with

$$y = M \begin{pmatrix} \widetilde{C}_u & \widetilde{C}_s \end{pmatrix} a \overset{\text{def}}{=} \overline{C} a, \tag{3.33}$$

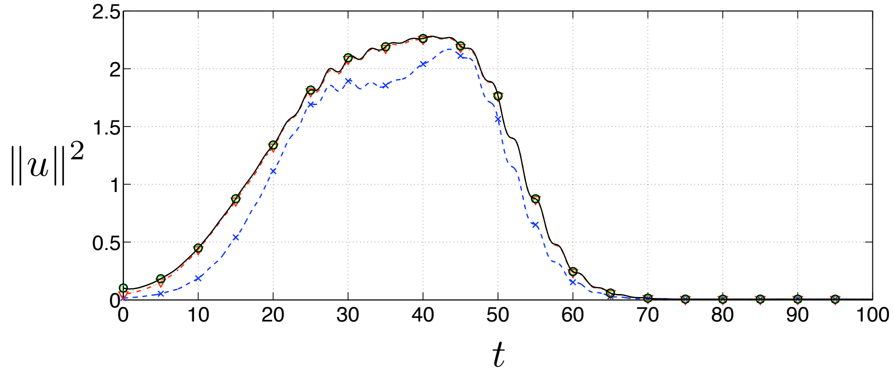

Figure 3.18: The energy of the flow-field (L^2-norm) obtained from an impulse response (——, ○) of (3.30) with leading edge actuation, and the energy captured by 4 (- - - -, ×), 10 (—·—, ▽), and 20 (·······, □) leading POD modes.

where $M \in \mathbb{R}^{s\times n}$ and s is the number of sensor measurements. The matrix M is sparse and extracts the values of the output of (2.57) at the sensor locations; thus, each row of M is filled with 0s except for the entry corresponding to a sensor measurement, which is 1.

Since the observability Gramian corresponding to the pair $(\widetilde{A}, \overline{C})$ is different from that for the pair $(\widetilde{A}, \widetilde{C})$, the model (2.57) with the output represented by (3.33), is not balanced. However, an advantage of using these models is that the cost function (3.32), based on the total kinetic energy of the perturbation velocity, is well captured.

The models used in section 3.5 for full-state feedback were those of a system whose stable-subspace output was the velocity field projected onto the leading 4 POD modes. These 4 POD modes capture only about 85% of the energy, but the resulting models were effective in suppressing vortex shedding. However, for observer design, this representation of the output is inadequate, as the energy content of the flow at the sensor locations is very small, while the POD modes capture the energetically dominant modes. Hence, a greater number of POD modes is required to accurately represent the velocity at the sensor locations. The temporal evolution of the energy content of the flow, obtained from an impulse response of the system restricted to evolve on the stable subspace, is plotted in Figure 3.18. Also plotted is the energy content of the same flow, but projected onto the leading 4, 10 and 20 POD modes; thus, a 4-mode projection leads to noticeable errors, while both 10- and 20-mode projections accurately represent the energy. The velocity field at the sensor locations, reconstructed by 10 and 20 POD modes, plotted in Figure 3.19, shows that a 10-mode projection does not accurately represent the velocities at the sensor locations. Since 20 POD modes are sufficient to represent these velocities, we derive models using a *20-mode output projection*, and use the same for observer design.

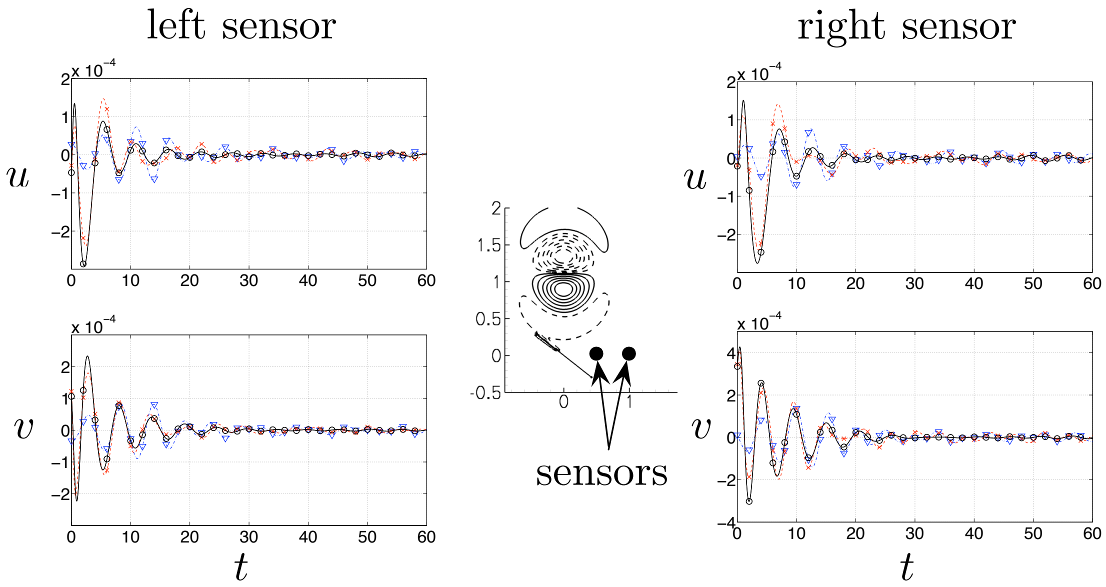

Figure 3.19: Velocities at the sensor locations (———, ∘), of an impulse response of (3.30) with leading edge actuation, compared with the reconstruction using 10 (—·—, ▽) and 20 (- - - -, ×) leading POD modes.

3.6.2 Observer design 2: develop balanced models

The more systematic approach is to construct reduced-order models of the system with the outputs corresponding to the sensor measurements. Since the number of outputs is typically small (here, we consider two velocity sensors), the output projection step is not required. The models are obtained using:

1. The approximate balanced truncation described in section 2.2.2, for which we need two adjoint impulse response simulations. We note that the linearized Navier-Stokes equations (3.16, 3.17) are differential-algebraic equations (DAEs), with the algebraic equations (3.17) imposing the constraint that enforces the velocity fields to remain divergence-free and to satisfy the no-slip boundary conditions at the flat plate surface. The adjoint equations for these DAEs are appropriately derived using the procedure outlined in appendix B.2. As a result, instead of (2.27, 2.2), the adjoint equations are given by:

$$\dot{z} = \mathbb{P}_H A^* z + \mathbb{P}_H C^* v \tag{3.34}$$

$$w = B^* z, \tag{3.35}$$

   where $\mathbb{P}_H$ is an orthogonal projection onto the range of nullspace of $EC(C^TC)^{-1}$, which defines the algebraic constraint (3.17).

2. The eigensystem realization algorithm (ERA) described in section 2.3, which results in the same models (of the stable subspace dynamics) as approximate balanced truncation at a lower computational cost. The method does not require adjoint simulations and only the impulse-response simulations of the

linearized system (3.16, 3.17), projected onto the stable subspace. The only information that needs to be stored is the velocity measurements at the sensor locations, which form the Markov parameters (2.69). The reduced-order models (of the stable subspace dynamics) is given by (2.73, 2.74).

The models obtained using the above methods are balanced and thus capture the most controllable and observable modes. In order to design the controllers using these models, the LQR weight is again chosen to be $Q = \widetilde{C}^*\widetilde{C}$, which in this case seeks to minimize the energy of the output signal.

3.6.3 Modeling of process and sensor noise

The reduced-order models derived above are now used to develop observers using a Linear Quadratic Gaussian (LQG) estimation. This method assumes that the errors in representing the state a and and the measurement y (due to the inaccuracies of the model) are stochastic Gaussian processes, and results in an estimate $\hat{a}$ of the state a that is optimal in the sense that it minimizes the mean of the squared error; refer to Skogestad & Postlethwaite (2005) for details. We now discuss briefly our procedure for modeling these noises; consider the reduced-order model (2.57, 2.58), but with process noise w and sensor noise v which enter the dynamics as follows:

$$\dot{a} = \widetilde{A}a + \widetilde{B}u + w \tag{3.36}$$

$$y = \widetilde{C}a + v. \tag{3.37}$$

A key source of the process (state) noise w arises from model truncation, and second, from ignoring the nonlinear terms in the reduced-order model. The nonlinearity of the dynamics is important, for instance, when the model is used to suppress vortex shedding. A source of the sensor noise arises from two sources; first, the state x is approximated as a sum of a finite number of modes (2.49), and second, in the output projection step (if used), the output is considered as a projection of the (approximated) state x onto a finite number of POD modes (2.55). Here, we approximate these two noises as Gaussian processes whose variances are

$$Q = E(ww^*), \qquad w = f(a_{meas}) - \widetilde{A}a_{meas}, \tag{3.38}$$

$$R = E(vv^*), \qquad v = y - \overline{C}a_{meas}, \tag{3.39}$$

and $E(\cdot)$ gives the expected value. Here, $f(\cdot)$ is the operator obtained by projecting the nonlinear Navier-Stokes equations (3.1) onto the balancing modes Φ, using the adjoint modes Ψ. The state a_{meas} is obtained by projecting the snapshots, obtained from a representative simulation of the full nonlinear system, onto the balancing modes. The representative simulation we used here is the base case, with no control, shown in Fig. 3.16, which includes the transient evolution from the steady state to periodic vortex shedding. The resulting estimator is of the form:

$$\dot{\hat{a}} = \widetilde{A}\hat{a} + \widetilde{B}u + L(y - \overline{C}\hat{a}), \tag{3.40}$$

$$\hat{y} = \overline{C}\hat{a}, \tag{3.41}$$

where $\hat{a}$ is the estimate of state a, $\hat{y}$ is the estimated output, and L is the observer gain. The estimator is then used along with the full-state feedback controller designed in section 3.5 to determine the control input; a schematic is shown in Fig. 3.20.

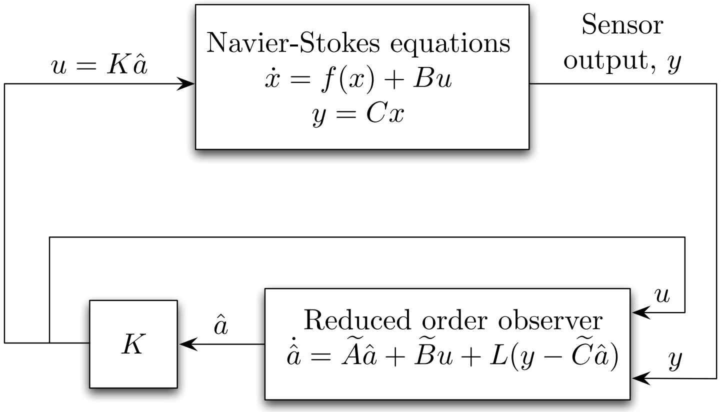

Figure 3.20: Schematic of the implementation of observer-based feedback control in the nonlinear simulations. The control input u and the sensor measurements y are used as inputs to the observer, which reconstructs the reduced-order state $\hat{a}$. This state is then multiplied by the gain K, to obtain the control input u. Both, the controller and observer gains K and L are computed based on the reduced-order model using LQR and LQG respectively.

3.6.4 Observer-based control

Observers using method 1: models are not balanced

The models obtained using the modified output (3.33) are used to design dynamic observers based on the vertical (v-) velocity measurements at the sensor locations. A 22-mode reduced-order model, with 2 and 20 modes describing the dynamics on the unstable and stable subspaces respectively, is used to design a Kalman filter for producing an optimal estimate of the velocity field based on Gaussian approximations of error terms (3.38, 3.39). This estimate is then used along with reduced-order controller to determine the control input, as shown in Fig. 3.20. The results of this observer-based controller (or compensator) are shown in Figs. 3.21, 3.22. Initially, the observer has no information about the states (the initial condition is zero), but it quickly converges to and follows the actual states. There is a key difference from the full-state feedback control, that the compensator does not stabilize the unstable operating point but converges to its small neighborhood. Thus, although the controller gains are chosen to stabilize the operating point of the reduced model, it is unstable in the full system. This is a result of the approximations that enter in the modeling procedure, namely, that of the state by projecting onto balancing modes and the output by means of projection onto POD modes.

Observers using method 2: balanced models using ERA

The reduced-order models are designed using ERA with the sensor measurements as at the output. In the case of point measurement outputs, the cost benefit of ERA is much greater (in comparison to the full-state output), as no inner-products are required to compute the Markov parameters (2.69, 2.80). In comparison, the balanced POD procedure still requires the computation of $m_c m_o$ block inner products to compute the Hankel matrix (2.83). Thus, ERA allows easy experimentation with different choices of actuators and different controller and observer gains. The trailing edge actuator resulted in better closed-loop performance over the leading-edge actuator; the results are shown in Figs. 3.23, 3.24. Again, initially the observer has no information about the states, but soon converges to the actual states; see Fig. 3.24, where, since the actual states cannot be computed using ERA, a comparison of the actual and estimated outputs is given. Further, from Fig. 3.23, we see that the unstable operating point is indeed stabilized in this case.

We experimented with a few other actuators, such as narrower actuation near the leading edge and mid-chord, but neither resulted in stabilizing controllers. Although ERA allows for easy experimentation, the method of choosing actuators remains ad-hoc and a more systematic approach towards actuator and sensor placement is required; further discussion is provided in the concluding chapter.

3.7 Summary

The model reduction techniques developed in chapter 2 were applied in this chapter to develop controllers for the 2-D low-Reynolds-number flow past a flat plate at a large angle of attack α, where the natural flow state is periodic vortex shedding. We performed a continuation study at $\mathsf{Re} = 100$ and computed the branch of steady states with α varying from 0 to 90°; we show that the flow undergoes a Hopf bifurcation from steady state to periodic shedding at $\alpha \approx 27°$. We performed a linear stability analysis of these steady states and presented the growth rate and frequencies of the leading eigenmodes. We developed reduced-order models of the linearized dynamics at $\alpha = 35°$, considering two different actuators modeled as a localized body force close to the leading and trailing edges of the plate. The outputs were first considered to be the entire flow field, projected onto the unstable eigenmodes and the leading POD modes of the impulse response simulation (restricted to the stable subspace). We developed stabilizing controllers based on

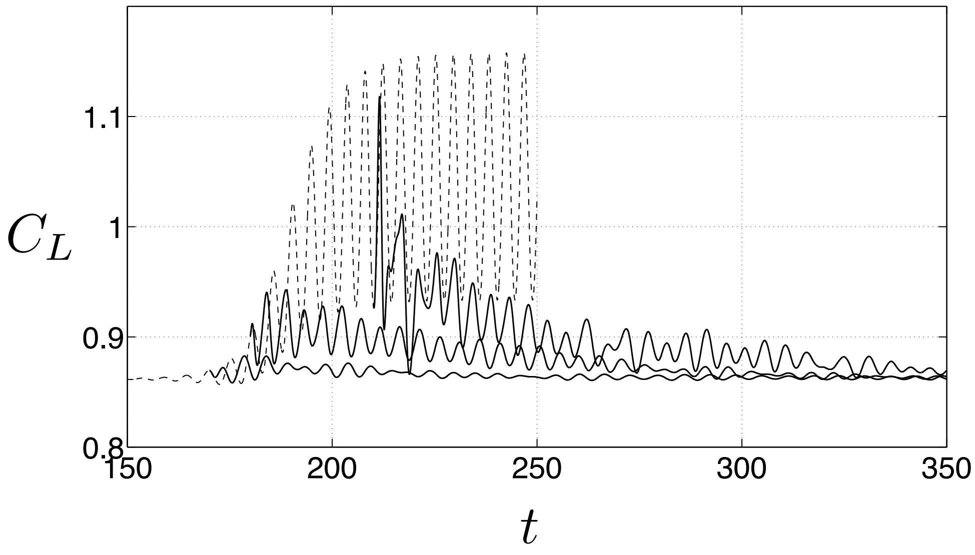

Figure 3.21: Lift-coefficient C_L vs. time t, for estimator-based feedback control, with control turned on at different times in the base uncontrolled simulation. The base case (– – – –) is the same as in Fig. 3.16, and the control is tested for different initial conditions, corresponding to $t = 170, 180, 210$ of the base case (———). In both the cases, the controller stabilizes the flow to a small neighborhood of the steady state.

the reduced-order models to stabilize the unstable steady state and showed that the models agreed well with the actual simulations. We also included the controllers in the full nonlinear simulations, and showed that they had a large-enough basin of attraction to even suppress the vortex shedding. For such large perturbations, however, the model agreement with the full simulation was good only for short times. We also developed more practical controllers by considering an observer-based control design, in which the outputs were modified to be just two near-wake velocity measurements. The nonlinear terms in the equations, which our models do not capture, were treated as process noise, and the error in modeling the outputs was treated as sensor noise. We designed a 22-mode reduced-order observer which reconstructed the flow field accurately, and along with the controllers, suppressed vortex shedding and stabilized the flow in a small neighborhood of the unstable steady state. We remark that the actuator and sensors considered here are not practically realizable, but the methodology presented here can be extended to a more practical actuation such as blowing and suction through the plate and measurements using surface pressure sensors.

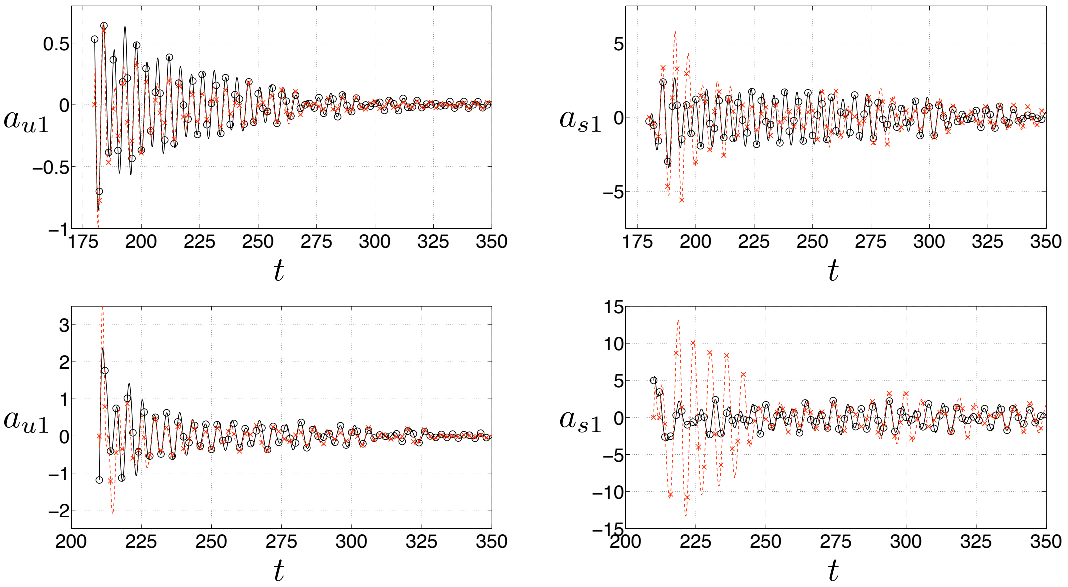

Figure 3.22: States of the system with observer-based control; the states reconstructed (----, ×) by a 22-mode observer quickly converge to the actual states (——, ∘). The initial conditions used are those corresponding to $t = 180, 210$ (top and bottom) of the uncontrolled case shown in Fig. 3.21.

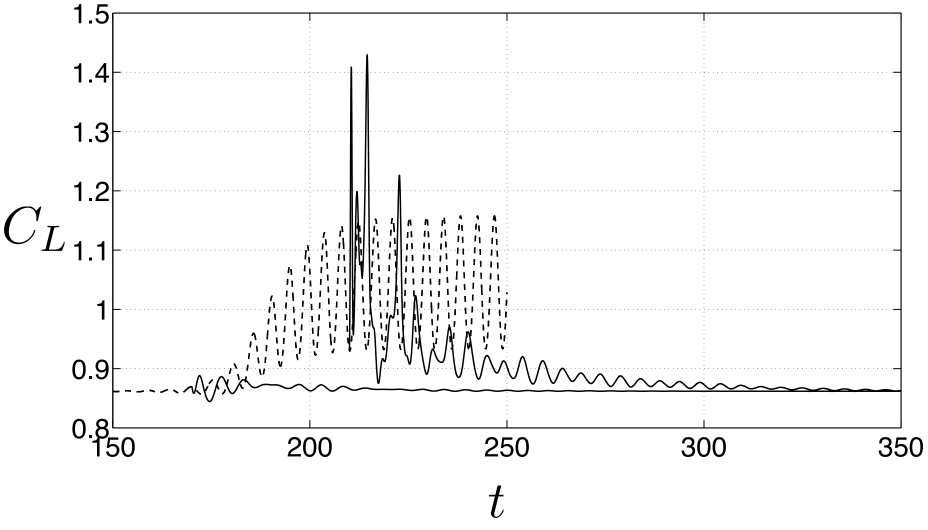

Figure 3.23: Trailing edge actuation and models obtained using ERA. Lift-coefficient C_L vs. time t, with the different curves similar to that in Fig. 3.21. The controller stabilizes the unstable steady state for all initial conditions.

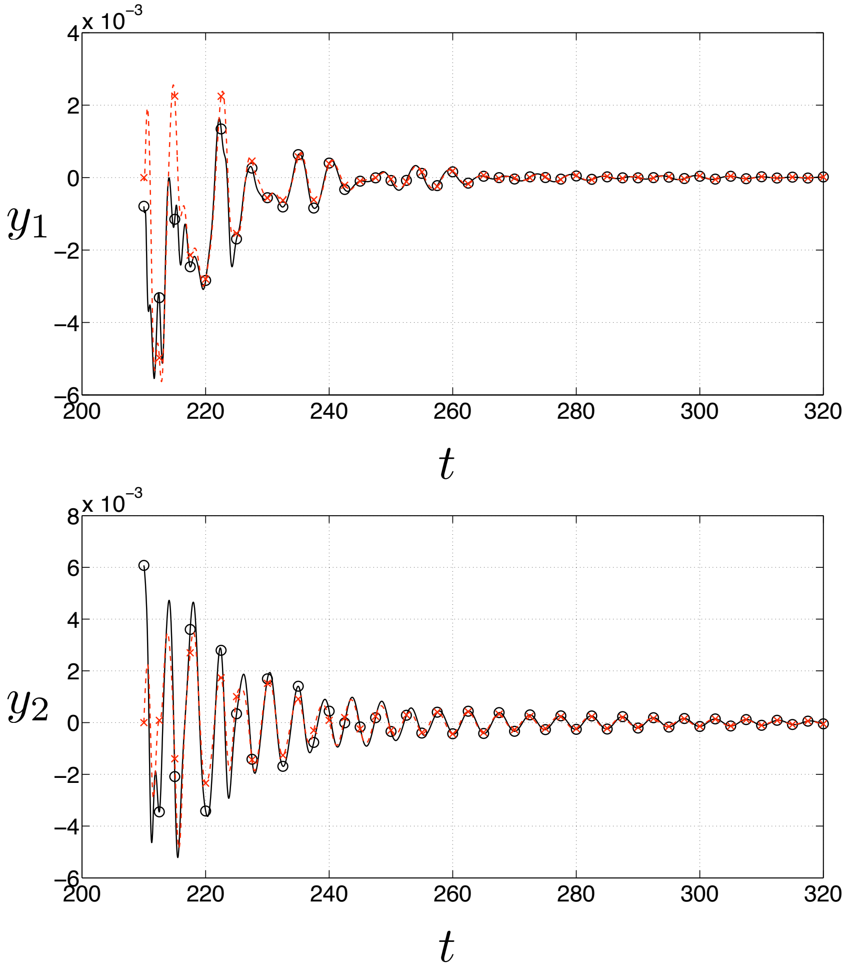

Figure 3.24: Outputs of the system with observer-based control; trailing edge actuation is used and the models are obtained using ERA. The outputs reconstructed (----, ×) by a 22-mode observer quickly converge to the sensor measurements (——, ∘). The initial conditions used are those corresponding to $t = 210$ of the uncontrolled case shown in Fig. 3.23.

Chapter 4

Symmetry reduction for stabilization of relative equilibria

The previous two chapters dealt with exploiting the low-dimensionality of the behavior of certain fluid flows, typically characterized by large coherent structures, in order to obtain reduced-order models of the governing Navier-Stokes equations. In this chapter, we consider fluid flows that are characterized by another structure, that of symmetry: some examples include Taylor-Couette flow, Rayleigh Bénard convection, circular jets and plane channel flow, all of which have translation, rotation or reflection symmetries. Analysis of the physics of these flows, which is rich in terms of the bifurcations that take place, has benefited immensely from symmetry-reduction methods developed using group theory; see the review article by Crawford & Knobloch (1991) and also the volumes by Golubitsky & Schaeffer (1985); Golubitsky *et al.* (1988).

Control of fluid flows with symmetry has also been an active area of research. For example, Weisberg *et al.* (1997) and Marques & Lopez (1997) studied the Taylor-Couette flow and showed that the formation of Taylor vortices could be delayed to larger rotation rates of the inner cylinder by harmonic axial sliding of the inner cylinder, while Sinha *et al.* (2006) and Avila *et al.* (2007) investigated symmetry-breaking bifurcations to more complex behavior in the same flow at higher rotation rates. Tang & Bau (1998) and Or *et al.* (2001) developed controllers to delay the onset of Rayleigh-Bénard convection. Add more examples.

An important class of solutions of systems with a continuous symmetry are *relative equilibria*, which are states that evolve only in the symmetry direction. For example, in a translationally invariant system, relative equiibria are simple traveling waves that move at a constant speed, while their shape remains unchanged. Other simple examples are standing, rotating, and modulated waves, and spiral and Taylor vortices; see the introduction of Roberts *et al.* (2002) for examples in various other systems. In this chapter, we develop controllers that stabilize unstable relative equilibria, by using symmetry reduction methods that borrow ideas from Lie group theory widely used in geometric mechanics (Marsden, 1992; Marsden & Ratiu, 1994).

In this chapter, we employ symmetry reduction using a template-based method developed in Rowley & Marsden (2000) and generalized to self-similar systems in Rowley *et al.* (2003). The method has been used by Wei & Rowley (2009), in combination with proper orthogonal decomposition (POD), to develop models of a free shear layer with self-similar spreading; models were developed in a scaled frame of reference obtained by factoring out the self-similarity. We extend the template-based method to systems with control and obtain equations in a symmetry-reduced frame of reference. The relative equilibria of the original system are fixed points of these reduced equations. Our controller design methodology is based on the linearization of the reduced equations about such fixed points, and is simple to implement as it relies on standard linear control techniques. We illustrate our approach using three examples: a planar rotationally invariant ODE, an inverted pendulum on a cart, and the translationally invariant Kuramoto-Sivashinsky equation in one spatial dimension. The work presented in this chapter has been published in Ahuja *et al.* (2007).

4.1 Template-based reduction

In this section, we first describe the *method of slices* introduced in Rowley *et al.* (2003) to obtain equations in a frame of reference in which the symmetry of the system has been factored out, and extend it to systems with control. More precisely, given dynamics on a manifold $\mathcal{M}$ that are equivariant to the action of a Lie group G, the procedure results in reduced dynamics that evolve on a subspace of $\mathcal{M}$ that is locally diffeomorphic to the quotient space $\mathcal{M}/G$. In many standard examples, (e.g., Lie-Poisson or Euler-Poincare reduction (Marsden & Ratiu, 1994), in which $\mathcal{M} = T^*G$ or TG), this quotient space may be constructed explicitly (e.g., it is $\mathfrak{g}^*$ or $\mathfrak{g}$), but in other examples, such as equivariant PDEs, it is often not clear how to write coordinates on the quotient space, and this is where the present method is useful.

4.1.1 Template dynamics of systems with control

Consider the evolution equations on an n-dimensional manifold $\mathcal{M}$ with control inputs $u \in \mathcal{U}$

$$\dot{z} = X(z, u) \tag{4.1}$$

where $z(t) \in M$, $\dot{z} := dz/dt$ and the initial condition is $z(0) = z_0$. Suppose that the dynamics of (4.1) are equivariant to the action of a d-dimensional Lie group G. The action of G on $\mathcal{M}$ is $\Phi_g : \mathcal{M} \to \mathcal{M}$, that on $\mathcal{U}$ is $\Psi_g : \mathcal{U} \to \mathcal{U}$ and we assume that both actions are free and proper, so that the quotient space M/G is a smooth manifold; see Marsden & Ratiu (1994). The equivariance of (4.1) implies that $\forall z \in \mathcal{M},\ \forall u \in \mathcal{U},$ and $\forall g \in G$,

$$X(\Phi_g(z), \Psi_g(u)) = T\Phi_g(X(z, u)) \tag{4.2}$$

where $T\Phi_g : TM \to TM$ is the tangent of the action on M. Further, we assume that with zero input $u = 0$, the vector field in (4.1) is $X(z, 0) = X(z)$.

In what follows, we will use the short-hand concatenation to denote all the group actions:

$$g \cdot z := \Phi_g(z) \qquad \forall z \in \mathcal{M}, \tag{4.3}$$

$$g \cdot v := T\Phi_g(v) \qquad \forall v \in T\mathcal{M}, \tag{4.4}$$

$$g \cdot u := \Psi_g(u) \qquad \forall u \in \mathcal{U}. \tag{4.5}$$

The idea behind the method of slices is that we decompose the solution $z(t)$ of (4.1) and the input $u(t)$ as

$$z(t) = g(t) \cdot \tilde{z}(t) \tag{4.6}$$

$$u(t) = g(t) \cdot \tilde{u}(t) \tag{4.7}$$

where $g(t)$, $\tilde{z}(t)$, and $\tilde{u}(t)$ are curves in G, $\mathcal{M}$, and $\mathcal{U}$ respectively. The value of $g(t)$ is to be chosen such that $\tilde{z}(t)$ is constrained in a useful manner: in particular, it evolves on a subspace locally diffeomorphic to the quotient space $\mathcal{M}/G$. Substituting (4.6, 4.7) into (4.1) and using equivariance (4.2), we obtain

$$\dot{\tilde{z}} = X(\tilde{z}, \tilde{u}) - \xi_{\mathcal{M}}(\tilde{z}), \tag{4.8}$$

where, $\xi_M : M \to TM$ is the infinitesimal generator of the action Φ_g in the direction $\xi(t) = g^{-1}\dot{g} \in \mathfrak{g}$, the Lie algebra of G; it is defined by

$$\xi_M(\tilde{z}) = \left.\frac{d}{ds}\right|_{s=0} h(s) \cdot \tilde{z}, \tag{4.9}$$

where $h(s)$ is a curve in G such that $h(0) = Id$, $dh/ds(s = 0) = \xi$. See Rowley *et al.* (2003) for the details leading to equation (4.8). Note that the vector field (4.8) is the same as that of (4.1) with an additional term subtracted. This additional term depends on $\xi(t)$ (and hence on $g(t)$), the choice of which so far has been arbitrary. As discussed in Rowley *et al.* (2003) and Beyn & Thümmler (2004), there are several ways to place a constraint on $\xi(t)$ such that the dynamics of $\tilde{z}(t)$ are restricted to a subspace that is isomorphic to $\mathcal{M}/G$. The template-based method, or the method of slices, is one such way described in Rowley *et al.* (2003).

In order to use the template-based method, we assume that $\mathcal{M}$ is a vector space endowed with an inner product, denoted by $\langle \cdot, \cdot \rangle$. We then choose a *template* $z_0 \in \mathcal{M}$ and choose a constraint on $\tilde{z}(t)$ so that, in time, it remains "aligned with" the template z_0 in the following sense: $h = Id$ is a local minimum of $\|\tilde{z} - h \cdot z_0\|$. This

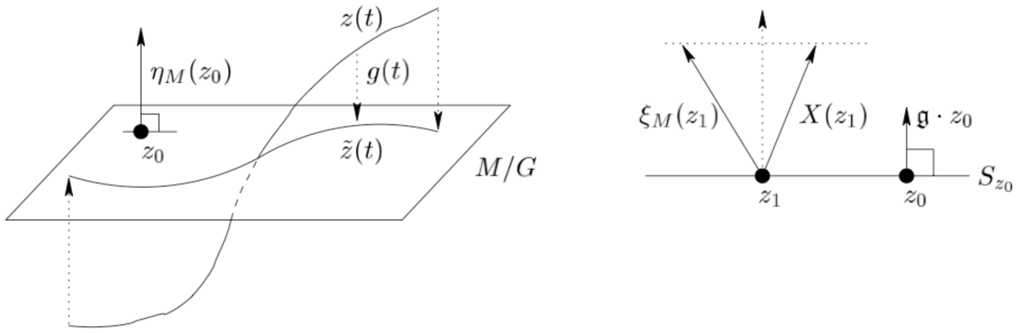

Figure 4.1: Method of slices

condition is equivalent to requiring $\tilde{z}(t)$ to lie in an affine space S_{z_0} defined by

$$S_{z_0} = \{\tilde{z} \in \mathcal{M} \mid \langle \tilde{z} - z_0, \eta_{\mathcal{M}}(z_0)\rangle = 0, \, \forall \eta \in \mathfrak{g}\}. \tag{4.10}$$

We call this set the slice through z_0. As shown in Fig. 4.1, the slice S_{z_0} may be interpreted as an $(n-d)$-dimensional affine space containing z_0 and orthogonal to the group orbit through z_0. It can be shown that this slice is locally isomorphic to the quotient space M/G, consisting of equivalence classes of M in which two points in M related by the group action are identified. Thus, in writing the decomposition (4.6, 4.7) and choosing $\tilde{z}(t)$ to lie in the slice, we effectively move to a reference frame in which the motion in the group direction has been factored out.

Now, differentiating (4.10) with respect to time and using (4.8), we find that requiring $\tilde{z}(t)$ to live on the slice is equivalent to requiring $\langle \dot{\tilde{z}}, \eta_{\mathcal{M}}(z_0)\rangle = 0$, $\forall \eta \in \mathfrak{g}$. This gives a set of d algebraic equations for ξ (recall that $d = \dim(G)$):

$$\langle X(\tilde{z}, \tilde{u}) - \xi_{\mathcal{M}}(\tilde{z}), \eta_{\mathcal{M}}(z_0)\rangle = 0, \quad \forall \eta \in \mathfrak{g}. \tag{4.11}$$

Equation (4.11) essentially means that ξ is chosen such that the projection of the vector field $X(\tilde{z})$ and of $\xi_M(\tilde{z})$ onto the direction perpendicular to the slice S_{z_0} is the same: refer to the right hand part of Fig. 4.1. Equations (4.8, 4.10) are the *reduced or slice dynamics* of (4.1) and are evolution equations for the shape variable $\tilde{z}(t)$. To get the full solution $z(t)$, we still need $g(t)$, for which we have the following *reconstruction equations*:

$$g^{-1}\dot{g} = \xi(t) \tag{4.12}$$

where, for a given $\tilde{z}(t)$, $\xi(t)$ is given by (4.11). The slice dynamics for the open loop or uncontrolled equations can be obtained by simply setting $\tilde{u} = 0$ in (4.8, 4.10).

Note that the constraint (4.11) in general depends on the control input $\tilde{u}$, which means that $\xi(t)$ and $g(t)$ depend on $\tilde{u}$. Thus, in general, the control input affects the group variables as well as the shape variables. We are particularly interested in the way the control input splits between these two variables.

4.1.2 Control objective

A fixed point of the slice dynamics of (4.1) is a relative equilibrium of (4.1). Assume that $\tilde{z}_s$ is a fixed point of the slice dynamics of (4.1) with no control input, that is, $\tilde{z}_s$ is a fixed point of (4.8, 4.11) with $\tilde{u} = 0$. Then, the corresponding solution of (4.1) is given by $z(t) = g(t) \cdot \tilde{z}_s$, which is a relative equilibrium.

We want to find feedback laws such that $\tilde{z}_s$ is an asymptotically stable fixed point of (4.8), with control, thus stabilizing the whole group orbit $G \cdot \tilde{z}_s$ of the original system. We consider two different ways in which the control input appears in the closed loop equations.

1. Assume that the dynamics are affine in the control input and that the available actuation is equivariant. Then, we find feedback laws that minimize a prescribed quadratic cost function that is invariant to the group action.
2. Assume that we don't have equivariant actuators but that the actuators can be "translated" in the group direction using an additional control input. Then, we obtain feedback laws by restricting the control to affect only the shape space and not the group space. Such a control has been called *internal actuation* in Jalnapurkar & Marsden (2000).

4.2 Control of differential-algebraic equations

The slice dynamics (4.8, 4.10) form a set of differential-algebraic equations (DAEs), and the control of such systems has been extensively studied; see Dai (1989); Verghese *et al.* (1981); Cobb (1981, 1983); Krishnan & McClamroch (1992); Kumar & Daoutidis (1995, 1996, 1999) for examples. Equation (4.10) constrains the dynamics of (4.8) to live on the slice S_{z_0}. That is, S_{z_0} is an $(n-d)$-dimensional invariant subspace of (4.8, 4.10), and it is the dynamics on this subspace that we want to control.

The feedback control problem of a class of nonlinear DAEs that is relevant here was addressed in Kumar & Daoutidis (1995, 1996, 1999); the procedure developed in these papers is as follows. First, an algorithmic procedure is outlined to eliminate the constraints and obtain an equivalent state-space realization of the DAEs. The feedback synthesis is based on this state-space realization, using tools from linear or nonlinear systems. The slice dynamics fall under this class of DAEs and we use the same procedure, outlined as follows, to derive a state-space realization and derive stabilizing feedback laws:

1. Differentiate the algebraic constraint (4.10) with respect to time and use the ODEs (4.8) to obtain an explicit expression for ξ in terms of $\tilde{z}$ (4.11).

2. Substitute for ξ in (4.8) to get a set of n-ODEs, which have the slice S_{z_0} as a d-dimensional invariant subspace. As we will show more explicitly later in this section, the slice is an affine subspace of M.
3. Linearize the ODEs about the relative equilibrium, which is a fixed point of this system. Since the slice dynamics have the slice as a *linear* invariant subspace, the resulting linearized ODEs also have the same invariant subspace.
4. Use equation (4.10) of the slice S_{z_0} to eliminate d equations from (4.8) to get an $(n-d)$-dimensional state space realization.
5. Use tools from linear control theory to find stabilizing feedback laws.

4.2.1 Linearization about a relative equilibrium

Here, we derive an expression for the linearization of the slice dynamics about the fixed point in the slice. For that, it is helpful to use the fact that the infinitesimal generator $\xi_{\mathcal{M}}(z)$ is linear in ξ and thus can be expressed in the following form:

$$\xi_{\mathcal{M}}(z) = Y(z)\xi \tag{4.13}$$

where $Y(z) : \mathfrak{g} \to T_z\mathcal{M}$ is linear. Assuming that M is an inner product space and using (4.13), the equation of the slice (4.10) simplifies as follows:

$$\langle z - z_0, Y(z_0)\eta\rangle = 0, \quad \forall \eta \in \mathfrak{g}, \tag{4.14}$$

$$\implies \quad Y^*(z_0)(z - z_0) = 0. \tag{4.15}$$

where $Y^*(z_0) : T\mathcal{M} \to \mathfrak{g}$ is the adjoint of $Y(z_0)$. Thus, the slice S_{z_0} is the space of all vectors $z - z_0$ in the null space of $Y^*(z_0)$ and this subspace forms an $(n-d)$-dimensional affine subspace.

With the form (4.13) of the infinitesimal generator, we can obtain an explicit form for ξ that appears in the slice dynamics (4.8). Since ξ satisfies (4.11), we have

$$\langle X(\tilde{z}, \tilde{u}) - Y(\tilde{z})\xi, Y(z_0)\eta\rangle = 0, \quad \forall \eta \in \mathfrak{g}. \tag{4.16}$$

$$\text{Thus,} \qquad \xi = \Big(Y^*(z_0)Y(\tilde{z})\Big)^{-1} Y^*(z_0)X(\tilde{z}, \tilde{u}). \tag{4.17}$$

Substituting for ξ into (4.8) from (4.17) results in a purely differential system of equations.

We assume that the template has been chosen such that $(Y^*(z_0)Y(\tilde{z}))^{-1}$ exists. We will explore the physical significance of this assumption with specific examples in section 4.5. If we use $z_0 = \tilde{z}(t)$ and assume $Y(\tilde{z})$ to have full rank, then Y^*Y will always be invertible. This choice of a time-dependent template gives a different method for deriving reduced dynamics, which was introduced and called as the *method of connections* in Rowley *et al.* (2003). However, unlike the method of slices, the resulting reduced dynamics do not have an invariant subspace (in the terminology of Rowley *et al.* (2003), the connection is not flat) containing a unique equilibrium. As our control method relies on the existence of such an invariant subspace, we use the method of slices throughout this work.

Now we are ready to derive an expression for the linearized dynamics in the neighborhood of a fixed point $\tilde{z}_s$. Let $\tilde{z} = \tilde{z}_s + w$ and $\tilde{u} = 0 + v$, where $\|w\|, \|v\| \ll 1$ are small perturbations about the fixed point and zero input. We think of w as a perturbation restricted to lie within the slice. Substituting this expansion in (4.8), where ξ is given by (4.17), and simplifying gives (refer to appendix C for a derivation)

$$\begin{aligned} \dot{w} =& \mathbb{P}_{S_{z_0}} \Big(D_{\tilde{z}} X(\tilde{z}_s, 0) w + D_{\tilde{u}} X(\tilde{z}_s, 0) v \Big) \\ &- \mathbb{P}_{S_{z_0}} D_{\tilde{z}} Y(\tilde{z}_s) w \Big(Y^*(z_0) Y(\tilde{z}_s) \Big)^{-1} Y^*(z_0) X(\tilde{z}_s, 0) + O(2) \qquad (4.18) \\ \stackrel{\text{def}}{=}& \mathbb{P}_{S_{z_0}} (\hat{A} w + \hat{B} v) + O(2), \qquad (4.19) \end{aligned}$$

where $O(2)$ represents terms second or higher order in w and v. Here, $\mathbb{P}_{S_{z_0}}$ is a projection onto the slice, i.e., the space orthogonal to the range of $Y(z_0)$:

$$\mathbb{P}_{S_{z_0}} = I - Y(\tilde{z}_s) \Big(Y^*(z_0) Y(\tilde{z}_s) \Big)^{-1} Y^*(z_0). \qquad (4.20)$$

The linearization (4.19) clearly has an invariant subspace that lives on the slice S_{z_0}. That is, (4.19) identically satisfy the constraint (4.15), which in terms of w is:

$$Y^*(z_0) w = Y^*(z_0)(\tilde{z}_s - z_0) = 0. \qquad (4.21)$$

Now, (4.20) is symmetric if and only if $z_0 = \tilde{z}_s$, that is, if the template is chosen to be the fixed point. In that case, (4.20) is an *orthogonal* projection onto the space orthogonal to the columns of $Y(\tilde{z}_s)$. In what follows and in the rest of this chapter, we will assume that the template chosen to define the slice S_{z_0} is the fixed point of the slice dynamics, $\tilde{z}_s$. Our control design in later sections is based on the linear part of equations (4.19). In particular, we will use LQR to derive optimal feedback laws that stabilize $\tilde{z}_s$.

Linearization about a fixed point

In the special case of the relative equilibrium that is also a steady state of the full dynamics (in which case a continuum of such steady states exist), the linearized equations (4.19) take a much simpler form. For this case, we have $X(g \cdot \tilde{z}_s, 0) = 0$, $\forall g \in G$ and hence the linearized slice dynamics (4.19) become:

$$\begin{aligned} \dot{w} &= \mathbb{P}_{S_{\tilde{z}_s}} (D_{\tilde{z}} X(\tilde{z}_s, 0) w + D_{\tilde{u}} X(\tilde{z}_s, 0) v) + O(2) \qquad (4.22) \\ &\stackrel{\text{def}}{=} \mathbb{P}_{S_{\tilde{z}_s}} (A w + B v) + O(2). \qquad (4.23) \end{aligned}$$

This implies that for linearization about a fixed point of (4.1), the following diagram commutes:

$$\begin{tikzcd}
\dot{z} = X(z,u) \arrow[r, "\text{lin. about } \tilde{z}_s"] \arrow[d, "\text{slice dynamics}"'] & \dot{w} = Aw + Bv \arrow[d, "\mathbb{P}_{S_{\tilde{z}_s}}"'] \\
\dot{\tilde{z}} = X(\tilde{z},\tilde{u}) - \xi_{\mathcal{M}}(\tilde{z}) \arrow[r, "\text{lin. about } \tilde{z}_s"] & \dot{w} = \mathbb{P}_{S_{\tilde{z}_s}}(Aw + Bv).
\end{tikzcd} \tag{4.24}$$

In words, the linearization of the slice dynamics about its fixed point is the same as the projection of the linearized original dynamics (about the same point) onto the slice defined with that fixed point as a template.

4.3 State-space formulation

In this section, we find an equivalent state-space realization of the linear DAEs (4.19, 4.21) by using the constraint equation (4.21) to eliminate d equations from (4.19). First, we write $w = (w_s, w_g)$, where $w_s \in \mathbb{R}^{n-d}$ and $w_g \in \mathbb{R}^d$. Then the equations (4.19) can be written as

$$\begin{pmatrix} \dot{w}_s \\ \dot{w}_g \end{pmatrix} = \underbrace{\begin{pmatrix} A_{s1} & A_{g1} \\ A_{s2} & A_{g2} \end{pmatrix}}_{\mathbb{P}_{S_{\tilde{z}_s}} \hat{A}} \begin{pmatrix} w_s \\ w_g \end{pmatrix} + \underbrace{\begin{pmatrix} B_s \\ B_g \end{pmatrix}}_{\mathbb{P}_{S_{\tilde{z}_s}} \hat{B}} v. \tag{4.25}$$

Similarly, the constraint (4.21) can be written as

$$\underbrace{\begin{pmatrix} Y_s^*(\tilde{z}_s) & Y_g^*(\tilde{z}_s) \end{pmatrix}}_{Y^*(\tilde{z}_s)} \begin{pmatrix} w_s \\ w_g \end{pmatrix} = \mathbf{0}. \tag{4.26}$$

where $Y_s^* \in \mathbb{R}^{d \times (n-d)}$ and $Y_g^* \in \mathbb{R}^{d \times d}$. The splitting $w = (w_s, w_g)$ is chosen such that $Y_g^*(\tilde{z}_s)$ is invertible, so that we can express w_g in terms of w_s. This can always be done as $Y(\tilde{z})$ has full rank. Thus, we have

$$w_g = -(Y_g^*(\tilde{z}_s))^{-1} Y_s^*(\tilde{z}_s) w_s \overset{\text{def}}{=} \Lambda w_s. \tag{4.27}$$

Then the state space realization is obtained by substituting (4.27) in the $\dot{w}_s$ equations in (4.25). The resulting equations are:

$$\dot{w}_s = (A_{s1} + A_{g1}\Lambda) w_s + B_s v \overset{\text{def}}{=} A_s w_s + B_s v. \tag{4.28}$$

Various properties of the linear DAEs such as controllability and stabilizability can now be stated based on the state equations.

4.3.1 Controllability and stabilizability

A simple check for controllability of the slice S_{z_0} is as follows. Construct the controllability test matrix corresponding to the pair $(\mathbb{P}_{S_{z_0}}\hat{A}, \mathbb{P}_{S_{z_0}}\hat{B})$ of (4.19):

$$C = \mathbb{P}_{S_{z_0}} \begin{bmatrix} \hat{B} & (\hat{A}\mathbb{P}_{S_{z_0}})^2\hat{B} & \dots & (\hat{A}\mathbb{P}_{S_{z_0}})^{n-1}\hat{B} \end{bmatrix}. \tag{4.29}$$

Since the span of C defines the controllable subspace of (4.19), the slice S_{z_0} is a controllable subspace of (4.19) iff $\operatorname{rank}(C) = n - d$. Since C is independent of the splitting (4.26), controllability of the slice is also independent of this splitting. However, in general, controllability does depend on the template z_0 chosen to define the slice.

There is another equivalent test for controllability of (4.19), which arises from the theory of control of linear DAEs of the form $E\dot{x} = \bar{A}x + \bar{B}u$, where E is singular. Such systems are treated, for example, in Cobb (1981, 1983) and Dai (1989). To express our system in this form, we ignore the differential equations in the variable w_g from (4.25) and augment the system with the algebraic equations (4.26). This gives us the following set of DAEs:

$$\underbrace{\begin{pmatrix} I & 0 \\ 0 & 0 \end{pmatrix}}_{E} \begin{pmatrix} \dot{w}_s \\ \dot{w}_g \end{pmatrix} = \underbrace{\begin{pmatrix} A_{s1} & A_{g1} \\ Y_s^*(\tilde{z}_s) & Y_g^*(\tilde{z}_s) \end{pmatrix}}_{\bar{A}} \begin{pmatrix} w_s \\ w_g \end{pmatrix} + \underbrace{\begin{pmatrix} B_s \\ 0 \end{pmatrix}}_{\bar{B}} v. \tag{4.30}$$

The above equations are indeed in the form $E\dot{x} = \bar{A}x + \bar{B}u$, where E is a singular matrix with rank $n-d$. Then, from theorem 2-2.1 on page 29 of Dai (1989), we have the following condition for controllability: $S_{\tilde{z}_s}$ is a controllable subspace of (4.19) if and only if

$$\operatorname{rank} \begin{bmatrix} sE - \bar{A} & \bar{B} \end{bmatrix} = n, \qquad \forall s \in \mathbb{C}, \ s \text{ finite}. \tag{4.31}$$

4.4 Feedback control design

In this section, we use the state-space representation of the linearized slice dynamics (4.28) to derive optimal feedback laws that asymptotically stabilize the relative equilibria. First, we find the feedback laws for the linearized reduced system and then we derive the form that these laws take in the full space. Essentially, we could use pole placement to find the feedback gain such that the poles of the resulting closed loop system are in the left half complex plane. We could also use LQR to find feedback laws that minimize a given cost function, quadratic in w_s and v. The trouble with these approaches is that in general the resulting feedback law depends on the way we split w into (w_s, w_g). In order to circumvent this problem, we define the cost function in terms of the *original* variables z and u. Then, we use (4.27) to derive the form this cost function takes in terms of the reduced variables w_s and v. The resulting feedback law is then independent of the choice of (w_s, w_g).

4.4.1 Optimal control with equivariant actuation

We assume that the closed loop dynamics (4.1) are affine in the control input:

$$X(z,u) = X(z) + H(z)u. \tag{4.32}$$

Equivariance of (4.32) implies that $H(z)$ has to satisfy the following property:

$$H(\Phi_g(z)) \circ \Psi_g = T_z\Phi_g \circ H(z), \qquad \forall g \in G, \quad \forall z \in M. \tag{4.33}$$

We seek a feedback law for u such that $\tilde{z}_s$ is a stable fixed point of the slice dynamics of (4.1,4.32) and the following cost function is minimized:

$$J[\tilde{z}, \tilde{u}] = \int_0^\infty \big(\langle \tilde{z} - \tilde{z}_s, Q(\tilde{z} - \tilde{z}_s) \rangle + \langle \tilde{u}, R\tilde{u} \rangle \big)\, dt. \tag{4.34}$$

where $Q : \mathcal{M} \to \mathcal{M}$ and $R : \mathcal{U} \to \mathcal{U}$ are positive definite weights. The cost (4.34) is prescribed to be invariant to the action of G, that is, $J[\Phi_h(z), \Psi_h(u)] = J[z,u]$, for all $h \in G$. This in turn imposes the following restrictions on Q and R:

$$Q = \Phi_{h^{-1}} \circ Q \circ \Phi_h, \tag{4.35}$$

$$R = \Psi_{h^{-1}} \circ R \circ \Psi_h, \quad \forall h \in G. \tag{4.36}$$

Using (4.6,4.7), and the invariance (4.36), the cost (4.34) in terms of the original variables z and u is given by

$$J[z,u] = \int_0^\infty \big(\langle g^{-1} \cdot z - \tilde{z}_s, Q(g^{-1} \cdot z - \tilde{z}_s) \rangle + \langle u, Ru \rangle \big)\, dt, \tag{4.37}$$

where g is as defined in the reconstruction equation (4.12); it is the action that aligns z with the template $\tilde{z}_s$. Then, substituting $\tilde{z} = \tilde{z}_s + w$ and $\tilde{u} = v$ in (4.34) gives the cost function in the variables (w, v). Thus, the problem of finding an optimal feedback law is the same as finding $(w(t), v(t))$ that satisfy (4.19, 4.15) and minimize $J[w, v]$.

As in the previous section, to obtain the state-space realization, we use the constraint (4.26) to eliminate w_g from the cost function; that is $J[(w_s, w_g), v] = J[(w_s, \Lambda w_s), v]$. The cost function thus obtained in terms of w_s only by using (4.27) is

$$J[w_s, v] = \int_0^\infty \big(\langle w_s, \widetilde{Q} w_s \rangle + \langle v, Rv \rangle \big)\, dt. \tag{4.38}$$

It can be easily shown that

$$\text{if} \qquad Q = \begin{pmatrix} Q_{11} & Q_{12} \\ Q_{21} & Q_{22} \end{pmatrix}, \tag{4.39}$$

$$\text{then} \qquad \widetilde{Q} = Q_{11} + Q_{12}\Lambda + \Lambda^* Q_{21} + \Lambda^* Q_{22} \Lambda. \tag{4.40}$$

The optimal control problem can now be stated as follows: find a feedback law $v = \tilde{K} w_s$ such that (w_s, v) satisfy (4.28) and minimize the reduced cost (4.38). If (4.28) is controllable, we have a standard result from linear systems theory that the optimal feedback law $v = \tilde{K} w_s$ is given by $\tilde{K} = -R^{-1} B_s^* M$ where M, which is symmetric and positive definite, is obtained by solving the following $(n-d)$-dimensional algebraic Riccati equation:

$$M A_s + A_s^* M - M B_s R^{-1} B_s^* M + \widetilde{Q} = 0 \tag{4.41}$$

Here, we would like to mention some similarity with the work of Cobb (1983) which considered the problem of finding an optimal feedback law for linear DAEs of the form mentioned earlier in section 4.3.1, that is $E\dot{x} = Ax + Bu$. The author showed that the optimal control can be found by solving a Riccati equation of order p, where p is the rank of E; this is exactly what our method involves as well. As mentioned earlier, our control problem is just a special case of that considered in Cobb (1983) which considers more general systems of DAEs. In general, if the initial conditions are not consistent with the algebraic constraints, the behavior of the system of DAEs consists of impulses at the starting time; Cobb (1983) accounts for such initial conditions as well. We do not consider such initial conditions as we considered perturbations restricted to the slice while deriving the linearized equations.

Finally, the feedback law can be expressed in the original variables w by expressing w_s in terms of w:

$$w_s = (I + \Lambda^* \Lambda)^{-1} \begin{pmatrix} I & \Lambda^* \end{pmatrix} w. \tag{4.42}$$

Here, $I + \Lambda^*\Lambda$ is invertible as $\Lambda^*\Lambda$ is Hermitian and positive definite. Thus,

$$v = \tilde{K} w_s = \tilde{K}(I + \Lambda^* \Lambda)^{-1} \begin{pmatrix} I & \Lambda^* \end{pmatrix} w \overset{\text{def}}{=} K w. \tag{4.43}$$

Form of feedback law in the original frame

Now we derive the form that the feedback law (4.43) takes in the original framework. Since we restricted the closed loop system to be linear in u, then $\tilde{u}$ is the same as its linearization v; thus

$$\tilde{u} = K w = K(\tilde{z} - \tilde{z}_s) \tag{4.44}$$

$$\therefore \quad \Psi_{g^{-1}}(u) = K(\Phi_{g^{-1}}(z) - \tilde{z}_s) \qquad \text{using } (4.6, 4.7) \tag{4.45}$$

$$\text{or} \qquad u = \Psi_g \circ K(\Phi_{g^{-1}}(z) - \tilde{z}_s). \tag{4.46}$$

Here, $g(t)$ is given by solving the reconstruction equation (4.12) and it represents a "translation" of z to the slice $S_{\tilde{z}_s}$. Also, it can be easily shown that the control law (4.46) is independent of the template chosen, provided that the template is a group shift of $\tilde{z}_s$. The choice of feedback law (4.46) for u can be described using Fig. 4.2 as follows. Choose $\tilde{z}$ to be a group shift of z by an amount g^{-1} such that $\tilde{z}$ lies in the slice defined using the template $\tilde{z}_s$. Then, evaluate the difference $\tilde{z} - \tilde{z}_s$ and act on it by the feedback gain K, which gives the input $\tilde{u}$. Finally, the input u is just a group shift of $\tilde{u}$ by the same amount g.

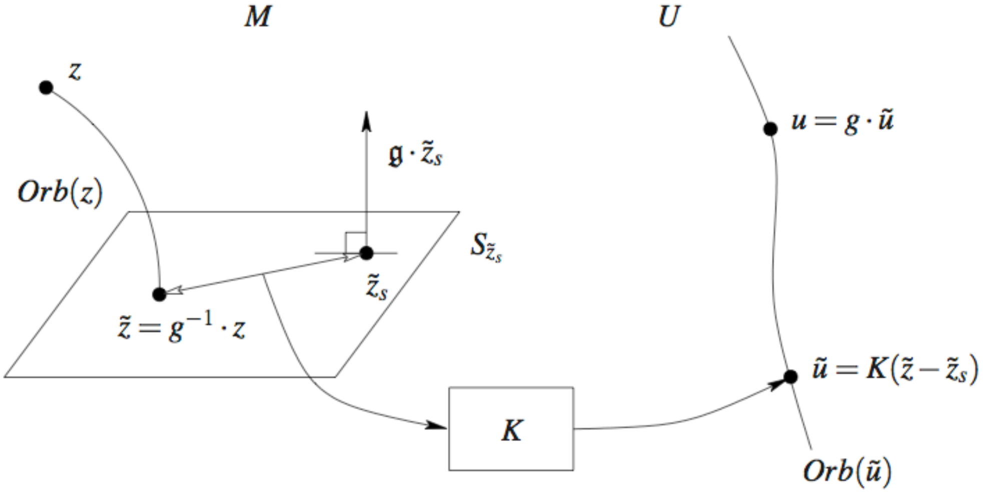
M
U
z
Orb(z)
$\mathfrak{g}\cdot\tilde{z}_s$
$S_{\tilde{z}_s}$
$\tilde{z}_s$
$\tilde{z}=g^{-1}\cdot z$
$u=g\cdot\tilde{u}$
$\tilde{u}=K(\tilde{z}-\tilde{z}_s)$
K
$Orb(\tilde{u})$

Figure 4.2: Feedback control using the method of slices

4.4.2 Amplitude and phase actuation

Here we consider a second approach to control design, where we allow for more general actuators. We do not assume that the given actuator is equivariant to the group action, but we assume that the equivariance of the closed loop vector field results from a freedom to "move the actuator" in the group direction. That is, we assume the closed loop equations to be of the form:

$$\dot{z} = X(z) + \sum_{i=1}^{m} T\Phi_{h_i} \circ b_i u_i, \tag{4.47}$$

where $b_i : \mathbb{R} \to T\mathcal{M}$ are the actuators, and $u_i \in \mathbb{R}$ and $h_i \in G$ are the control inputs. We can think of the input h_i as being the *phase* and the input u_i being the *amplitude* of actuator b_i. The control space $\mathcal{U}$ is defined as $m\,(\leq \dim(M) = n)$ copies of $\mathbb{R} \times G$, and the action Ψ_g on $\mathcal{U}$ is

$$\Psi_g \cdot (u_i,\, h_i) = (u_i,\, g \cdot h_i), \qquad i = 1, 2, \ldots, m. \tag{4.48}$$

Note that each actuator can be moved independently in the group direction, that is, the phase of each actuator b_i can be separately prescribed by the control inputs h_i.

As in section 4.1, in order to derive the slice dynamics of (4.47), we write $z = \Phi_g(\tilde{z})$, where $\tilde{z} \in S_{\tilde{z}_s}$. The resulting equations are:

$$\dot{\tilde{z}} = X(\tilde{z}) + \sum_{i=1}^{m} T\Phi_{g^{-1}h_i} \circ b_i u_i - \xi_{\mathcal{M}}(\tilde{z}), \tag{4.49}$$

where we rewrite the expression for ξ from (4.17) as:

$$\xi = \Big(Y^*(\tilde{z}_s)Y(\tilde{z})\Big)^{-1} Y^*(\tilde{z}_s)\Big(X(\tilde{z}) + \sum_{i=1}^{m} T\Phi_{g^{-1}h_i} \circ b_i u_i\Big). \tag{4.50}$$

Now, in order to derive feedback laws, we first need to linearize the slice dynamics about the fixed point and a zero amplitude control input. For that, we write $z = \tilde{z}_s + w$ and $u_i = 0 + v_i$ and the resulting equations are:

$$\dot{w} = \mathbb{P}_{S_{\tilde{z}_s}}(\hat{A}w + \sum_{i=1}^{m} T\Phi_{g^{-1}h_i} \circ b_i v_i) + O(2), \tag{4.51}$$

where $\hat{A}$ is the same as defined in (4.19). The above equations are nonlinear in the control input h_i and hence not in a form appropriate for using linear control techniques. However, if we choose h_i to be $g \cdot c_i$, where $c_i \in G$ is a constant, then the resulting equations will be linear in w and v. The choice of these constants c_i comes from a phase condition which is explained as follows. We choose c_i such that the control term *does not act in the group direction*. This is the same as a choice that gives a zero contribution of the control term to ξ in (4.50). That is, c_i are given by

$$Y^*(\tilde{z}_s)\,(T\Phi_{c_i} \circ b_i\, u_i) = 0, \qquad \forall u_i \in \mathbb{R}, \qquad i = 1, 2, \ldots, m. \tag{4.52}$$

This choice of c_i means that the group variable g, which depends on ξ, is not affected by the control input and the resulting control acts only on the shape space. The linearized equations (4.51) thus become

$$\dot{w} = \mathbb{P}_{S_{\tilde{z}_s}}(\hat{A}w + \hat{B}v) + O(2), \tag{4.53}$$

where $v = (v_1, v_2, \ldots, v_m)^T$ and $\hat{B}$ is comprised of columns $c_i \cdot b_i$. Equation (4.53) is in the form for linear control design and we can proceed to derive feedback laws for v as described in the previous section.

The amplitude v is chosen such that $(w,\, v)$ minimize a quadratic cost function, which in this case is

$$J[\tilde{z}, u] = \int_0^\infty \big(\, \langle \tilde{z} - \tilde{z}_s, Q(\tilde{z} - \tilde{z}_s)\rangle + \langle u, Ru\rangle \,\big)\, dt, \tag{4.54}$$

where $u = (u_1, u_2, \ldots, u_m)^T$. Q is again equivariant to the action Φ_g and has to satisfy (4.35). But since the action Ψ_g leaves u unchanged, R can be an arbitrary, positive-definite, $m \times m$ matrix. The resulting control law is optimal in the sense that the inputs u_i are chosen such that they minimize the cost (4.54); however, the choice of the other inputs h_i does not come from an optimality criterion, but from an imposed phase condition.

Note that the choice of the control inputs $h_i = g \cdot c_i$ implies that the phase of the actuators differs from the group variable just by a constant. This means that the actuators appear “stationary” in the reduced frame of reference and their “phase-difference" is always constant. We will demonstrate with the help of a numerical example that this choice of the phase h_i, in general, is not the best choice; that is, different phase conditions might lead to cheaper or more efficient controllers.

4.5 Examples

In this section, we illustrate our control methodology with the help of three examples. First, we consider a simple planar, rotationally invariant system and derive feedback laws to stabilize an open-loop unstable limit cycle. Then we consider a physical example, that of stabilizing an inverted pendulum on a cart, which was previously considered in Bloch *et al.* (2000) to illustrate the method of controlled Lagrangians. Finally, we demonstrate the potential of the developed methods to control of fluid flows with symmetry, using a simplified model of flame dynamics and turbulence, namely the Kuramoto-Sivashinsky equation, which is a translationally invariant PDE in one spatial dimension. For this PDE, we derive feedback laws that stabilize unstable traveling waves and present numerical results.

4.5.1 A planar ODE system with rotational symmetry

We consider (4.1) to be a system of ODEs on $\mathcal{M} = \mathbb{R}^2$ with the symmetry group acting on $\mathcal{M}$ being $G = \mathrm{SO}(2)$. Then, for $z \in \mathbb{R}^2$ and $\theta \in S^1$, the group action is $\Phi_\theta(z) = R_\theta z$, where R_θ is rotation through an angle $\theta \in [0, 2\pi)$. Equivariance of (4.1), with no control, implies that $X(R_\theta z) = R_\theta X(z)$. We consider the following particular example, where $z = (x, y)$:

$$\dot{x} = -x - y + x\sqrt{x^2 + y^2}, \tag{4.55}$$

$$\dot{y} = x - y + y\sqrt{x^2 + y^2}. \tag{4.56}$$

In polar coordinates (r, θ), the above equations are:

$$\dot{r} = r^2 - r, \quad \dot{\theta} = 1. \tag{4.57}$$

This system has $r = 1$ as an unstable limit cycle or a relative equilibrium, which we want to stabilize. Note that in polar coordinates, the shape dynamics (r) and the group dynamics (θ) are decoupled. So, a simple control technique is to just ignore the θ-dynamics in (4.57) and add a control term of the form Bu to the r-equation, where the input $u = K(r - 1)$ with K chosen such that $r = 1$ is stable. This control retains the symmetry of the system and stabilizes the relevant relative equilibrium, the limit cycle $r = 1$. Here instead, we work with equations (4.56) in Cartesian coordinates to illustrate our template-based control technique.

We first derive the reduced or slice dynamics of the above system. The infinitesimal generator $\xi_{\mathcal{M}}(z)$ can be obtained from (4.9) by:

$$\xi_{\mathcal{M}}(z) = \left.\frac{d}{ds}\right|_{s=0} R_{\phi(s)} z = \xi \begin{pmatrix} 0 & -1 \\ 1 & 0 \end{pmatrix} z \overset{\text{def}}{=} \xi\, \mathbb{J}\, z, \qquad \phi(0) = 0, \xi = \frac{d\phi}{ds}(s=0), \tag{4.58}$$

where $\xi \mathbb{J} \in \mathfrak{g} = \mathfrak{so}(2)$ is an element of the Lie algebra of G. Comparing with (4.13), we note that $Y(z) = \mathbb{J}z$. Next, we define the slice S_{z_0}. Let the template z_0 be a particular point on the limit cycle $r = 1$, that is $z_0 = (\cos\beta, \sin\beta)$, for some $\beta \in [0, 2\pi)$. Then using (4.15), the slice S_{z_0} is given by

$$-\sin\beta\, x + \cos\beta\, y = 0 \tag{4.59}$$

which is a straight line through the origin and z_0. The slice dynamics can be obtained by writing $z = R_\theta \tilde{z}$, where $\tilde{z} \in S_{z_0}$ and θ is a rotation of z to the line defined by (4.59); see Fig. 4.3. The resulting equations for $\tilde{z}$ are:

$$\dot{\tilde{z}} = X(\tilde{z}) - \xi\, \mathbb{J}\, \tilde{z}, \tag{4.60}$$

where ξ is given by (4.19). Then, we differentiate (4.59) with respect to time and use (4.60) to find an explicit expression for ξ. In this example, we pick $\beta = \tan^{-1}(2)$, and the resulting open loop expression for ξ is

$$\xi = \frac{(3x + 2y) - (2x - y)\sqrt{x^2 + y^2}}{x + 2y}. \tag{4.61}$$

Equations (4.60,4.59) are the reduced or slice dynamics and they form a set of DAEs with two differential and one algebraic equations; the relative equilibrium $r = 1$ is a fixed point $(1/\sqrt{5}, 2/\sqrt{5})$ of these equations.

Equivariant actuation

Consider the closed loop vector field to be of the form (4.32), that is affine in u. Suppose that $u \in \mathcal{U} = \mathbb{R}^2$ and that the action of G on $\mathcal{U}$ is $\Psi_\theta = \Phi_\theta$. Equivariance of $H(z)$ implies that $H(z)R_\theta = R_\theta H(z)$. That is, $H(z)$ is of the form:

$$H(z) = \begin{pmatrix} a(r) & -b(r) \\ b(r) & a(r) \end{pmatrix} \qquad \forall z \in \mathbb{R}^2, \quad r = \sqrt{x^2 + y^2} \tag{4.62}$$

Here, we choose $H(z)$ to be a constant with $a(r) = 2$ and $b(r) = 1$. Letting $\tilde{z} = z_0 + (w_x,\, w_y)$ and $u = 0 + v$, the linearization of the closed loop slice dynamics about the fixed point $z_0 = (1/\sqrt{5}, 2/\sqrt{5})$ is given by (4.19):

$$\dot{w} = \begin{pmatrix} \dot{w}_x \\ \dot{w}_y \end{pmatrix} = \frac{1}{5}\begin{pmatrix} 1 & 2 \\ 2 & 4 \end{pmatrix} \begin{pmatrix} w_x \\ w_y \end{pmatrix} + \frac{1}{5}\begin{pmatrix} 4 & 3 \\ 8 & 6 \end{pmatrix} v. \tag{4.63}$$

By direct calculation, it can be verified that (4.63) has an invariant subspace defined by the constraint (4.59). Now, as in (4.25, 4.26), we write $w = (w_s, w_g)$ and eliminate one of the equations from (4.63). Equation (4.59) is analogous to (4.26)

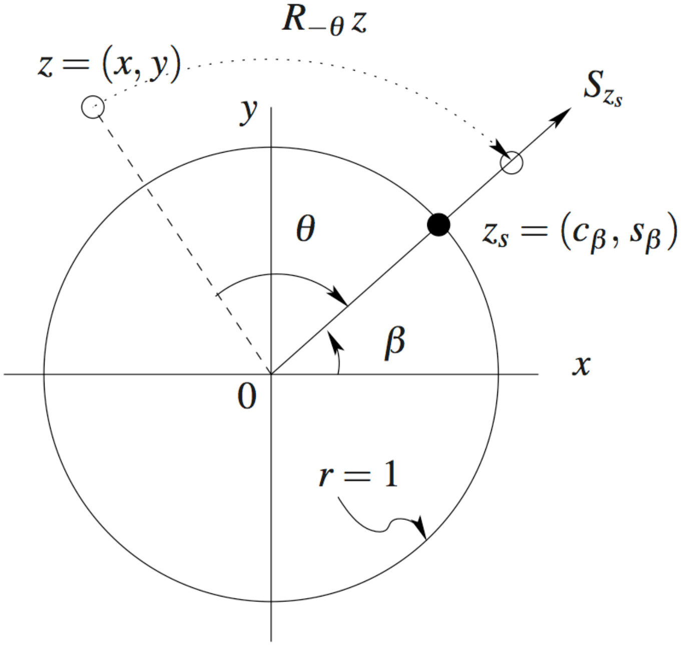

Figure 4.3: Planar rotationally invariant system.

and, for our choice of β, we can either express w_x in terms of w_y or vice-versa. If $\beta=0$, then (4.63) would become $w_y=0$ and we can eliminate only the w_x equation from (4.63); similarly, for $\beta=\pi/2$, we can eliminate only the w_y-equation. We let $w_s=w_x$ and $w_g=w_y$, so that from (4.59) we have $w_g=(\tan\beta)\,w_s=2w_s:=\Lambda\,w_s$. We use this to eliminate the equation for w_g from (4.63) to get

$$\dot{w_s}=w_s+\frac{1}{5}\begin{pmatrix}4 & 3\end{pmatrix}v\overset{\text{def}}{=}A_sw_s+B_sv. \tag{4.64}$$

Now, clearly (4.64) is controllable, as the rank of B_s is 1. This implies that the slice S_{z_0} is a controllable subspace of (4.63).

Optimal control design. Invariance of the cost function (4.37) to the group action imposes a restriction on Q, R, which is the same as that on $H(\tilde{z})$ in (4.62). But since they also have to be symmetric and positive definite, Q, R can only be multiples of I. We choose $Q=R=I$. Then, eliminating w_g from (4.37), the modified cost function is

$$J[w,u]=\int_0^\infty\left((w_s^2+w_g^2)+v^Tv\right)\,dt=\int_0^\infty(5w_s^2+v^Tv)\,dt. \tag{4.65}$$

Thus, the weight in the reduced cost function (4.38) is $\tilde{Q}=5$. The LQR problem to be solved is: find the feedback law $v=\tilde{K}w_s$ such that (w_s,v) solve (4.64) and minimize (4.65). The $1D$ Riccati equation to be solved, as in (4.41) is

$$M^2-2M-5=0\implies M=1+\sqrt{6}. \tag{4.66}$$

Then, $\tilde{K} = R^{-1}B_s M = B_s M$ and $v = \tilde{K} w_s$, where, as shown in (4.42), w_s can be expressed in terms of w as:

$$w_s = \frac{1}{5}\begin{bmatrix}1 & 2\end{bmatrix} w \overset{\text{def}}{=} \Gamma w. \tag{4.67}$$

Finally, the feedback law in terms of w is

$$v = -\frac{1+\sqrt{6}}{25}\begin{pmatrix}4 & 8\\ 3 & 6\end{pmatrix} w \overset{\text{def}}{=} Kw. \tag{4.68}$$

The feedback law in the original framework is given by (4.46), with $\Phi_g = R_\theta$ where $-\theta$ is the angle of rotation to the slice (refer Fig. 4.3). The closed loop system in polar coordinates becomes,

$$\dot{r} = -r + r^2 - \kappa(r-1), \quad \dot{\theta} = 1, \tag{4.69}$$

where $\kappa = 1 + \sqrt{6}$. Thus, the resulting control does not affect the group variables, just the shape variables. This may appear as a convoluted way to design an obvious controller, but it serves to illustrate the mathematical machinery in a transparent example.

Amplitude and phase actuation

We now consider a more general system of the form (4.47) with $m = 1$; that is we have one actuator that is not equivariant but can be rotated about the origin. We consider a controller of the form $R_\alpha B d$, where $d \in \mathbb{R}$ and $B : \mathbb{R} \to \mathbb{R}^2$ (We use the symbol α here, instead of h used in (4.47)). The control inputs are $(d, \alpha) \in \mathcal{U} = \mathbb{R} \times G$ and the action of G on $\mathcal{U}$ is $\Psi_\theta(d, \alpha) = (d, \alpha + \theta)$. If we choose $B = (a(r),\, b(r))^T$ where a, b are defined as in (4.62), then it is easy to see that the resulting control is the same as in the previous section if we identify $u = (u_1, u_2)$ with $(d\cos\alpha, d\sin\alpha)$. However, the choice of the inputs is different in the two cases. In this case, the slice dynamics for (4.47) can be obtained by decomposing $z = R_\theta \tilde{z}$:

$$\dot{\tilde{z}} = X(\tilde{z}) + R_{\alpha-\theta} B d - \xi \mathbb{J}\tilde{z}, \tag{4.70}$$

where ξ is given by

$$\xi = \frac{\langle X(\tilde{z}) + R_{\alpha-\theta} B d, \mathbb{J}\tilde{z}_s\rangle}{\langle \mathbb{J}\tilde{z}, \mathbb{J}\tilde{z}_s\rangle}. \tag{4.71}$$

As discussed in section 4.4.2, we choose α such that the control term does not affect ξ. That is, from (4.71), we choose α such that

$$\langle R_{\alpha-\theta} B d, \mathbb{J}\tilde{z}_s\rangle = 0 \qquad \forall d \in \mathbb{R}. \tag{4.72}$$

With the given form of $B = (a,\, b)^T$, and again choosing $a = 2$ and $b = 1$, this simplifies to:

$$\alpha - \theta = \beta - \tan^{-1}(-b/a) = \tan^{-1}(3/4). \tag{4.73}$$

Using (4.73) in (4.70) and expressing $\tilde{z} = \tilde{z}_s + w$, we get the linearized slice dynamics:

$$\dot{w} = \begin{pmatrix} \dot{w}_x \\ \dot{w}_y \end{pmatrix} = \frac{1}{5} \begin{pmatrix} 1 & 2 \\ 2 & 4 \end{pmatrix} \begin{pmatrix} w_x \\ w_y \end{pmatrix} + \begin{pmatrix} 1 \\ 2 \end{pmatrix} d. \tag{4.74}$$

As in (4.63, 4.64), we use the equation of the slice (4.59) to eliminate the equation for w_y. That is, we substitute $w_y = 2\, w_x$ in (4.74) to get

$$\dot{w}_x = w_x + d \overset{\text{def}}{=} A_s w_x + B_s d. \tag{4.75}$$

Now, we can derive an optimal feedback law for (4.75). The matrices Q and R in the cost function are chosen to be equal to 2 and 1-dimensional identities respectively. The Riccati equation to be solved in this case turns out to be the same as (4.66). Thus, the feedback law for d is

$$\epsilon = -B_s M w_x = -B_s M \Gamma w \qquad \text{using (4.67)} \tag{4.76}$$

$$= \frac{1+\sqrt{6}}{5} \begin{pmatrix} 2 & 1 \end{pmatrix} w \overset{\text{def}}{=} K w. \tag{4.77}$$

Finally, the feedback law in the original frame is given by

$$d = K(R_{-\theta} z - z_s). \tag{4.78}$$

Thus, the inputs d and α are given by (4.78) and (4.73) respectively. With this control the closed loop equations in polar coordinates happen to be the same as (4.69). Thus, for this example, both approaches yield the same feedback laws. This is not the case in general, though, as illustrated in a following section.

4.5.2 Inverted pendulum on a cart

We now consider a physical example: that of stabilizing an inverted pendulum on a cart. We will also compare our controller with that obtained in Bloch *et al.* (2000) using the method of controlled Lagrangians.

We first derive the equations of motion. Let s be the cart position and ϕ be the pendulum angle measured clockwise from the vertical axis; the Lagrangian of the system is:

$$L(\phi, s, \dot{\phi}, \dot{s}) = \frac{1}{2}(m_1 l^2 \dot{\phi}^2 + 2 m_1 l \cos\phi \dot{s}\dot{\phi} + (m_1 + m_2)\dot{s}^2) - m_1 g l \cos\phi, \tag{4.79}$$

where m_1 and m_2 are the pendulum and the cart masses, and l is the pendulum length. As the Lagrangian is independent of s, the equations of motion are invariant to translations of the cart. The momenta conjugate to ϕ and s are

$$p_\phi = m_1 l^2 \dot{\phi} + m_1 l \cos\phi \dot{s} \quad \text{and} \tag{4.80}$$

$$p_s = (m_1 + m_2)\dot{s} + m_1 l \cos\phi \dot{\phi}, \tag{4.81}$$

and the equations of motion are

$$\begin{pmatrix} \dot\phi \\ \dot s \\ \dot p_\phi \\ \dot p_s \end{pmatrix} = \begin{pmatrix} \frac{\gamma p_\phi - \beta\cos\phi p_s}{\alpha\gamma - \beta^2\cos^2\phi} \\ \frac{\alpha p_s - \beta\cos\phi p_\phi}{\alpha\gamma - \beta^2\cos^2\phi} \\ -D\sin\phi - \beta\sin\phi\dot s\dot\phi \\ 0 \end{pmatrix}, \tag{4.82}$$

where $\alpha = m_1 l^2$, $\beta = m_1 l$, $\gamma = m_1 + m_2$, and $D = -m_1 g l$. Define the state as $z = (\phi,\, s,\, p_\phi,\, p_s)$, $z \in M$, where we think of M as being $\mathbb{R}^4$. (Note that actually $z \in S^1 \times \mathbb{R}^3$; however, as our control objective is only to achieve *local* stabilization of relative equilibria, it suffices to use a local chart on M). The symmetry group G acting on M is $(\mathbb{R}, +)$, corresponding to translations in s. The relative equilibria that we attempt to stabilize are $\phi = \dot\phi = 0$ and $\dot s = v$, a constant, which correspond to inverted pendulum on a cart moving with a constant velocity v.

We now define the slice and derive the slice dynamics. The infinitesimal generator is $\xi_M(z) = \xi(0, 1, 0, 0)$, where $\xi \in \mathbb{R} = \mathfrak{g}$, the Lie algebra of G. If we choose the template to be the origin, the slice is defined by the set $\{\tilde z \mid \langle \tilde z, \eta_M(\tilde z)\rangle = 0, \forall \eta \in \mathbb{R}\}$, which is the set $s = 0$. Then, the slice dynamics are given by subtracting $\xi_M(\tilde z)$ from (4.82) and imposing the constraint $s = 0$. It can be easily verified that the equivalent slice dynamics are $\dot s = 0$, with the equations in the other variables remaining unchanged. Thus, the state-space realization of the slice dynamics is obtained by just ignoring the s-equation from (4.82). The template-based method seems trivial here as the shape and the group spaces are already decoupled. This is comparable with the previous example of a planar rotational system. As we saw there, when written in polar coordinates, the group space θ and the shape space r were also decoupled. In general, such a decomposition might not always be possible, as in the same example written in Cartesian coordinates; the template-based reduction is non-trivial and useful for such cases. The template-based control design for the inverted pendulum is based on the linearization of the remaining three equations about the origin. Here, we define a quadratic cost function in terms of the reduced state (ϕ, p_ϕ, p_s) and the input u and use LQR to find the gain $\tilde K$ that stabilizes the origin.

In order to compare with Bloch *et al.* (2000), we consider a control input only in the direction of the cart, that is, we consider a control term of the form $(0, 0, 0, u)$. Thus, $u \in U = \mathbb{R}$ and we assume that the group action leaves this input unchanged, i.e., u is independent of s. We demonstrate our results using some specific numerical values, same as those used in Bloch *et al.* (2000): $m = 0.14$, $M = 0.44$, $l = 0.215$. In particular, we attempt to stabilize the inverted pendulum on a stationary cart ($v = 0$). The eigenvalues of the linearization of the reduced uncontrolled system about this equilibrium are $(\pm 7.751, 0)$ and so the equilibrium is unstable. The eigenvalues of the linearization of the reduced closed loop system (4.28) are tabulated in table 4.1 along with the feedback gains $\tilde K$ defining the feedback law (4.43) for different weights in the cost function (4.38). Note that as K is increased, the eigenvalues approach the values corresponding to the minimum energy control, $(-7.751, -7.751, 0)$.

$\widetilde{Q}$	R	Gain, $\tilde{K}$	closed loop eigenvalues
diag(1,0,10)	10	(12.84, 337.35, -16.51)	(-0.998, -7.755 ± 0.22i)
diag(1,0,10)	100	(11.83, 310.92, -15.82)	(-0.316, -7.752 ± 0.07i)
diag(1,0,10)	1000	(11.52, 302.60, -15.60)	(-0.100, -7.752 ± 0.02i)

Table 4.1: LQR gains. Here, "diag" implies a diagonal matrix with its diagonal entries in parentheses.

Now, the control law derived in Bloch *et al.* (2000) is

$$u = \frac{\kappa\beta\sin\phi(\alpha\dot{\phi}^2 + \cos\phi D) - c\big(\alpha - \frac{\beta^2}{\gamma}\cos^2\phi\big)\big((\lambda(\kappa+1)+1)\beta\cos\phi\dot{\phi} + \lambda\gamma(\dot{s} - v)\big)}{\alpha - \frac{\beta^2}{\gamma}(1+\kappa)\cos^2\phi} \tag{4.83}$$

where, κ, c, and λ are the control gains. For numerical comparison, we use the same control gains as in Bloch *et al.* (2000): $\kappa = 135$, $\lambda = 0.01$, and $c = 50$. The linearization of (4.83) about the relative equilibrium can be written in the form $u = \tilde{K}w$ and the feedback gain thus obtained is $\tilde{K} = (5.819, 17.17, -0.879)$. The resulting closed loop eigenvalues are $(-0.570, -0.155 \pm 1.11i)$. These values can be compared with those in table 4.1. We see that the control gains resulting from the controlled Lagrangians method are much smaller than those from the template-based method. We also compare the performances using Matlab simulations. Fig. 4.4 shows the time histories of the pendulum angle, the cart position, and the control input; the control gain being the second listed in table 4.1. The initial angle is $\phi(0) = 0.5$, the initial cart position is at the origin, and the initial pendulum and cart velocities are zero. With both methods, the pendulum comes to rest at the upright position $\phi = 0$, while the cart moves a considerable distance before coming to rest. However, using the controlled Lagrangian method, there are considerably more oscillations in the transient approach to the equilibrium as compared to that using the template-based approach and even though the gains are smaller, the overall actuator energy is greater. A key advantage of the controlled Lagrangian method is that the domain of stability can be defined, whereas the template based method can only ensure local stability.

4.5.3 The Kuramoto-Sivashinsky equation: a spatially distributed example

Here, we illustrate our control methodology using a less simplistic example. We consider a dissipative PDE, the Kuramoto-Sivashinsky (K-S) equation

$$z_t = -zz_x - z_{xx} - \nu z_{xxxx}, \qquad x \in [0, 2\pi), \tag{4.84}$$

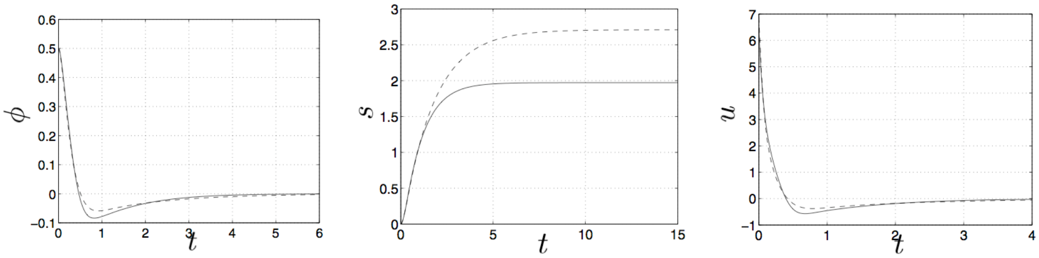

Figure 4.4: Comparison of template-based LQR (solid line) and the controlled Lagrangian method (dashed line).

in one spatial dimension and with periodic boundary conditions. That is, $z \in \mathcal{M} = L^2([0, 2\pi])$, the space of 2π-periodic, square integrable functions. This system is translationally invariant, that is equation (4.84) is equivariant under the action of the additive group $G = (\mathbb{R}, +)$. The group action is given by $\Phi_g(z(x)) = z(x + g)$ and $T\Phi_g = \Phi_g$. The infinitesimal generator obtained using (4.9) is

$$\xi_{\mathcal{M}}(z) = \xi z_x. \tag{4.85}$$

Physically, ξ is the speed of travel in the group direction.

The K-S equation exhibits complex dynamics for different values of the viscous parameter ν. Various analytical and numerical studies have been performed on the equation; for example, see Kevrekidis *et al.* (1990), Armbruster *et al.* (1988) and the references therein. Here, we restrict our attention to two different values of ν, for which we try to stabilize different types of unstable relative equilibria: steady states, and traveling waves. For $\nu = 4/20$, we will try to stabilize an unstable open loop traveling wave (actually, the equation possesses two of them, one left-traveling and one reflection-symmetric right-traveling one); for $\nu = 4/15$, we will try to stabilize a ring of open-loop unstable spatially nonuniform steady states. Fig. 4.5 shows numerical results demonstrating that the transients are eventually attracted to a heteroclinic loop at $\nu = 4/20$ and to a stable traveling wave at $\nu = 4/15$; see Kevrekidis *et al.* (1990). Our goal is to find feedback laws that stabilize members of these two types of representative solution families.

We base our control design on a finite dimensional ODE approximation of (4.84) obtained using a Galerkin projection onto the 2π-periodic Fourier modes. Such an approach of control design for PDEs is very common, (for example, see Armaou & Christofides (2000) and the references therein) and is justified by the existence of a low-dimensional inertial manifold (Jolly *et al.*, 1990; Temam, 1988; Nicolaenko *et al.*, 1989). We note that the feedback control problem of the K-S equation with periodic boundary conditions was considered before in Armaou & Christofides (2000), Lou & Christofides (2003), and Lee & Tran (2005); the focus in these works was on stabilization of the zero solution.

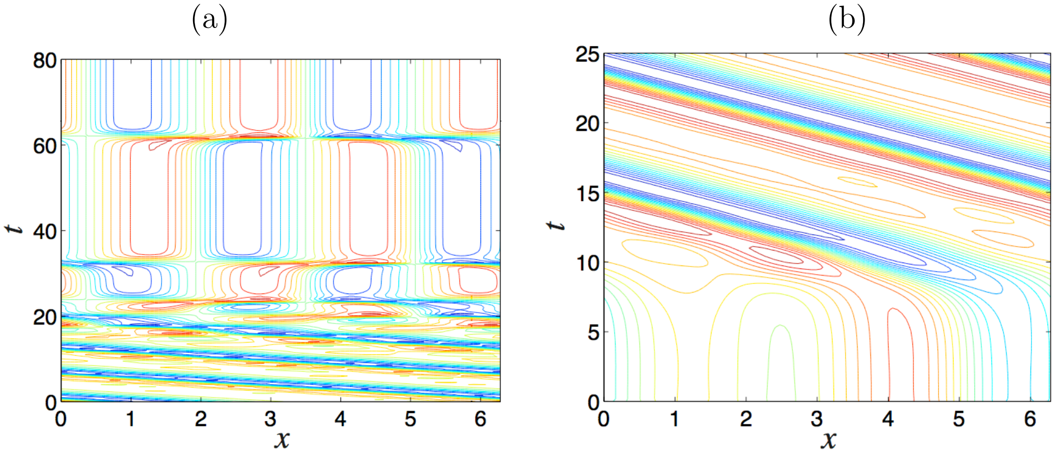

Figure 4.5: Plot (a): $\nu = 4/20$. A contour plot of $z(x,t)$ showing transients which, initialized in the vicinity of an unstable traveling wave approach asymptotically a persistent heteroclinic loop. Plot (b): $\nu = 4/15$. A contour plot showing transients which, initialized in the vicinity of a ring of unstable steady states, asymptotically approach a stable traveling wave.

First, we obtain a finite-dimensional ODE approximation of (4.84). For that, we decompose $z(x,t)$ into its Fourier modes:

$$z(x,t) = \sum_{k=-\infty}^{\infty} c_k(t) \exp(ikx), \qquad c_k = a_k + i\, b_k, \quad c_{-k} = c_k^*. \tag{4.86}$$

Here, we consider only solutions with a zero spatial mean; that is $c_0 = 0$. Substituting (4.86) in (4.84), performing a Galerkin projection onto the Fourier modes, and truncating at an order n, results in a finite set of ODEs for c_k. The action $\Phi_g(z(x))$ translates to an action on the Fourier coefficients c_k as $\Phi_g(c_k) = e^{ikg}c_k$, $k = 0, 1, \ldots, n$. We consider two different controllers, belonging to the class of controllers described in sections 4.4.1 and 4.4.2. In the first case, the closed loop system is affine in the control input and the actuation is equivariant:

$$\dot{z} = X(z) + \sum_{k=1}^{m} u_k(t) \exp(ikx) \overset{\text{def}}{=} X(z) + \sum_{k=1}^{m} u_k(t) b_k(x), \tag{4.87}$$

The actuators $b_k(x)$ are considered to be the first m Fourier modes, and the control inputs essentially prescribe the amplitudes of these modes. The action Ψ_g on the control inputs u_k is the same as that of Φ_g on the Fourier coefficients c_k.

In the second case, we consider arbitrarily shaped actuators and assume that the actuator can be translated by any amount in space. The closed loop system for this case is

$$\dot{z} = X(z) + \sum_{k=1}^{m} u_k(t) b_k(x + h_k). \tag{4.88}$$

Physically, h_k and u_k are the inputs that specify the phase and amplitude of the actuator b_k respectively. The group action on the control inputs is $\Psi_g : (u_k, h_k) \rightarrow (u_k, h_k + g), k = 1, 2, \ldots, m$.

If $\tilde{z}_s$ is the template, the slice $S_{\tilde{z}_s}$ is defined using (4.10, 4.85) to be the set of $\tilde{z}$ such that

$$\langle \tilde{z} - \tilde{z}_s, \tilde{z}_s' \rangle = 0 \tag{4.89}$$

where $\langle \cdot, \cdot \rangle$ is the L^2-inner product and prime denotes differentiation with respect to x. Now, if we denote the right hand sides of (4.87, 4.88) as $X(z) + U$, we can formally write the slice dynamics of these equations as:

$$\dot{\tilde{z}} = X(\tilde{z}) + \widetilde{U} - \xi \tilde{z}_x \tag{4.90}$$

where $\tilde{z}(x,t) = z(x - g, t)$ lies in the slice $S_{\tilde{z}_s}$. Similarly, $\widetilde{U}$ is the control term U expressed in the traveling frame. The speed ξ in (4.90), analogous to (4.17), is

$$\begin{aligned} \xi = \frac{\langle X(\tilde{z}) + \widetilde{U}, \tilde{z}_s' \rangle}{\langle \tilde{z}', \tilde{z}_s' \rangle} &= \frac{\langle X(\tilde{z}), \tilde{z}_s' \rangle}{\langle \tilde{z}', \tilde{z}_s' \rangle} + \frac{\langle \widetilde{U}, \tilde{z}_s' \rangle}{\langle \tilde{z}', \tilde{z}_s' \rangle} \\ &\overset{\text{def}}{=} \xi_o + \xi_c. \end{aligned} \tag{4.91}$$

Thus, ξ is the closed loop speed, and ξ_o and ξ_c are the contributions of the open-loop vector field and the control inputs to it. The assumption made in equation (4.17) in section 4.2.1 that $Y^*(\tilde{z}_s)Y(z)$ is invertible is the same as assuming that the denominator $\langle \tilde{z}', \tilde{z}_s' \rangle$ in (4.91) is non-zero.

Before presenting the results of our control design, we make a remark. In order to obtain the feedback laws, we choose the template function to be the fixed point of the slice dynamics itself. Clearly, we first need to calculate this fixed point, for which we proceed as follows. We choose an arbitrary template function z_0 and use Newton's method to find the fixed point of the slice dynamics thus obtained. Instead of finding the fixed point of the DAE system (4.8, 4.10), we substitute for ξ from (4.17) into (4.8) and find the fixed point of the resulting equivalent differential system. Note that the Jacobian at each step of these Newton iterations will be singular because of translational invariance. However, we have an additional constraint (4.10) that each iteration should belong to the slice S_{z_0}. We use this constraint to reduce the number of unknowns in the Newton iterations by one. This constraint is similar to the pinning conditions commonly used in the computation of traveling waves or limit cycles, or equivalently it is similar to the phase condition used in Doedel *et al.* (1991) to tackle the issue of a singular Jacobian while computing periodic solutions of ODEs. Then, we use the fixed point $\tilde{z}_s$ thus obtained as a new template to derive feedback laws.

Now we present some results for the two different control methodologies to illustrate their differences. First, we describe the numerical scheme for integrating the closed loop equations.

Numerical scheme

Here we outline the numerical scheme used to integrate the close loop K-S equation (4.87) for the case of equivariant actuation; the scheme is very similar for the amplitude-phase control case. We first write the closed loop K-S equation (4.87) as

$$\dot{z} = L(z) + N(z) + \sum_{i=1}^{M} b_i(x)\, u_i, \tag{4.92}$$

where, the inputs are given by

$$u_i = h \cdot K_i(h^{-1} \cdot z - z_s) \tag{4.93}$$

and h is given by

$$\langle h^{-1} \cdot z - z_s, z_s' \rangle = 0. \tag{4.94}$$

Here, $L(z)$ and $N(z)$ are the linear and nonlinear terms of the open loop vector field. The time-stepping scheme uses the implicit trapezoidal rule for the linear terms and the explicit Adams-Bashforth for the nonlinear terms:

$$\frac{z_{n+1} - z_n}{\Delta t} = \frac{1}{2}(L(z_{n+1}) + L(z_n)) + \frac{1}{2}(3N(z_n) - N(z_{n-1})) + \sum_{i=1}^{M} b_i(x) \frac{u_i^n + u_i^{n+1}}{2}, \tag{4.95}$$

where,

$$u_i^n = h_n \cdot K_i(h_n^{-1} \cdot z_n - z_s) \tag{4.96}$$

and h_{n+1} given by

$$\langle h_{n+1}^{-1} \cdot z_{n+1} - z_s, z_s' \rangle = 0. \tag{4.97}$$

Equations (4.95, 4.96, 4.97) are solved iteratively for h_{n+1} and z_{n+1}.

Stabilization of traveling waves

First, we consider $\nu = 4/20$ and stabilize unstable traveling waves. We consider the closed loop equation to be (4.87) (where the actuator is equivariant) and the actuator to be simply the first Fourier mode; that is, $m = 1$ and the control term is $u_1 e^{ix}$. We derive a feedback law that minimizes the cost function (4.37). Unless specified otherwise, here and in what follows, the weight matrices Q and R in the cost are chosen to be the identity. In order to derive the feedback law, we need to evaluate various terms in the linearized slice dynamics (4.19), which we do numerically. The controllability tests mentioned in section 4.3.1 are satisfied in this case. The resulting LQR problem is $(2n-1)$-dimensional and is solved using standard Matlab routines. The results are presented in figures 4.6 and 4.7. As shown in Fig. 4.6(b), the eigenvalues of the linearized open-loop slice dynamics include a complex conjugate pair in the right half complex plane. Both the open and closed loop cases have one eigenvalue at the origin, which corresponds to translational invariance. The initial condition, which is set to be a perturbation of the steady shape of the traveling wave, is shown in Fig. 4.6(a). As shown in Fig. 4.7(b), the control is turned on at $t = 15$. Since the traveling wave is unstable, this causes the perturbations to grow and as seen in Fig. 4.6(c), the residual $\|\tilde{z} - \tilde{z}_s\|_2$ initially grows away from 0; once the control is turned on, it starts to decay. It asymptotically approaches zero, which implies convergence to the correct open loop shape of the traveling wave. Fig. 4.6(d) shows the evolution of the closed loop speed ξ as well as the contribution of the control input ξ_c to it. This contribution is initially non-zero, which means that the optimal control has a non-zero component in the group direction. However, as the dynamics approach the right shape, ξ_c goes to zero asymptotically. This means that the dynamics approach the correct open loop speed of the traveling wave. Thus, the controller stabilizes the traveling wave to the right shape and the right speed. Fig. 4.7(e) is a 3-D plot of the spatiotemporal evolution of $z(x,t)$ and shows convergence to the traveling wave. The input term can also be written as $a \sin(x + \phi)$, where ϕ and a are the equivalent phase and amplitude; these are plotted in Fig. 4.7(c,d) and will be used for comparison with the next case.

Now, we consider the closed loop equations of the form (4.88), where the actuator is not equivariant but can be translated in the group direction, that is, along the domain $[0, 2\pi]$. We first consider the control term to be $u \sin(x + \alpha)$, with the inputs being u and α. The phase α is chosen such that the control does not act in the group direction, that is $\xi_c = 0$. The other input u is then chosen such that the cost function (4.54) is minimized. The results are presented in Fig. 4.8. The initial condition is the same as that considered in the previous case and the control is again turned on at $t = 15$. Fig. 4.8(b) shows that ξ_c indeed stays zero, which confirms that the resulting control acts only on the shape space. Fig. 4.8(a,b) show convergence to the right shape and speed of the traveling wave. Fig. 4.8(c) is a plot of the control input u, and Fig. 4.8(d) is a plot of the amount of translation $g(t)$ that makes $\tilde{z}(x,t) = z(x - g, t)$ to lie in the slice $S_{\tilde{z}_s}$. Now, the other input $\alpha = g(t) + c$; that is, it differs from the phase of $z(x,t)$ by a constant c chosen to impose the condition $\xi_c = 0$.

We note that the range of possible actuation for the two cases considered so far is actually identical, but the two cases differ in the way the control inputs appear and in the selection of the feedback laws. In the first case, the inputs are the amplitudes of $\sin(x)$ and $\cos(x)$, both of which are chosen such that a given cost function is minimized. In the second case, the inputs are the amplitude and phase of $\sin(x)$. Here, the phase is chosen by imposing a different type of constraint; given this constraint on the phase, the amplitude is chosen using LQR. We can now compare the inputs in the second case with the equivalent phase and amplitude of the inputs in the first case plotted in Fig. 4.7(c,d). We see that, unlike in the second case, the phase ϕ in the first case does not differ from g by a constant. So, the actuator is

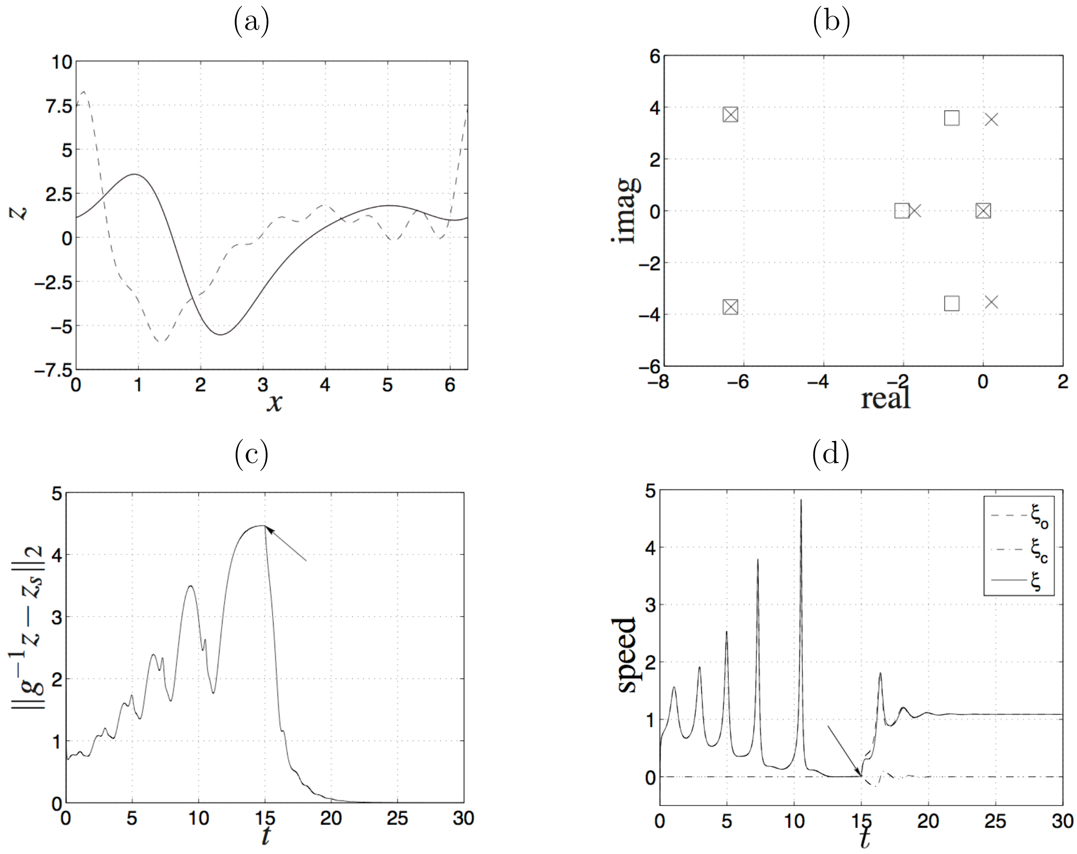

Figure 4.6: Stabilized traveling wave solution for $\nu = 4/20$ with the control term $u_1 \sin x + u_2 \cos x$, where u_1 and u_2 are the control inputs. Control is turned on at $t = 15$, as indicated by the arrows. Plot (a) shows the fixed point $\tilde{z}_s$ of the slice dynamics (solid line) and the initial condition of the closed loop equations (dashed line). Plot (b) shows the open and closed loop eigenvalues (in '×' and '□') of the linearized slice dynamics. Plot (c) shows that the L^2-error $\|\tilde{z} - \tilde{z}_s\|_2$ decays to zero. Plot (d) shows the the closed loop speed ξ, and the contributions of the open loop vector field (ξ_o) and the control term (ξ_c) to it.

not stationary in the traveling or symmetry reduced frame of reference, which is also reflected in the fact that the control has a non-zero component in the group direction. Since the controller in the second case results in no actuation in the group direction, it implies that the choice of phase in the second case is sub-optimal.

The advantage of the second procedure is that it allows a broader class of actuators, whereas in the first case we are restricted to the Fourier modes for actuation. We illustrate this advantage as follows. As is common practice in control of PDEs (Hagen & Mezić, 2003; Lou & Christofides, 2003; Dubljevic *et al.*, 2004), we consider an actuator that has finite support. Physically, such actuators could be injectors on the circumference of a compressor (Hagen & Mezić, 2003), a laser beam for temperature control of catalytic surfaces, or an array of actuators for flow control (references in Dubljevic *et al.* (2004)). As shown in Fig. 4.9(a), we approximate this actuator by a narrow Gaussian. This actuator is not translationally invariant, hence

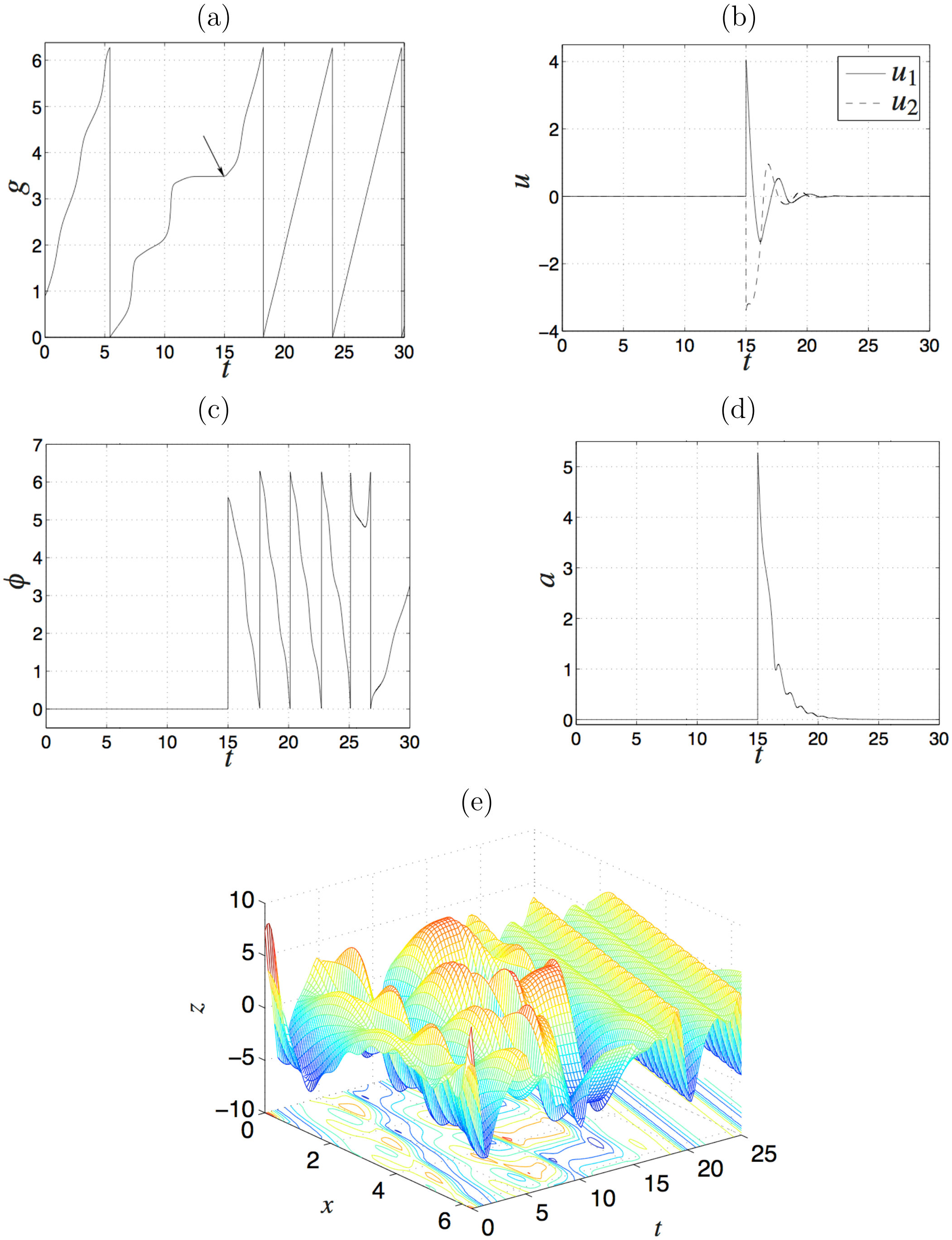

Figure 4.7: Plots for the same case as considered in Fig. 4.6. Plot (a) is a plot of g vs. t where $g(t)$ (modulo 2π) is the amount of translation that makes $z(x,t)$ lie on the slice $S_{\tilde{z}_s}$. The straight line portion represents a wave traveling at a constant speed. Plot (b) shows the control inputs u_1 and u_2, while plots (c) and (d) show the equivalent phase ϕ and amplitude a: $a\sin(x+\phi) = u_1\sin(x) + u_2\cos(x)$. Plot (e) is a 3-D plot of the spatiotemporal evolution of $z(x,t)$.

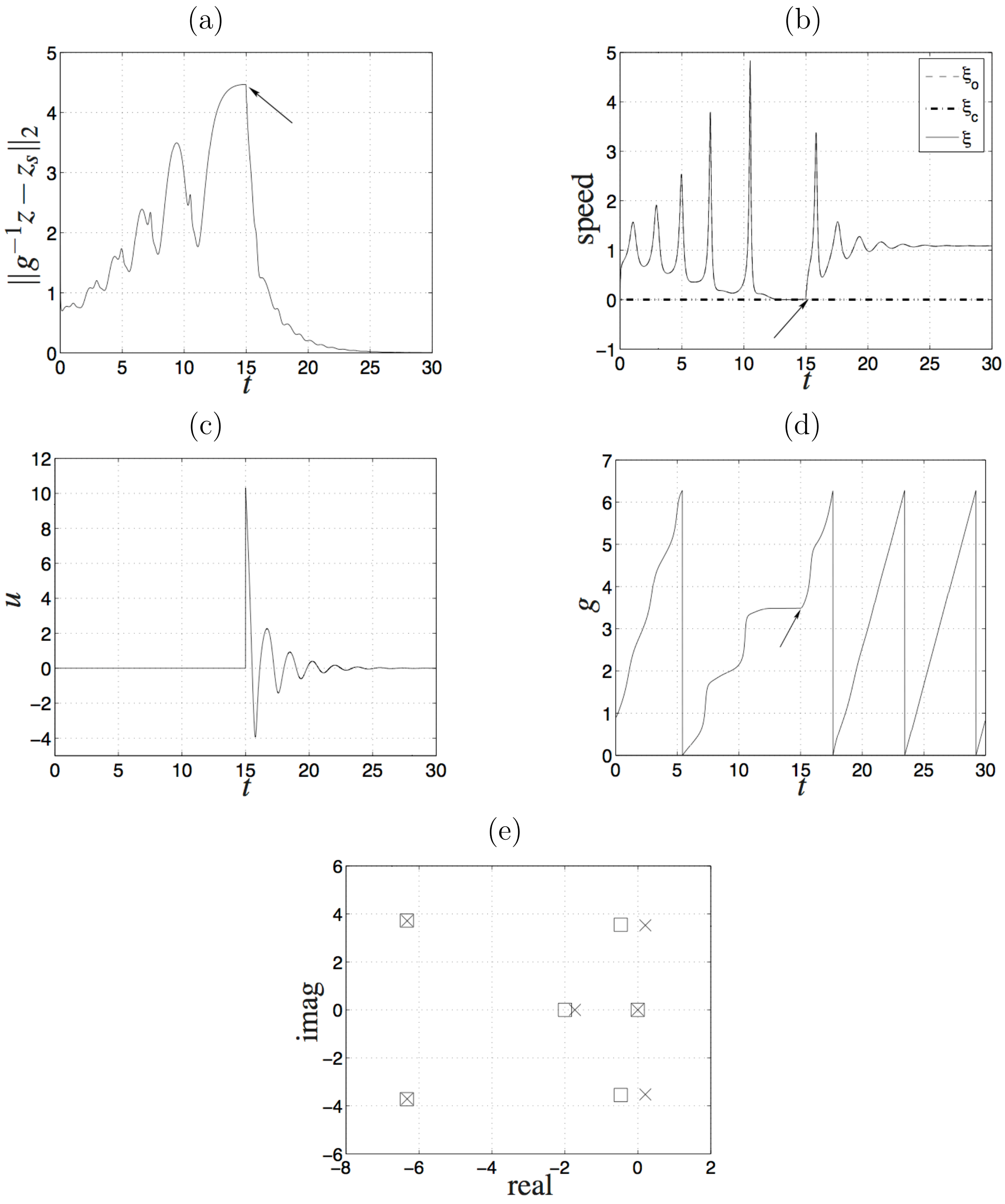

Figure 4.8: $\nu = 4/20$. Plots analogous to those in figures 4.6 and 4.7. The control term is $u_1 \sin(x+\alpha)$, and the inputs are u_1 and α. Again, the control is turned on at $t = 15$, as indicated by the arrows. In plot (b), the solid and dashed lines coincide.

we have to resort to the second control methodology. The results are presented in Fig. 4.9. The initial condition is shown in Fig. 4.9(b), and the rest of the plots show convergence to the correct traveling wave. In the plots of the residual, the control input, and the speed, we observe extensive oscillations in the transient approach to the steady state. This implies insufficient damping which is also evident from the proximity of the two closed loop eigenvalues to the imaginary axis in Fig. 4.9(d). We tried some simulations with the phase α still given as $g(t) + c$, where c is a constant. But now instead of being chosen from the criterion $\xi_c = 0$, c was varied arbitrarily. We observed that for certain values of c, the performance of the resulting controller was better: considerably fewer oscillations in the transients were observed as compared to those in Fig. 4.9. It would be interesting to pursue optimal choices of c, but we leave this for future studies.

Stabilization of steady states

Next, we consider the case of $\nu = 4/15$ and attempt to stabilize the unstable, spatially nonuniform steady state of the KS. The linearization of the open loop dynamics about such steady states has one one eigenvalue in the right-half of the complex plane; see Fig. 4.10(b). Note that, because of translational invariance, there exists a one-parameter family of steady states given by a translation of $\tilde{z}_s$ (which is a fixed point of the slice dynamics). Our control procedure retains this invariance; that is, the initial conditions that are simple translations of each other result in trajectories that are the same translations of each other. We consider the closed loop equation to be (4.87) and again, the actuator is the first Fourier mode e^{ix}. The controllability tests are satisfied. The closed loop results are presented in Fig. 4.10 and Fig. 4.11. The initial condition, shown in Fig. 4.10(a), is set to be a random perturbation of $\tilde{z}_s$. Here too, Fig. 4.10(c) shows convergence to the right shape. Fig. 4.10(d) shows that the speeds ξ and ξ_c approach zero, implying convergence to a steady state. Non-zero transients for ξ_c show that here too, the optimal control has a non-zero component in the group direction.

Fig. 4.12(b) shows the evolution of g, which represents the shift of $z(x,t)$ that aligns it with the slice $S_{\tilde{z}_s}$, for different initial conditions. Fig. 4.12(a) shows the initial conditions in the corresponding line styles. All the plots converge to a constant value of g, which means convergence to another, but different, translation of $\tilde{z}_s$. Furthermore, the initial conditions in dots is simply a translation by two units of that in dashes. Correspondingly, the resulting trajectories of g are also simply translations of each other by the same two units.

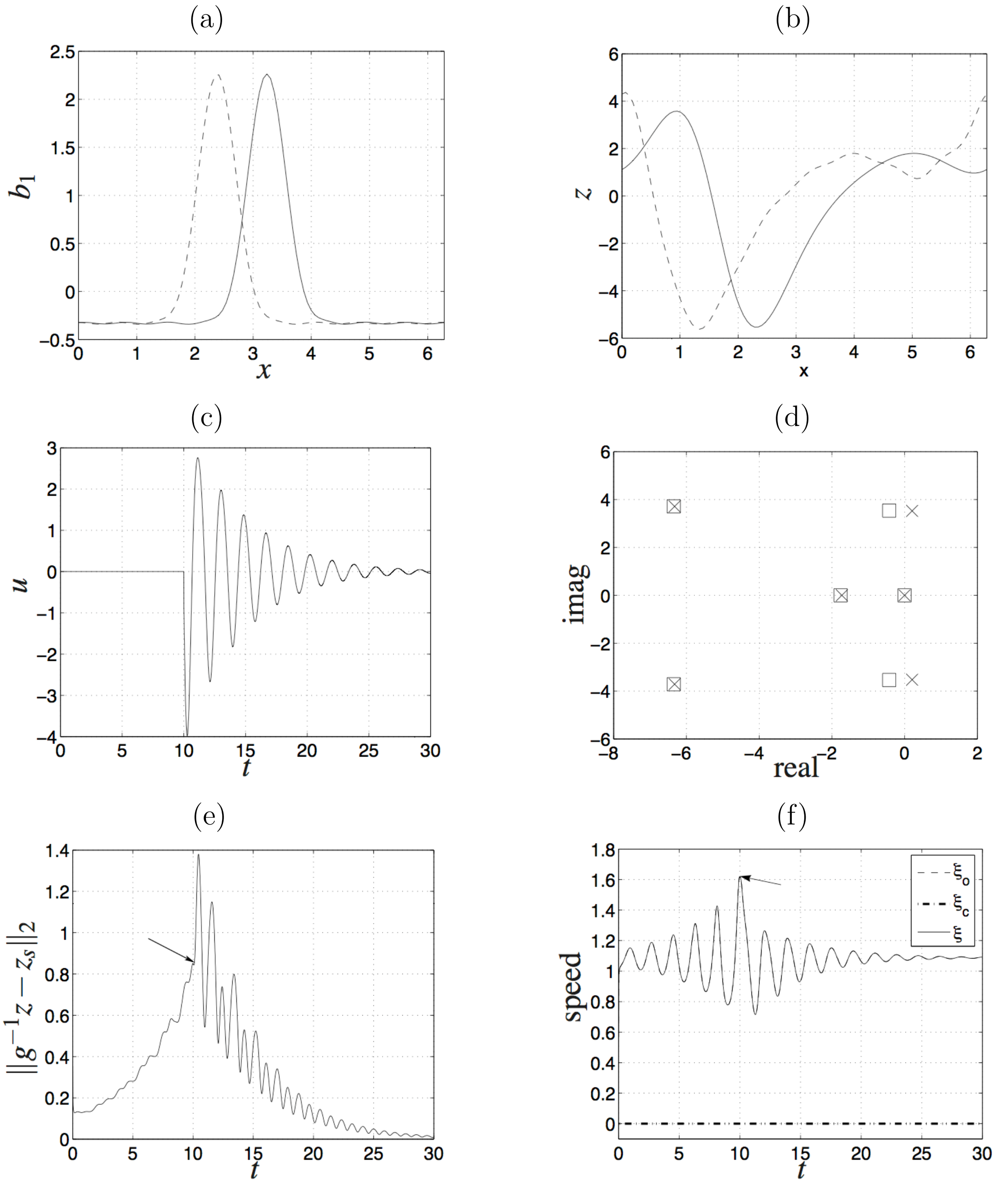

(a) (b) (c) (d) (e) (f)

Figure 4.9: $\nu = 4/20$. Plots analogous to those in figures 4.6 and 4.7, except for plot (a). The control term is $u\,b(x+\alpha)$, where $b(x)$ is the actuator, shown in plot (a) with a solid line, and u and α are the control inputs. The dashed line in plot (a) shows the actuator in the traveling frame of reference, where it appears stationary. Plot (b) shows the fixed point $\tilde{z}_s$ of the slice dynamics (solid line) and the initial condition of the closed loop equations (dashed line).

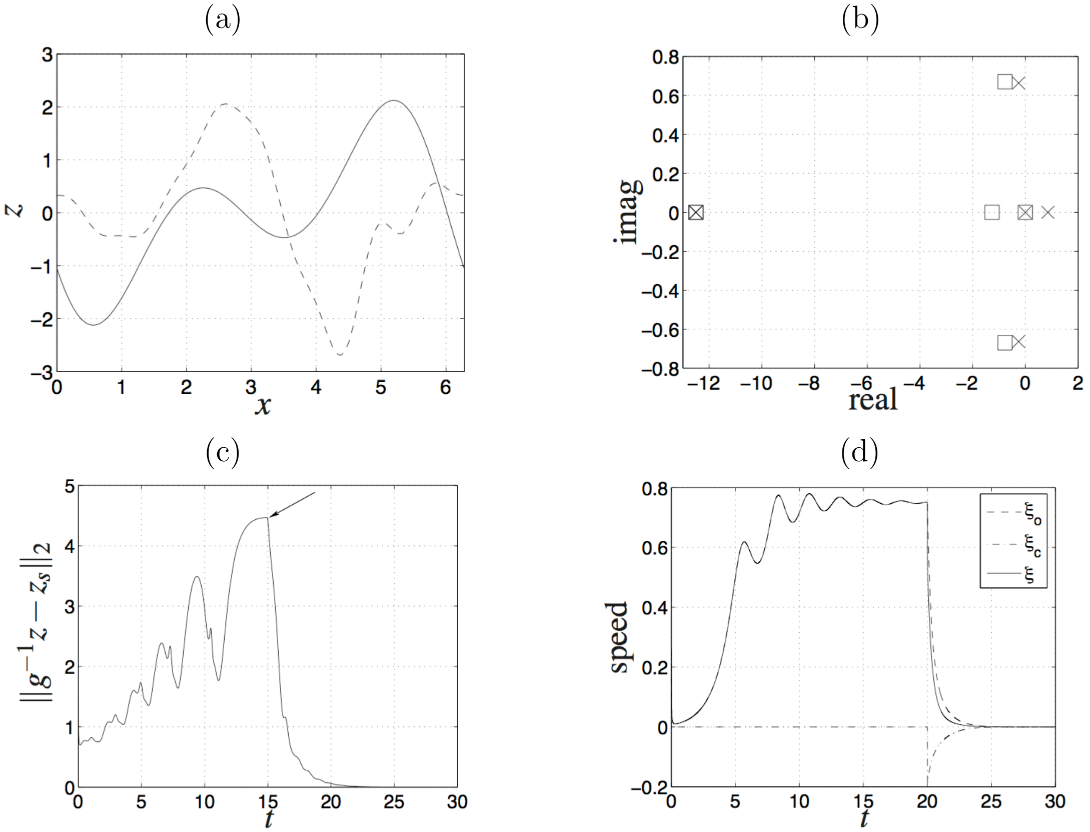

Figure 4.10: Stabilized steady state solution for $\nu = 4/15$ with the control term $u_1 \sin x + u_2 \cos x$, where u_1 and u_2 are the control inputs. Plots analogous to those in Fig. 4.6. Control is turned on at $t = 20$ (indicated by an arrow), where the state is in the vicinity of the stable traveling wave. Plot (a) shows the fixed point $\tilde{z}_s$ of the slice dynamics (solid line) and the initial condition of the closed loop equations (dashed line).

4.6 Summary

We have presented two approaches to stabilizing relative equilibria of general nonlinear systems with symmetry, using the template-based technique of Rowley *et al.* (2003) and Rowley & Marsden (2000) to obtain equations in a symmetry-reduced frame. As the relative equilibria are fixed points in this frame, simple tools from linear systems theory could be used to derive feedback laws. The reduced dynamics have an invariant subspace orthogonal to the group orbit through the chosen template, and it is this subspace that we require to be controllable.

We considered two types of actuators. In the first case, we assumed the actuation to be equivariant under the symmetry group action. For this case, we used LQR to derive locally optimal feedback laws and demonstrated with a numerical example that, in general, these control laws have a component in both the group and the shape directions. In the second case, we considered arbitrary actuators, but assumed

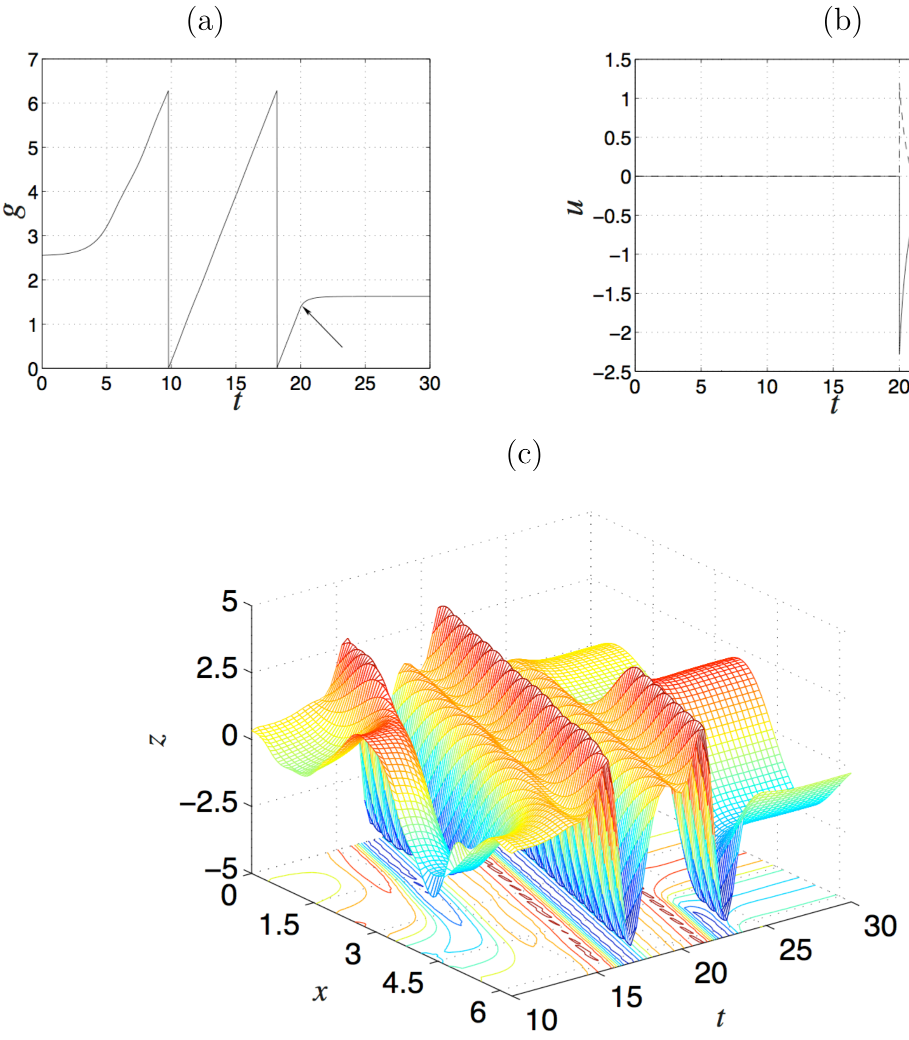

Figure 4.11: Plots for the same case as in Fig. 4.10. Plots are analogous to those in Fig. 4.7. Plot (a) shows that, with control, the dynamics approach a translation of $\tilde{z}_s$.

that the actuator can be translated in the symmetry direction. For this case, which we called the phase-amplitude actuation, the phase of the actuator was chosen such that the control has a zero component in the group direction. In the numerical example with Gaussian actuators, we mentioned that different choices of phases indeed yield better closed loop performance.

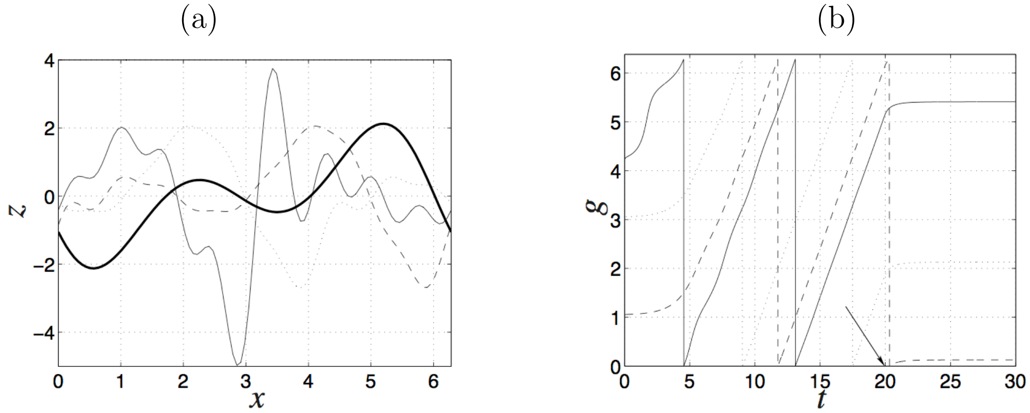

Figure 4.12: $\nu = 4/15$. Plot (b) shows the evolution of $g(t)$ for different initial conditions, shown in corresponding line styles in plot (a). The solid bold line in plot (a) represents the steady state $\tilde{z}_s$ used to define the slice dynamics.

Chapter 5

Conclusions and future work

5.1 Conclusions

In this work, we presented dimension reduction techniques for obtaining reduced-order models of the input-output dynamics of fluid flows. We demonstrated these techniques by stabilizing an unstable steady state in the flow past a flat plate at a large angle of attack and a low Reynolds number. We presented symmetry reduction techniques for stabilizing unstable relative equilibria such as traveling waves and self-similar solutions. Potential application for control of fluid flows was demonstrated by stabilizing unstable traveling waves of the translationally invariant Kuramoto-Sivashinsky equation.

The model reduction techniques presented in chapter 2 were based on balanced truncation, which was developed in the control theory community. Balanced truncation is attractive as it accurately captures the effect of both actuation and sensing. The resulting low-order models capture the dynamics of the original system with provable a-priori bounds on the error and are guaranteed to retain its stability properties. In comparison, proper orthogonal decomposition (POD) provides energetically optimal modes, but the models resulting from the subsequent Galerkin projection do not always capture the dynamics accurately and do not always retain the stability properties of the original system; for instance, the models of a full stable system could even be unstable.

The exact balanced truncation is intractable for large systems and an approximate algorithm was developed by Rowley (2005), for stable systems. We extended this algorithm to unstable systems, assuming a small number of unstable eigenvalues. The method presented was to project the full dynamics onto the stable subspace, using the unstable eigenmodes, and then obtaining its reduced models using the procedure for stable systems. The projection technique has also proven useful for obtaining balanced models of time-periodic systems, obtained from linearizing the nonlinear dynamics about a periodic orbit. Such linearizations have a neutral eigenmode, given by perturbations in the direction of the periodic orbit. In this case, the full dynamics are projected onto the stable subspace using the neutral (instead of unstable) eigenmodes; see Ma *et al.* (submitted).

Another attractive method, which results in the same reduced models as balanced truncation, is the eigensystem realization algorithm (ERA). We showed that the advantage of ERA is that it does not require adjoint simulations, and as a result can be used in experiments, at least for stable systems. We also showed that, when used in simulations, ERA requires an order of magnitude smaller computational effort than approximate balanced truncation.

The dimension reduction techniques developed in this work were applied to the two-dimensional flow past a flat plate at a low Reynolds number. The control actuation was modeled as a localized body force close to the leading or trailing edge of the flat plate, while sensing was through velocity measurements in the near-wake of the plate. We used time-stepper based techniques in combination with Krylov methods for bifurcation and linear stability analysis of the flow, varying the angle of attack from 0° to 90°. We developed reduced-order models of the input-output dynamics of the flow linearized about an unstable steady state at a large angle of attack. We used these models to develop reduced-order compensators, which were included in the full linear and nonlinear simulations. We showed that the controllers stabilized the unstable steady state, and more importantly, the models accurately reproduced the full system dynamics. When included in the nonlinear system, the controllers were able to suppress the periodic vortex shedding, implying a large domain of attraction of the stabilized steady state.

For the class of systems with a continuous symmetry, we used a symmetry-reduction procedure for control design; in particular, we extended the template-based procedure developed in Rowley *et al.* (2003) to systems with a control input. The method resulted in reducing the equations to a frame of reference in which the symmetry is factored out. The control goal was to stabilize unstable relative equilibria, which are simple steady states in the reduced frame. The reduced equations were then linearized about the steady state to obtain standard state-space equations. The formulation, obtained by reduction followed by linearization, was appealing as it allowed the use of standard tools from linear control theory. We considered two different actuators, which when included, retained the symmetry of the original system. In the first case, the actuation was assumed to be equivariant to the action of the symmetry group, and in the second case, arbitrary actuation was considered, while equivariance resulted from the freedom to move the actuator in the symmetry direction. In both cases, we derived optimal control techniques to stabilize unstable equilibria. Potential application of the developed methods towards control of fluid flows was demonstrated by stabilizing unstable traveling waves in the translationally invariant Kuramoto-Sivashinsky equation.

5.2 Future work

This dissertation has developed various techniques useful for obtaining reduced models of fluid flows that are suitable for feedback control design. However, many other areas remain to be explored, some of which are discussed here.

Model reduction of nonlinear systems. While the focus of this work was to develop models of linear state-space systems, most fluid flows in nature are essentially nonlinear. A natural step towards extending linear models to nonlinear systems would be to project the full nonlinear equations onto the balancing modes. Another interesting direction is development of algorithms to compute nonlinear balanced models, for instance based on the theoretical work of Scherpen (1993). There has been some effort on obtaining nonlinear models by balancing empirical Gramians or input and output coavariance matrices (Lee *et al.*, 2000; Lall *et al.*, 2002; Hahn *et al.*, 2003), although most of these directions involve computing many impulse response simulations and require large computational effort. Alternately, the balanced models of the linear system, which accurately capture the transient dynamics, could be combined with the POD-based models using shift-modes of Noack *et al.* (2005) which accurately capture vortex shedding and some of the transient dynamics.

Extend parameter range. The controllers present here are designed to operate at a fixed set of parameters (such as Reynolds number and angle of attack), and an important direction is to obtain models that are accurate over a range of off-design parameter values. In an initial study, Ilak & Rowley (2008) showed that the models of the linearized channel flow obtained at a fixed Re had a greater range of validity and better stability at off-design Re, as compared to POD models.

Optimal placement of sensors and actuators. The selection of both actuators and sensors was ad-hoc and not practically realizable. Numerically validated models of physically realistic actuation mechanisms such as wall blowing and suction should be developed, and more practical sensors such as surface pressure probes or shear stress sensors need to be considered. The actuation that was successful in suppressing vortex shedding was found after manual experimentation with various different choices. The combination of the fast immersed-boundary solver, two-dimensional flow, and ERA allowed a quick computation of reduced-order models and made it possible to explore a wide range of actuators and sensors. However, this iterative process can become expensive and laborious for three-dimensional simulations, which require more computational power. Hence, it is important to develop a systematic approach for optimizing actuator and sensor locations, and various parameters such as the width and strength of actuation. An extensive literature on selection of sensors and actuators is provided in van de Wal & de Jager (2001) and chapter 10 of Skogestad & Postlethwaite (2005), mostly with applications to chemical process control, vibration control in flexible structures and flight control. Most of these methods are limited to small-dimensional systems, and it would be useful to integrate the selection process with developing reduced-order models. For fluid flows, the recent works of Giannetti & Luchini (2007) and Marquet *et al.* (2008), which provided methods for identifying regions of the flow that acts as a wavemaker for exciting instabilities and are most receptive to external forcing, seem relevant for effective actuator selection.

Three-dimensional flows. The motivation for the choice of our model problem of the control of the two-dimensional flow past a flat plate was to develop tools towards manipulating wakes of micro-air vehicles. Recently, Taira & Colonius (2009*b*) performed a numerical study for understanding the physics of the three-dimensional flow past low-aspect-ratio plates, and showed that as the angle of attack is increased beyond the Hopf-bifurcation point, the flow undergoes a secondary bifurcation to an aperiodic regime. An interesting direction would be to to perform a detailed continuation study of this flow in order to determine the nature of this secondary bifurcation and also to explore the existence of high-lift unstable steady states in this 3-D flow.

Balanced truncation of systems with symmetry. The second class of systems considered in this work was those with a continuous symmetry, for which we developed feedback controllers to stabilize unstable relative equilibria. The dimensions of the system were small enough for direct application of linear control techniques. However, the dimensions would be much larger for systems arising from discretization of PDEs describing phenomena in two or three spatial coordinates. Using the idea of Rowley & Marsden (2000), the symmetry and dimension reduction ideas presented in this work could be easily combined to deal with such systems. First, symmetry could be factored out to obtain reduced dynamics, which have relative equilibria as steady states. The symmetry-reduced dynamics could be linearized about their steady states (which are relative equilibria) to obtain linear state-space equations. Dimension reduction could then be used to obtain reduced-order models and develop reduced-order controllers. The method could have interesting applications in pattern formation, for example, stabilizing spiral waves (Golubitsky & Stewart, 2002) and traveling or periodic structures (Postlethwaite & Silber, 2007).

Equation-free approach. An interesting direction would be to extend the reduction ideas to systems modeled at the fine or microscopic scales, while the dynamics of interest (say, for control) occurs at much larger or macroscopic scales. In the traditional approach, the effect of the microscopic scales on the macroscopic scales is analytically derived and used to obtain a closed-form equation describing the macroscopic dynamics. However, such a derivation is not possible in many cases, for which the equation-free approach of Theodoropoulos *et al.* (2000); Kevrekidis *et al.* (2003) is useful as it effectively solves for the large scale dynamics without ever deriving their equations in closed form. The method also allows the performance of various computational tasks such as bifurcation analysis and control design directly at the coarse level (Aronson *et al.*, 2001; Armaou *et al.*, 2004). An interesting direction would be to extend the symmetry and dimension reduction methods presented in this work to the equation-free framework.

Symmetry reduction ideas have been applied in the equation-free setting in Kavousanakis *et al.* (2007) and could be combined with this work for stabilizing relative equilibria of the macroscopic dynamics. Sirisup *et al.* (2005) used POD modes and the equation-free framework to integrate reduced-order models without deriving them in closed form; computational savings over the direct numerical solver were demonstrated for the flow past a cylinder. For capturing input-output dynamics, model dimension reduction using ERA could also be applied in this setting, since it requires only the input-output data from impulse response simulations. However, the approximate balanced truncation procedure requires adjoint simulations of the effective coarse dynamics, which in general are not available.

Control of group dynamics. In this work, symmetry reduction was performed to decompose the dynamics into two components, one related to the symmetry variable and the other to the remaining variables called shape variables. The resulting controllers were designed to stabilize only the dynamics associated with the shape variables. A natural extension would be to also control the group dynamics to achieve complete stabilization in full phase space by breaking the symmetry, as was done in Bloch *et al.* (2001). For systems with translational symmetry, this would imply stabilizing a particular steady state or a particular shift of a traveling wave profile from the one-parameter family.

Appendix A

Balancing transformation for unstable systems

Without loss of generality, the transformation T (and its inverse) that decouples the stable and unstable dynamics of (2.1, 2.2) can be written as:

$$T = \begin{pmatrix} T_u & T_s \end{pmatrix}, \qquad T^{-1} = \begin{pmatrix} S_u^* \\ S_s^* \end{pmatrix}, \tag{A.1}$$

where the columns of T_u and T_s span the unstable and stable *right* eigenspaces of A, while the columns of S_u and S_s span the unstable and stable *left* eigenspaces of A. Further, these matrices are scaled such that $S_u^* T_u = I_{n_u}$ and $S_s^* T_s = I_{n_s}$. The transformation (A.1) decouples the dynamics of (2.1) as given in (2.40) with the various matrices defined as follows:

$$A_u = S_u^* A T_u, \quad B_u = S_u^* B, \quad C_u = C T_u, \tag{A.2}$$

$$A_s = S_s^* A T_s, \quad B_s = S_s^* B, \quad C_s = C T_s. \tag{A.3}$$

Using (A.1) in (2.42, 2.43), the Gramians of the original system (2.1, 2.2) are

$$W_c = T_u W_c^u T_u^* + T_s W_c^s T_s^*, \tag{A.4}$$

$$W_o = S_u^* W_o^u S_u + S_s^* W_o^s S_s, \tag{A.5}$$

where, W_c^s and W_o^s are the Gramians corresponding to the system defined by the triplet (A_s, B_s, C_s), while W_c^u and W_o^u are the Gramians corresponding to the system defined $(-A_u, B_u, C_u)$. Let $\widetilde{\Phi}_u \in \mathbb{R}^{n_u \times n_u}$ be the transformation that balances the Gramians W_c^u and W_o^u, while $\widetilde{\Phi}_s \in \mathbb{R}^{n_s \times n_s}$ be the transformation that balances W_c^s and W_o^s. Then, it can be verified that the transformation that balances the Gramians W_c and W_o is given by

$$\Phi = \begin{pmatrix} T_u \widetilde{\Phi}_u & T_s \widetilde{\Phi}_s \end{pmatrix} \overset{\text{def}}{=} \begin{pmatrix} \Phi_u & \Phi_s \end{pmatrix}. \tag{A.6}$$

Thus, the balancing transformation consists of two parts Φ_u and Φ_s which respectively balance the dynamics on the unstable and stable subspaces of A. As per the technique of Zhou *et al.* (1999), a reduced-order model can be obtained by truncating the columns of Φ that correspond to the relatively uncontrollable and unobservable states. As we will show now, the algorithm outlined in section 2.2.2 essentially computes the leading columns of Φ_s (and the corresponding rows of its inverse). We show that the controllability Gramian of the stable dynamics of (2.1), which are defined by (2.45), is the same as the "stable" part of the Gramian defined in (A.5). Note that using (A.1) and the definition (2.44), the projection operator $\mathbb{P}_s$ can be written as

$$\mathbb{P}_s = I - T_u S_u^* = T_s S_s^*. \tag{A.7}$$

Using the definition (2.16), the controllability Gramian of (2.45, 2.46) is

$$\begin{aligned}
\widetilde{W}_c^s &= \int_0^\infty e^{\mathbb{P}_s A t} (\mathbb{P}_s B)\,(\mathbb{P}_s B)^* e^{(\mathbb{P}_s A)^* t}\; dt \\
&= \int_0^\infty T_s\; e^{S_s^* A T_s t}\; S_s^* B\; B^* S_s\; e^{T_s^* A^* S_s t}\; T_s^*\; dt \qquad \text{using equation (A.7)} \\
&= T_s \Big(\int_0^\infty e^{A_s t}\; B_s B_s^*\; e^{A_s^* t}\; dt \Big) T_s^* \qquad \text{using equation (A.3)} \\
&= T_s W_c^s T_s^*,
\end{aligned} \tag{A.8}$$

which is the same as the stable part of W_c. Similarly, it can be shown that the observability Gramian $\widetilde{W}_o^s$ of (2.45, 2.46) is the same as the "stable" part of the observability Gramian W_o:

$$\widetilde{W}_o^s = \int_0^\infty e^{\mathbb{P}_s^* A^* t} (\mathbb{P}_s^* C^*)\,(\mathbb{P}_s^* C^*)^* e^{(\mathbb{P}_s^* A^*)^* t}\; dt = S_s^* W_o^s S_s. \tag{A.9}$$

Thus, balancing the Gramians $\widetilde{W}_o^s$ and $\widetilde{W}_c^s$ is identical to balancing the parts of the Gramians W_c and W_o of the original system (2.1) that are related to the dynamics on the stable subspace of A.

Appendix B

Derivation of the adjoint equations

B.1 Adjoint formulation of the immersed boundary method

In this appendix, we derive the adjoint of the linearized semi-discrete equations (3.16, 3.17). Let (ζ, ψ) be the weighting functions corresponding to $(\gamma, \tilde{f})$. Then, using the inner product defined in equation (3.19), the weak form of (3.16, 3.17) is:

$$\int_0^T \int_\Omega \zeta \cdot (C^T C)^{-1} \Big(\frac{d\gamma}{dt} + C^T E^T \tilde{f} + \beta C^T C \gamma - C^T \mathcal{N}_L(\gamma_s)\gamma \Big)\, dx\, dt \\ + \int_0^T \int_\Omega \psi \cdot E C s \, dx\, dt = 0. \tag{B.1}$$

Integrating by parts with respect to t and rearranging terms,

$$\int_0^T \int_\Omega \gamma \cdot \Big(-(C^T C)^{-1} \frac{d\zeta}{dt} + (C^T C)^{-1} C^T E^T \psi + \beta \zeta - \big((C^T C)^{-1} C^T \mathcal{N}_L(\gamma_s) \big)^T \zeta \Big) dx\, dt \\ + \int_0^T \int_\Omega \tilde{f} \cdot \Big(E C (C^T C)^{-1} \zeta \Big)\, dx\, dt + \langle \gamma, \zeta \rangle \Big|_0^T = 0. \tag{B.2}$$

For linearization about stable steady states, $\gamma \to 0$, as $T \to \infty$, and if the adjoint equations are integrated backwards in time, $\zeta(t = 0) \to 0$. So, the last term on the left hand side of equation (B.2) vanishes identically. If equation (B.2) is to hold for all values of γ and $\tilde{f}$, we get the following adjoint equations hold:

$$-\frac{d\zeta}{dt} + C^T E^T \psi = -\beta C^T C \zeta + (C^T C) \mathcal{N}_L(\gamma_s)^T q_a, \tag{B.3}$$

$$E C \xi = 0, \tag{B.4}$$

where $\xi = (C^T C)^{-1} \zeta$ and $q_a = C\xi$ can be thought of as the weighting functions corresponding to the streamfunction s and the flux q respectively. Now, equations (B.3, B.4) have the same form as (3.16, 3.17) except for the nonlinear term.

Thus, the same time-integration scheme can be used for both, with the appropriate (linearized) nonlinear terms.

B.2 Adjoint of differential algebraic equations

Consider the state-space system defined in (2.1, 2.2)

$$\dot{x} = Ax + Bu, \tag{B.5}$$

$$y = Cx, \tag{B.6}$$

where although $x \in \mathbb{R}^n$, it is constrained to evolve on a m-dimensional subspace; for instance, in case of the immersed boundary formulation of the linearized Navier-Stokes equations, it is restricted to evolve on the subspace defined by the velocity fields that are divergence-free and satisfy the no-slip boundary conditions at the body surface. Mathematically, x satisfies the constraint

$$Fx = 0, \tag{B.7}$$

where the operator $F \in \mathbb{R}^{m\times n}$ where $m < n$. The equations (B.5, B.6, B.7) form a set of differential-algebraic equations. In order to find the adjoint of these equations, we obtain a minimal state-space representation defined by only differential equations. We first construct a matrix $H \in \mathbb{R}^{n\times m}$, such that

$$FH = 0 \quad \text{and} \quad H^T H = I, \tag{B.8}$$

that is, the columns of H form an orthonormal basis spanning the null-space of F. Since x satisfies (B.7), we can write

$$x = H\tilde{x}. \tag{B.9}$$

Substituting (B.9) in (B.5, B.6), left-multiplying by H^T and using (B.8), we obtain the minimal state-space realization:

$$\dot{\tilde{x}} = H^T AH\tilde{x} + H^T Bu \overset{\text{def}}{=} \tilde{A}\tilde{x} + \tilde{B}u, \tag{B.10}$$

$$y = CH\tilde{x} \overset{\text{def}}{=} \tilde{C}\tilde{x}. \tag{B.11}$$

Assuming L^2- inner-products, the adjoint of (B.10, B.11) is simply given by

$$\dot{\tilde{z}} = \tilde{A}^T\tilde{z} + \tilde{C}^T v, \tag{B.12}$$

$$w = \tilde{B}^T\tilde{z}, \tag{B.13}$$

where $\tilde{z}$, v and w are dual to the state $\tilde{x}$, input u and output y. Then, left-multiply (B.12) by H,

$$H\dot{\tilde{z}} = HH^T A^T H\tilde{z} + HH^T C^T v \tag{B.14}$$

$$w = B^T\tilde{z} \tag{B.15}$$

and define the dual to the state x by $z = H\tilde{z}$ to obtain the adjoint formulation of the differential-algebraic equations (B.5, B.6, B.7):

$$\dot{z} = \mathbb{P}_H A^T z + \mathbb{P}_H C^T v \overset{\text{def}}{=} A^* z + C^* v \tag{B.16}$$

$$w = B^T z \overset{\text{def}}{=} B^* z, \tag{B.17}$$

$$\text{where,} \qquad \mathbb{P}_H \overset{\text{def}}{=} H H^T \tag{B.18}$$

is an orthogonal projection onto the columns of H. The adjoint state z is constrained to satisfy (B.7); that is, the adjoint field obtained in the immersed boundary formulation, is divergence free and satisfies the no-slip boundary condition at the body surface. Further, the adjoint of the output matrix is obtained by taking its transpose, followed by a projection onto the columns of H.

Appendix C

Linearization of slice dynamics

Let $\tilde{z} = \tilde{z}_s + w$, and $\tilde{u} = 0 + v$, where $\|w\|, \|v\| \ll 1$. Substituting in (4.8), we get

$$\begin{aligned}\dot{w} =& X(z_s, 0) + D_{\tilde{z}}X(z_s, 0)w + D_{\tilde{u}}X(\tilde{z}_s, 0)v - Y(\tilde{z}_s + w)(\xi_0 + \xi_1) + O(2)\\ =& \underbrace{X(z_s, 0) - Y(\tilde{z}_s)\xi_0}_{O(0)} +\\ & \underbrace{D_{\tilde{z}}X(z_s, 0)w + D_{\tilde{u}}X(\tilde{z}_s, 0)v - Y(\tilde{z}_s)\xi_1 - D_{\tilde{z}}Y(\tilde{z}_s)w \cdot \xi_0}_{O(1)} + O(2).\end{aligned} \tag{C.1}$$

Here, ξ_0 and ξ_1 are the zeroth and first order terms in the expansion of ξ. The exact form of these terms follows. Let $A = D_{\tilde{z}}X(\tilde{z}_s, 0)$ and $B = D_{\tilde{u}}X(\tilde{z}_s, 0)$. Substituting $\tilde{z} = \tilde{z}_s + w$, $\tilde{u} = v$ in (4.17),

$$\begin{aligned}\xi =& \Big(Y^*(z_0)Y(\tilde{z}_s + w)\Big)^{-1} Y^*(z_0)X(\tilde{z}_s + w, v)\\ =& \Big(Y^*(z_0)(Y(\tilde{z}_s) + D_{\tilde{z}}Y(\tilde{z}_s)w)\Big)^{-1} Y^*(z_0)(X(\tilde{z}_s, 0) + Aw + Bv) + O(2)\\ =& \Big(Y^*(z_0)Y(\tilde{z}_s)\Big)^{-1/2}\Big(I - (Y^*(z_0)Y(\tilde{z}_s))^{-1/2}Y^*(z_0)D_{\tilde{z}}Y(\tilde{z}_s)w(Y^*(z_0)Y(\tilde{z}_s))^{-1/2}\Big)\\ & \Big(Y^*(z_0)Y(\tilde{z}_s)\Big)^{-1/2} Y^*(z_0)(X(\tilde{z}_s, 0) + Aw + Bv) + O(2)\\ =& \Big(Y^*(z_0)Y(\tilde{z}_s)\Big)^{-1}\Big(Y^*(z_0)(\underbrace{X(\tilde{z}_s, 0)}_{O(0)} + \underbrace{Aw + Bv}_{O(1)}) -\\ & \underbrace{Y^*(z_0)D_{\tilde{z}}Y(\tilde{z}_s)w\Big(Y^*(z_0)Y(\tilde{z}_s)\Big)^{-1} Y^*(z_0)X(\tilde{z}_s, 0)}_{O(1)}\Big) + O(2)\end{aligned} \tag{C.2}$$

$$\overset{\text{def}}{=} \xi_0 + \xi_1 + O(2). \tag{C.3}$$

That is, the terms at $O(0)$ and $O(1)$ in (C.2) define ξ_0 and ξ_1 respectively. Now, define the following projection operator:

$$\mathbb{P}_{S_{z_0}} = I - Y(\tilde{z}_s)\Big(Y^*(z_0)Y(\tilde{z}_s)\Big)^{-1}Y^*(z_0) \tag{C.4}$$

which is a projection onto the space orthogonal to the columns of $Y(z_0)$. Then, combining (C.1, C.2, C.4), we get

$$\begin{aligned} \dot{w} =& \mathbb{P}_{S_{z_0}}(X(z_s,0) + Aw + Bv) \\ & - \mathbb{P}_{S_{\tilde{z}_s}} D_{\tilde{z}} Y(\tilde{z}_s) w \Big(Y^*(z_0)Y(\tilde{z}_s)\Big)^{-1} Y^*(z_0) X(\tilde{z}_s,0) + O(2) && \text{(C.5)} \\ \overset{\text{def}}{=}& \mathbb{P}_{S_{\tilde{z}_s}}(\hat{A}w + \hat{B}v) + O(2). && \text{(C.6)} \end{aligned}$$

Here, we have used the fact that since $\tilde{z}_s$ is a fixed point of the slice dynamics, $\mathbb{P}_{S_{z_0}} X(\tilde{z}_s,0) = 0$.

Bibliography

Åkervik, E., Brandt, L., Henningson, D. S., Hœpffner, J., Marxen, O. & Schlatter, P. 2006 Steady solutions of the Navier-Stokes equations by selective frequency damping. *Physics of Fluids* **18**, 068102.

Åkervik, E., Hœpffner, J., Ehrenstein, U. & Henningson, D. S. 2007 Optimal growth, model reduction and control in a separated boundary-layer flow using global eigenmodes. *Journal of Fluid Mechanics* **579**, 305–314.

Ahuja, S., Kevrekidis, I. G. & Rowley, C. W. 2007 Template-based stabilization of relative equilibria in systems with continuous symmetry. *Journal of Nonlinear Science* **17** (2), 109–143.

Ahuja, S. & Rowley, C. W. 2009 Feedback control of unstable steady states of flow past a flat plate using reduced-order estimators. *Journal of Fluid Mechanics* (submitted).

de Almeida, V. F. & Derby, J. J. 2000 Construction of solution curves for large two-dimensional problmes of steady-state flows of incompressible fluids. *SIAM Journal on Scientific Computing* **22** (1), 285–311.

Armaou, A. & Christofides, P. D. 2000 Feedback control of the kuramoto-sivashinsky equation. *Physica D. Nonlinear Phenomena* **137**, 49–61.

Armaou, A., Siettos, C. I. & Kevrekidis, I. G. 2004 Time-steppers and 'coarse' control of distributed microscopic processes. *International Journal of Robust and Nonlinear Control* **12** (2), 89–111.

Armbruster, D., Guckenheimer, J. & Holmes, P. 1988 Heteroclinic cycles and modulated traveling waves in systems with O(2) symmetry. *Physica D. Nonlinear Phenomena* **29** (3), 257–282.

Arnoldi, W. E. 1951 The principle of minimized iterations in the solution of the matrix eigenvalue problem. *Quarterly of Applied Mathematics* **9**, 17–29.

Aronson, D. G., Betelu, S. I. & Kevrekidis, I. G. 2001 Going with the flow: a Lagrangian approach to self-similar dynamics and its consequences. http://arxiv.org/abs/nlin.AO/0111055.

Avila, M., Marques, F., Lopez, J. M. & Meseguer, A. 2007 Stability control and catastrophic transition in a forced taylor-couette system. *Journal of Fluid Mechanics* **590**, 471–496.

Bagheri, S., Brandt, L. & Henningson, D. S. 2009*a* Input–output analysis, model reduction and control of the flat-plate boundary layer. *Journal of Fluid Mechanics* **620**, 263–298.

Bagheri, S., Schlatter, P., Schmid, P. J. & Henningson, D. S. 2009*b* Global stability of a jet in cross-flow. *Journal of Fluid Mechanics* **624**, 33–44.

Bamieh, B., Paganini, F. & Dahleh, M. A. 2002 Distributed control of spatially invariant systems. *IEEE Transactions on Automatic Control* **47** (7), 1091–1107.

Barkley, D. 2006 Linear analysis of the cylinder wake mean flow. *Europhysics Letters* **75** (5), 750–756.

Barkley, D., Gomes, M. G. M. & Henderson, R. 2002 Three-dimensional instability in flow over a backward-facing step. *Journal of Fluid Mechanics* **473**, 167–190.

Barkley, D. & Henderson, R. D. 1996 Three-dimensional floquet stability analysis of the wake of a circular cylinder. *Journal of Fluid Mechanics* **322**, 215–241.

Barkley, D. & Tuckerman, L. S. 1999 Stability analysis of perturbed plane couette flow. *Physics of Fluids* **11**, 1187–1195.

Beyn, W.-J. & Thümmler, V. 2004 Freezing solutions of equivariant evolution equations. *SIAM Journal on Applied Dynamical Systems* **3** (2), 85–116.

Birch, J. M. & Dickinson, M. H. 2001 Spanwise flow and the attachment of the leading-edge vortex on insect wings. *Nature* **412**, 729–733.

Bloch, A. M., Chang, D.-E., Leonard, N. E. & Marsden, J. E. 2001 Controlled lagrangians and the stabilization of mechanical systems ii: Potential shaping. *IEEE Transactions on Automatic Control* **46** (10), 1556–71.

Bloch, A. M., Leonard, N. E. & Marsden, J. E. 2000 Controlled lagrangians and the stabilization of mechanical systems i: The matching theorem. *IEEE Transactions on Automatic Control* **45** (12), 2253–2270.

Bodenschatz, E., Pesch, W. & Ahlers, G. 2000 Recent developmentsin rayleigh-bénard convection. *Annual Review of Fluid Mechanics* **32**, 709–778.

Brockett, R. W. & Willems, J. L. 1974 Discretized partial differential equations: Examples of control systems defined on modules. *Automatica* **10**, 507–515.

Bullo, F. 2000 Stabilization of relative equilibria for underactuated systems on riemannian manifolds. *Automatica* **36**, 1819–34.

Cabell, R. H., Kegerise, M. A., Cox, D. E. & Gibbs, G. P. 2006 Experimental feedback control of flow-induced cavity tones. *AIAA Journal* **44** (8), 1807–1815.

Cattafesta, III, L. N., Garg, S., Choudhari, M. & Li, F. 1997 Active control of flow-induced cavity resonance. AIAA Paper 97-1804.

Choi, H., Jeon, W.-P. & Kim, J. 2008 Control of flow over a bluff body. *Annual Review of Fluid Mechanics* **40**, 113–39.

Chowdhury, M. K. & Tuckerman, L. S. 1995 Asymmetry and hopf bifurcation in spherical couette flow. *Physics of Fluids* **7** (1), 80–91.

Cliffe, K. A., Spence, A. & Tavener, S. J. 2000 The numerical analysis of bifurcation problems with application to fluid mechanics. *Acta Numerica* pp. 39–131.

Cobb, J. D. 1981 Feedback and pole placement in descriptor variable systems. *International Journal of Control* **33** (6), 1135–46.

Cobb, J. D. 1983 Descriptor variable systems and optimal state regulation. *International Journal of Control* **28** (5), 601–611.

Coller, B. D. 1995 Suppression of heteroclinic bursts in boundary layer models. PhD thesis, Cornell University.

Colonius, T. & Taira, K. 2008 A fast immersed boundary method using a nullspace approach and multi-domain far-field boundary conditions. *Computer Methods in Applied Mechanics and Engineering* **197** (25-28), 2131–46.

Corke, T. C., Glauser, M. N. & Berkooz, G. 1994 Utilizing low-dimensional dynamical systems models to guide control experiments. *Applied Mechanics Reviews* **47** (6), 133–138.

Cortelezzi, L. 1996 Nonlinear feedback control of the wake past a plate with a suction point on the downstream wall. *Journal of Fluid Mechanics* **327**, 303–324.

Cortelezzi, L., Chen, Y.-C. & Chang, H.-L. 1997 Nonlinear feedback control of the wake past a plate: From a low-order model to a higher-order model. *Physics of Fluids* **9** (7), 2009–2022.

Crawford, J. D. & Knobloch, E. 1991 Symmetry and symmetry-breaking bifurcations in fluid dynamics. *Annual Review of Fluid Mechanics* **23**, 341–387.

Dai, L. 1989 *Singular control systems*, *Lecture notes in control and information sciences*, vol. 118. Berlin-Heidelberg: Springer-Verlag.

D'Andrea, R. & Dullerud, G. E. 2003 Distributed control design for spatially interconnected systems. *IEEE Transactions on Automatic Control* **48** (9), 1478–95.

Deane, A. E., Kevrekidis, I. G., Karniadakis, G. E. & Orszag, S. A. 1991 Low-dimensional models for complex geometry flows: Application to grooved channels and circular cylinders. *Physics of Fluids A* **3** (10), 2337–54.

Doedel, E. J., Keller, H. B. & Kernevez, J. P. 1991 Numerical analysis and control of bifurcation problems, part II. *International Journal of Bifurcation and Chaos* **1** (4), 745–772.

Dubljevic, S., Christofides, P. D. & Kevrekidis, I. G. 2004 Distributed nonlinear control of diffusion-reaction processes. *International Journal of Robust and Nonlinear Control* **14**, 133–156.

Ellington, C. P., van der Berg, C., Willmott, A. P. & Thomas, A. L. R. 1996 Leading-edge vortices in insect flight. *Nature* **384**, 626–630.

Gaitonde, A. L. & Jones, D. P. 2003 Reduced order state-space models from the pulse responses of a linearized cfd scheme. *International Journal for Numerical Methods in Fluids* **42**, 581–606.

Giannetti, F. & Luchini, P. 2007 Structural sensitivity of the first instability of the cylinder wake. *Journal of Fluid Mechanics* **581**, 167–197.

Gillies, E. A. 1998 Low-dimensional control of the circular cylinder wake. *Journal of Fluid Mechanics* **371**, 157–178.

Gloerfelt, X. 2008 Compressible proper orthogonal decomposition/galerkin reduced-order model of self-sustained oscillations in a cavity. *Physics of Fluids* **20**, 115105.

Golubitsky, M. & Schaeffer, D. G. 1985 *Singlularities and Groups in Bifurcation Theory I*, *Applied Mathematical Sciences*, vol. 51. New York: Springer-Verlag.

Golubitsky, M. & Stewart, I. 2002 *The Symmetry Perspective: From Equilibrium to Chaos in Phase Space and Physical Space*, *Progress in mathematics*, vol. 200. Basel: Birkh´auser.

GOLUBITSKY, M., STEWART, I. & SCHAEFFER, D. G. 1988 *Singlularities and Groups in Bifurcation Theory II*, *Applied Mathematical Sciences*, vol. 69. New York: Springer-Verlag.

GRAHAM, W. R., PERAIRE, J. & TANG, K. Y. 1999*a* Optimal control of vortex shedding using low-order models. part 1 - open-loop model development. *International Journal for Numerical Methods in Engineering* **44** (7), 945–972.

GRAHAM, W. R., PERAIRE, J. & TANG, K. Y. 1999*b* Optimal control of vortex shedding using low-order models. part 2 - model-based control. *International Journal for Numerical Methods in Engineering* **44** (7), 973–990.

GREENBLATT, D. & WYGNANSKI, I. J. 2000 The control of flow separation by periodic excitation. *Progress in Aerospace Sciences* **36**, 487–545.

GRIZZLE, J. & MARCUS, S. 1984 Optimal control of systems possessing symmetries. *IEEE Transactions on Automatic Control* **29** (11), 1037–40.

GRIZZLE, J. & MARCUS, S. 1985 The structure of nonlinear control systems possessing symmetries. *IEEE Transactions on Automatic Control* **30** (3), 248–258.

HAGEN, G. & MEZIĆ, I. 2003 Spillover stabilization in finite-dimensional control and observer design for dissipative evolution equations. *SIAM Journal on Control and Optimization* **42** (2), 746–768.

HAHN, J., EDGAR, T. F. & MARQUARDT, W. 2003 Controllability and observability covariance matrices for the analysis and order reduction of stable nonlinear systems. *Journal of Process Control* **13** (2), 115–127.

HENNINGSON, D. S. & ÅKERVIK, E. 2008 The use of global modes to understand transition and perform flow control. *Physics of Fluids* **20** (031302).

HOLMES, P., LUMLEY, J. L. & BERKOOZ, G. 1996 *Turbulence, Coherent Structures, Dynamical Systems and Symmetry*. Cambridge, UK: Cambridge University Press.

ILAK, M. & ROWLEY, C. W. 2008 Modeling of transitional channel flow using balanced proper orthogonal decomposition. *Phys. Fluids* **20**, 034103.

JALNAPURKAR, S. & MARSDEN, J. E. 1999 Stabilization of relative equilibria ii. *Regular and Chaotic Dynamics* **3**, 161–179.

JALNAPURKAR, S. & MARSDEN, J. E. 2000 Stabilization of relative equilibria. *IEEE Transactions on Automatic Control* **45** (8), 1483–91.

Jolly, M. S., Kevrekidis, I. G. & Titi, E. S. 1990 Approximate inertial manifolds for the kuramoto-sivashinsky equation: analysis and computations. *Physica D. Nonlinear Phenomena* **44** (1-2), 38–60.

Juang, J.-N. & Pappa, R. S. 1985 An eigensystem realization algorithm for modal parameter identification and model reduction. *Journal of Guidance, Control, and Dynamics* **8** (5), 620–627.

Justh, E. W. & Krishnaprasad, P. S. 2004 Equilibria and steering laws for planar formations. *Systems and Control Letters* **52**, 25–38.

Kavousanakis, M. E., Erban, R., Boudouvis, A. G., Gear, C. W. & Kevrekidis, I. G. 2007 Projective and coarse projective integration for problems with continuous symmetries. *Journal of Computational Physics* **225** (1), 382–407.

Kelley, C. T. 1995 *Iterative methods for linear and nonlinear equations*. *Frontiers in Applied Mathematics* 16. Society for Industrial and Applied Mathematics.

Kelley, C. T., Kevrekidis, I. G. & Qiao, L. 2004 Newton-Krylov solvers for timesteppers. http://arxiv.org/math/0404374.

Kevrekidis, I. G., Gear, C. W., Hyman, J. M., Kevrekidis, P. G., Runborg, O. & Theodoropoulos, C. 2003 Equation-free coarse-grained multiscale computation: enabling microscopic simulators to perform system-level tasks. *Comm. Math. Sciences* **1** (4), 715–762.

Kevrekidis, I. G., Nicolaenko, B. & Scovel, J. 1990 Back in the saddle again: A computer assisted study of the kuramoto-sivashinsky equation. *SIAM Journal on Applied Mathematics* **50** (3), 760–790.

Kim, J. & Bewley, T. R. 2007 A linear systems approach to flow control. *Annual Review of Fluid Mechanics* **39**, 383–417.

Krishnan, H. & McClamroch, N. H. 1992 Computation of state realizations for control systems described by a class of linear differential-algebraic equations. *International Journal of Control* **55** (6), 1425–41.

Kumar, A. & Daoutidis, P. 1995 Feedback control of nonlinear differential-algebraic equations. *AIChE Journal* **41** (3), 619–636.

Kumar, A. & Daoutidis, P. 1996 State-space realizations of linear differential-algebraic-equation systems with control-dependent systems. *IEEE Transactions on Automatic Control* **41** (2), 269–274.

Kumar, A. & Daoutidis, P. 1999 *Control of nonliinear differential algebraic equation systems with applications to chemical processes*. Chapman and Hall/CRC Research Notes in Mathematics.

Lall, S., Marsden, J. E. & Glavaški, S. 2002 A subspace approach to balanced truncation for model reduction of nonlinear control systems. *Int. J. Robust Nonlinear Control* **12**, 519–535.

Lee, C. H. & Tran, H. T. 2005 Reduced-order-based feedback control of the kuramoto-sivashinsky equation. *Journal of Computational and Applied Mathematics* **173** (1), 1–19.

Lee, K. S., Eom, Y., Chung, J. W., Choi, J. & Yang, D. 2000 A control-relevant model reduction technique for nonlinear systems. *Computers and Chemical Engineering* **24**, 309–315.

Lehoucq, R. B., Sorensen, D. C. & Yang, C. 1998 *ARPACK Users' Guide*. Society for Industrial and Applied Mathematics.

Lewis, J. & Martin, C. 1983 Linear quadratic control optimal control for symmetric systems. In *Proc. IEEE Conf. Decision and Control*, pp. 907–909.

Lorenz, E. N. 1956 Empirical orthogonal functions and statistical weather prediction. Department of Meteorology Statistical Forecasting Project 1. Massachusetts Institute of Technology.

Lou, Y. & Christofides, P. D. 2003 Optimal actuator/sensor placement for nonlinear control of the kuramoto-sivashinsky equation. *IEEE Transactions on Control Systems Technology* **11**, 737–745.

Luchtenburg, D. K., G´unther, B., Noack, B. R., King, R. & Tadmor, G. 2009 A generalized mean-field model of the natural and high-frequency actuated flow around a high-lift configuration. *Journal of Fluid Mechanics* **623**, 283–316.

Lumley, J. L. 1970 *Stochastic Tools in Turbulence*. New York: Academic Press.

Lumley, J. L. & Blossey, P. 1998 Control of turbulence. *Annual Review of Fluid Mechanics* **30**, 311–27.

Ma, Z., Ahuja, S. & Rowley, C. W. 2009 Reduced order models for control of fluids using the eigensystem realization algorithm. *Journal of Fluid Mechanics* (submitted).

Ma, Z., Rowley, C. W. & Tadmor, G. submitted Snapshot-based balanced truncation for linear time-periodic systems. *IEEE Transactions on Automatic Control* .

Marques, F. & Lopez, J. M. 1997 Taylor-Couette flow with axial oscillations of the inner cylinder: Floquet analysis of the basic flow. *Journal of Fluid Mechanics* **348**, 153–175.

Marquet, O., Sipp, D. & Jacquin, L. 2008 Sensitivity analysis and passive control of cylinder flow. *Journal of Fluid Mechanics* **615**, 221–252.

Marsden, J. E. 1992 *Lectures on Mechanics*, *London Mathematical Society Lecture Note Series*, vol. 174. Cambridge University Press.

Marsden, J. E. & Ratiu, T. S. 1994 *Introduction to mechanics and symmetry*, 2nd edn., *Texts in Applied Mathematics*, vol. 17. Springer-Verlag.

Moore, B. C. 1981 Principal component analysis in linear systems: Controllability, observability, and model reduction. *IEEE Transactions on Automatic Control* **26** (1), 17–32.

Mozhaev, G. V. 1975*a* Use of symmetry in linear optimal control problems with a quadratic performance index - i. *Automatic and Remote Control* **36** (6), 892–899.

Mozhaev, G. V. 1975*b* Use of symmetry in linear optimal control problems with a quadratic performance index - ii. *Automatic and Remote Control* **36** (7), 1069–76.

Nair, S. & Leonard, N. E. 2007 Stable synchronization of rigid body networks. *Networks and Heterogeneous Media* **2** (4), 595–624.

Nicolaenko, C., Foias, B., Temam, R. & Constantin, P. 1989 *Integral manifolds and inertial manifolds for dissipative partial differential equations*, *Applied Mathematical Sciences*, vol. 70. New York, NY: Springer.

Noack, B., Afanasiev, K., Morzyński, M., Tadmor, G. & Thiele, F. 2003 A hierarchy of low-dimensional models for the transient and post-transient cylinder wake. *Journal of Fluid Mechanics* **497**, 335–363.

Noack, B. R., Papas, P. & Monkewitz, P. A. 2005 The need for a pressure-term representation in empirical Galerkin models of incompressible shear flow. *Journal of Fluid Mechanics* **523**, 339–365.

Noack, B. R., Pelivan, I., Tadmor, G., Morzyński, M. & Comte, P. 2004 Robust low-dimensional Galerkin models of natural and actuated flows. In *Fourth Aeroacoustics Workshop*. RWTH Aachen 26–27 Feb. 2004.

Or, A. C., Cortelezzi, L. & Speyer, J. L. 2001 Robust feedback control of rayleigh-b/'enard convection. *Journal of Fluid Mechanics* **437**, 175–202.

Pastoor, M., Henning, L., Noack, B. R., King, R. & Tadmor, G. 2008 Feedback shear layer control for bluff body drag reduction. *Journal of Fluid Mechanics* **608**, 161–196.

Peskin, C. S. 1972 Flow patterns around heart valves: a numerical method. *Journal of Computational Physics* **11**, 479–517.

Postlethwaite, C. M. & Silber, M. 2007 Spatial and temporal feedback control of traveling wave solutions of the two-dimensional complex ginzburg-landau equation. *Physica D. Nonlinear Phenomena* **236**, 65–74.

Prabhu, R. D., Collis, S. S. & Chang, Y. 2001 The influence of control on proper orthogonal decomposition of wall-bounded turbulent flows. *Physics of Fluids* **12** (2), 520–37.

Protas, B. 2008 Vortex dynamics models in flow control problems. *Nonlinearity* pp. R203–R250.

Provansal, M., Mathis, C. & Boyer, L. 1987 Bénard-von kármán instability: transient and forced regimes. *Journal of Fluid Mechanics* **182**, 1–22.

Ravindran, S. S. 2000 A reduced-order approach for optimal control of fluids using proper orthogonal decomposition. *International Journal for Numerical Methods in Engineering* **34**, 425–488.

Roberts, M., Wulff, C. & Lamb, J. S. W. 2002 Hamiltonian systems near relative equilibria. *Journal of Differential Equations* **179**, 562–604.

Rowley, C. W. 2005 Model reduction for fluids using balanced proper orthogonal decomposition. *International Journal of Bifurcation and Chaos* **15** (3), 997–1013.

Rowley, C. W., Ahuja, S., Taira, K. & Colonius, T. 2008 Closed-loop control of leading edge vorticity on a 3d wing: Simulations and low-dimensional models. AIAA Paper 2008-3981, 38th Fluid Dynamics Conference and Exhibit.

Rowley, C. W. & Juttijudata, V. 2005 Model-based control and estimation of cavity flow oscillations. In *Proceedings of the 44th IEEE Conference on Decision and Control*. Seville, Spain.

Rowley, C. W., Kevrekidis, I. G., Marsden, J. E. & Lust, K. 2003 Reduction and reconstruction for self-similar dynamical systems. *Nonlinearity* **16**, 1257–1275.

Rowley, C. W. & Marsden, J. E. 2000 Reconstruction equations and the Karhunen-Loève expansion for systems with symmetry. *Physica D. Nonlinear Phenomena* **142**, 1–19.

Saad, Y. & Schultz, M. H. 1986 GMRES: A generalized minimal residual algorithm for solving nonsymmetric linear systems. *SIAM J. Sci. Statist. Comput.* **7** (3), 856–869.

Sanchez, J., Marques, F. & Lopez, J. M. 2002 A continuation and bifurcation technique for navier-stokes flows. *Journal of Computational Physics* **180**, 78–98.

Scherpen, J. M. A. 1993 Balancing for nonlinear systems. *Systems and Control Letters* **21** (2), 143–153.

Siegel, S. G., Seidel, J., Fagley, C., Luchtenburg, D. M., Cohen, K. & McLaughlin, T. 2008 Low-dimensional modelling of a transient cylinder wake using double proper orthogonal decomposition. *Journal of Fluid Mechanics* **610**, 1–42.

Silva, W. A. & Bartels, R. E. 2004 Development of reduced-order models for aeroelastic analysis and flutter prediction using the cfl3dv6.0 code. *Journal of Fluids and Structures* **19**, 729–745.

Sinha, M., Kevrekidis, I. G. & Smits, A. J. 2006 Experimental study of a neimark-sacker bifurcation in axially forced taylor-couette flow. *Journal of Fluid Mechanics* **558**, 1–32.

Sirisup, S., Xiu, D., Karniadakis, G. E. & Kevrekidis, I. G. 2005 Equation-free/galerkin-free pod-assisted computation of incompressible flows. *Journal of Computational Physics* **207**, 568–587.

Sirovich, L. 1987 Turbulence and the dynamics of coherent structures, parts I–III. *Quarterly of Applied Mathematics* **XLV** (3), 561–590.

Skogestad, S. & Postlethwaite, I. 2005 *Multivariable Feedback Control Analysis and Design*, 2nd edn. John Wiley and Sons.

Smith, T. R. 2003 Low-dimensional models of plane Couette flow using the proper orthogonal decomposition. PhD thesis, Princeton University.

Tadmor, G., Centuori, M., Noack, B., Luchtenburg, M., Lehmann, O. & Morzynski, M. 2007 Low order galerkin models for the actuated flow around 2-d airfoils. AIAA Paper 2007-1313, 45th AIAA Aerospace Sciences Meeting and Exhibit.

Taira, K. & Colonius, T. 2007 The immersed boundary method: A projection approach. *Journal of Computational Physics* **225** (2), 2118–2137.

Taira, K. & Colonius, T. 2009*a* Effect of tip vortices in low-reynolds-number poststall flow control. *AIAA Journal* **47** (3), 749–756.

Taira, K. & Colonius, T. 2009*b* Three-dimensional flows around low-aspect-ratio flat-plate wings at low reynolds numbers. *Journal of Fluid Mechanics* **623**, 187–207.

Tang, J. & Bau, H. H. 1998 Numerical investigation of the stabilization of the no-motion state of a fluid layer heated from below and cooled from above. *Physics of Fluids* **10** (7), 1597–1610.

Temam, R. 1988 *Infinite-dimensional dynamical systems in mechanics and physics*, *Applied Mathematical Sciences*, vol. 68. New York, NY: Springer-Verlag.

Theodoropoulos, C., Qian, Y.-H. & Kevrekidis, I. G. 2000 "coarse" stability and bifurcation analysis using timesteppers: A reaction-diffusion example. *Proceedings of the National Academy of Sciences* **97**, 9840–43.

Trefethen, L. N. & Bau, D. I. 1997 *Numerical Linear Algebra*. Society for Industrial and Applied Mathematics.

Tuckerman, L. & Barkley, D. 1999 Bifurcation analysis for timesteppers. *IMA Volumes in Applied Mathematics and its Applications* **19** (119), 453–466.

Verghese, G. C., Levy, B. & Kailath, T. 1981 A generalized state-space for singular systems. *IEEE Transactions on Automatic Control* **26** (4), 811–831.

van de Wal, M. & de Jager, B. 2001 A review of methods for input/output selection. *Automatica* **37**, 487–510.

Wang, Y., Haller, G., Banaszuk, A. & Tadmor, G. 2003 Closed-loop lagrangian separation control in a bluff body shear flow model. *Physics of Fluids* **15** (8), 2251–66.

Wei, M. & Rowley, C. W. 2009 Low-dimensional models of a temporally evolving free shear layer. *Journal of Fluid Mechanics* **618**, 113–134.

Weisberg, A. Y., Kevrekidis, I. G. & Smits, A. J. 1997 Delaying transition n Taylor-Couette flow with axial motion of the inner cylinder. *Journal of Fluid Mechanics* **348**, 141–151.

Williams, D., Collins, J., Jankhot, C., Colonius, T. & Tadmor, G. 2008 Control of flow structure on a semi-circular planform wing. AIAA Paper 2008-0597, 46th AIAA Aerospace Sciences Meeting and Exhibit.

Zannetti, L. & Iollo, A. 2003 Passive control of the vortex wake past a flat plate at incidence. *Theoretical and Computational Fluid Dynamics* **16**, 211–230.

Zhou, K., Salomon, G. & Wu, E. 1999 Balanced realization and model reduction for unstable systems. *International Journal of Robust and Nonlinear Control* **9** (3), 183–198.